UNIVERSITÀ DEGLI STUDI DI CATANIA
DOTTORATO DI RICERCA IN FISICA
PhD IN PHYSICS - XXXI CYCLE

GRAZIA D'AGOSTINO

Orbit dynamics studies of injection, acceleration and extraction of high-intensity beams for the upgrade of the INFN-LNS Superconducting Cyclotron

PH.D THESIS

SUPERVISORS:
PROF. F. CAPPUZZELLO
DOTT. L .CALABRETTA
DOTT. W. KLEEVEN

ANNO ACCADEMICO 2017/2018

Contents

List of abbreviations

AISHa	Advanced Ions Source for Hadrontherapy
amu	atomic mass unit
AOC	Advanced Orbit Code
AVF	Azimuthal Varying Field
CAD	Computer Aided Design
CATANA	Centro di AdroTerapia ed Applicazioni Nucleari Avanzate
CEA	Commissariat à l'énergie atomique et aux énergies alternatives
CNAO	Centro Nazionale di Adroterapia Oncologica
CS	Ciclotrone Superconduttore at INFN-LNS in Catania
DCE	Double Charge Exchange reaction
EC	Electron Capture
ECRIS	Electron Cyclotron Resonance Ion Source
EDF	Energy Density Functional
ERC	European Research Council
ES	Energy Selection
EXCYT	EXotics with CYclotron and Tandem
FEM	Finite Element Method
FRAISE	New FRAgment Ion SEparator at INFN-LNS

FRIBs@LNS	in-Flight Radioactive Ion BeamS at LNS
FWHM	Full Width at Half Maximum
IBA	Ion Beam Applications company
IBM	Interacting Boson Model
INFN	Istituto Nazionale di Fisica Nucleare
INFN-LNS	Istituto Nazionale di Fisica Nucleare-Laboratori Nazionali del Sud
ISOL	Isotope Separation On Line
LASA	Laboratori Acceleratori e Superconduttività Applicata
MIT	Massachusetts Institute of Technology
MP	Median Plane
MSU	Michigan State University
NME	Nuclear Matrix Elements
NUMEN	NUclear Matrix Elements for Neutrinoless double beta decay
NURE	NUclear Reactions for neutrinoless double beta decay
pps	particle per second
QRPA	Quasi Random Phase Approximation
RF	Radio Frequency
RFS	RF Selection
RIBs	Radioactive Ion Beams
r.m.s.	root mean square
SI	Spiral inflector

TFH	Two Frequency Heating
ToF	Time of Flight
TWT	Traveller Wave Tube
2D	bi-dimensional
3D	three-dimensional
$0\nu\beta\beta$	Neutrinoless double beta decay
$2\nu\beta\beta$	Two-neutrino double beta decay
$\beta\beta$	Double beta decay

Introduction

The LNS (Laboratori Nazionali del Sud), operating since the early '80s, is one of the four national laboratories present in Italy of the INFN (Istituto Nazionale di Fisica Nucleare).

The nuclear research is carried out at the LNS laboratory mainly by means of ion beams delivered by two ion accelerators, a 15 MV Tandem and a k800 Superconducting Cyclotron, known as the CS (Ciclotrone Superconduttore). These accelerators enable to deliver to the INFN-LNS scientific community a large variety of stable ion beams with energies ranging from a few MeV/amu up to 80 MeV/amu.

In addition, RIBs (Radioactive Ion Beams) can be produced at INFN-LNS allowing to extend the nuclear research also to unstable beams induced reactions at intermediate energies. The facility for RIBs production, called FRIBs@LNS (in Flight Radioactive Ion BeamS), produces ion beams using the primary beam accelerated by the CS and exploiting the technique known as in-flight fragmentation. The investigations on the properties of unstable nuclei is usually limited to nuclei not far away from the stability valley, e.g. ^{10}Be, ^{16}C, ^{18}Ne, ^{68}Ni, with beam intensities of about 10^4-10^5 pps. Typical energies of the RIBs produced are between 20 MeV/amu and 45 MeV/amu.

In the past also an ISOL (Isotope Separation On Line) low energy radioactive beam facility, named EXCYT (EXotics with CYclotron and Tandem), was present at INFN-LNS. It was based on the combined use of the two accelerators and it was able to produce radioactive ion beams

with energy up to 7 MeV/amu.

The great variety of stable and radioactive ion beams delivered by means of the two accelerators, their wide energy range together with the development and use of high performance detection systems, allow a huge variety of experimental research at INFN-LNS in the fields of the reaction mechanisms, nuclear structure and nuclear astrophysics.

Although INFN-LNS was born as a nuclear physics research laboratory, also the research in the field of multidisciplinary science is developing over the years and it constitutes today a relevant fraction of the research activities performed in the laboratory. Multidisciplinary science is performed using the ion beams delivered by the Tandem and Superconducting Cyclotron. Among them, it is worth to cite the use of the 62 MeV proton beam delivered by the CS for the treatment of ocular diseases like uveal melanoma, performed by the first protontherapy facility developed in Italy, named CATANA (Centro di AdroTerapia e Applicazioni Nucleari Avanzate).

A continuous upgrading of the beam production and detection facilities is performed at LNS to continuously enrich its scientific program with innovative research lines.

The interest of the scientific community on neutrino physics has been growing through the years. The mass hierarchy and the nature of the neutrino are currently open questions. The $0\nu\beta\beta$ decay of atomic nuclei is a long-searched process which could gives us the answers to these questions. A critical aspect is that the Nuclear Matrix Element (NME) associated to the process must be reliably known.

NUMEN (NUclear Matrix Elements for Neutrinoless double beta decay), a nuclear physics project born recently at INFN-LNS, proposes the use of Heavy Ion induced Double Charge Exchange (HI-DCE) reactions as tools to access quantitative information, relevant for $0\nu\beta\beta$ decay NME. The pilot experiment carried out by the NUMEN team at LNS in Cata-

nia has already demonstrated that beam power of the order of $1-10$ kW (corresponding to current of $10^{13} - 10^{14}$ pps) of ^{12}C, ^{18}O and ^{20}Ne with energies in the range $15-70$ MeV/amu are mandatory for the NUMEN reaction study. An additional requirement is that the beam energy resolution $\Delta E/E$ should not overcome 1/1000 FWHM.

Currently, the maximum CS beam power does not exceed 100 W, so a substantial upgrade of the CS is needed to fulfil the NUMEN requirements. Also the other research projects at INFN-LNS could benefit from the upgrade of the CS. In particular, the installation of FRAISE (FRAgment In-flight SEparator) at INFN-LNS, together with the upgrade of the LNS cyclotron, would enable a substantial increase of the power of RIBs, also for ions very far from the stability valley.

The current CS performances are mainly limited by the low efficiency of the extraction process, which is carried out by electrostatic deflectors.

The lack of full separation between last turns in the INFN-LNS cyclotron implies a beam loss on the first electrostatic deflector. The maximum beam power that the CS can deliver is also limited by the thermal issues of the first electrostatic deflector. Indeed, although it is water cooled, the electrostatic deflector is not reliable when the dissipated beam power exceeds 100 W.

The stripping extraction is a valid solution to achieve a high extraction efficiency, also close to 100%, for the set of light-medium ion beams with mass number A $\leq$ 40 and energy higher than 15 MeV/amu required by the NUMEN and RIBs production projects.

The expected efficiency of the stripping extraction is higher than the present one, that is about 60%, obtained by means of the existing extraction system.

The extraction by stripping is not trivial to perform in the case of the LNS cyclotron since it requires significant changes in the cyclotron.

It is planned to use an extraction channel different from the existing one

in order to facilitate the exit of all the ion beams to be extracted by stripping. Since the new extraction channel needs to be larger than the present one in both the radial and axial directions, a new superconducting magnet (composed of the cryostat and two pairs of superconducting coils), fitting the new requirements must be built to replace the present one. The replacement of the cryostat and superconducting coils with new ones implies technological efforts to fit an already existing structure. Other aspects of the project of upgrade of the LNS cyclotron concerns the improvement of the performance of the ion sources, injection line and central region, all finalized to further enhance the present performance of the LNS cyclotron.

Technological efforts are necessary in order that the modifications to be applied to the cyclotron coexist with the existing components of the accelerator since the LNS cyclotron has to continue to accelerate and extract by electrostatic deflectors all the ion beams presently delivered to the LNS users. However, due to mechanical interference between the handling system of the stripper foils and one of the two electrostatic deflectors, it will possible to extract beams by stripping only in absence of the electrostatic deflector into the cyclotron and vice versa.

In the frame of the CS upgrade, this thesis is devoted to the simulation study of beam injection and acceleration up to the extraction, with the aim to overcome the current CS limitations and to propose innovative solutions for achieving the beam characteristics in terms of beam power and energy resolution required by the NUMEN and RIBs production projects.

One of the main subject studied in this thesis work was the stripping extraction from the CS. The study has been finalized to determine the position of the stripper foil for each ion to be extracted by stripping and the direction of the new extraction channel to be machined in the cyclotron. The simulation study has also finalized to determine the fea-

tures of the passive magnetic channels, which will be placed in the new extraction channel in order to compensate the horizontal defocussing effect of the magnetic fringing field on the extracted beams.

Another main question addressed in this thesis was the overall efficiency of beam transmission from the axial bore injection into the cyclotron up to the extraction. To perform such an evaluation, numerical beam tracking simulations from the axial bore entrance, through the present spiral inflector and central region, up to the extraction system have been done. Also a process of beam energy selection after the extraction has been considered. Particular attention has been paid to the improvement of the injection efficiency and the evaluation of the beam energy spread at the extraction. This second aspect is relevant in view of the stringent NUMEN requirement on the beam energy spread.

When a beam is extracted by stripping, the beam energy spread at the extraction depends not only on the energy gain per turn but also on the horizontal beam emittance. As it will shown in this thesis, this second factor plays an important role in the determining the beam energy spread at the extraction in the case of the CS, due to the large injected emittance into the cyclotron centre. Unfortunately, the lack of information on the injected beam features and on the exact orientation of the spiral inflector with respect to the central region electrodes have complicated the study, forcing us to make conservative assumptions about them. This implied that the results of this work could be, in some cases, overestimated, as for example in the case of the injection efficiency evaluation. However, this work permits to establish a roadmap to be followed for the improvement of the CS performances.

Hereinafter, a brief description of the contents of all the chapters which compose this thesis is given.

The first chapter introduces the physical and experimental reasons that have addressed the upgrade of the INFN-LNS Superconducting Cyclotron.

The NUMEN and the RIBs production projects will be described in some detail together with the beam requirement the CS is expected to satisfy to achieve the goals of both the projects. An overview of the present limitations of the CS performances will be also given.

The second chapter presents the main features and components constituting of the INFN-LNS Superconducting Cyclotron. Among them, great emphasis is given to the detailed description of the magnetic structure and of the injection and extraction systems, whose upgrade has a key role in this thesis work.

The aim of the third chapter is to present the CS upgrade project.

The physics beyond stripping extraction and the criticality to be overcome in order to perform the stripping extraction from the CS will be detailed.

The forth chapter presents the study of the stripping extraction from the CS. The procedure used and the results of the simulation study are presented.

The fifth chapter deals with the development of the model of the accelerating and magnetic structures of the CS, needed for computations of particle orbits in the cyclotron. The modelling approach used and the main features of the two models are presented.

Finally, the sixth chapter presents the study of the beam injection, acceleration and extraction in the LNS cyclotron. Central to the entire chapter are the questions relative to the injection efficiency and beam energy spread at the extraction, which will be carefully discussed together with ideas for further improvements of the CS performances.

Chapter 1

High intensity beams at INFN-LNS in Catania

Since Lawrence built the first cyclotron in 1929 [1], there has been an increasing progress in the performances of cyclotrons both for research and for medical, industrial, technological applications.

The increase of the ion beam intensity represents the new challenge to drive experiments searching for rare processes, especially in nuclear and high energy physics, for which higher sensitivity is required.

At INFN-LNS in Catania the upgrade of the existing Superconducting Cyclotron (CS) is now under study to significantly increase the intensity of light-medium ion beams with energies inside the range 15-70 MeV/amu.

High intensity ion beams are requested by an innovative research project, named NUMEN (NUclear Matrix Elements for Neutrinoless double beta decay) [2], for nuclear physics studies correlated to neutrino physics.

Furthermore, the improvement of the CS performance, together with the installation of FRAISE, the new FRAgment In-flight SEparator at INFN-LNS [3], would open up new perspectives of research in nuclear physics and astrophysics for the other existing research projects that currently use ion beams accelerated by the CS.

This chapter introduces the physical and experimental reasons behind

the upgrade of the INFN-LNS Superconducting Cyclotron. An overview of the present limitations of the CS performances, that prevent to fulfil the ion beam NUMEN requirements, will be also given.

1.1 The neutrinoless double beta decay

1.1.1 Introduction

The neutrino is a neutral particle, unaffected by electromagnetic and strong interactions.

It is the most elusive particle so far discovered because it interacts weakly with the matter, being able to cross enormous distances practically undisturbed. As a consequence, despite its existence has been known since the 1950s, today many properties of the neutrino are still beyond comprehension. Fundamental open questions are the value of the neutrino mass and its nature of Dirac or Majorana particle.

The results obtained by neutrino oscillation experiments demonstrate that the neutrino has some mass and the three neutrino mass eigenstates (m_1, m_2 and m_3) mix each other [4–8]. The obtained data are compatible with two possible mass hierarchies: the normal one, characterized by $m_1 < m_2 << m_3$, and the inverted one $m_3 << m_1 < m_2$.

Unfortunately, the experiments studying neutrino oscillations do not allow to obtain information on the absolute scale of the neutrino masses, because they are sensitive only to the squared differences of the neutrino mass eigenvalues. In addition, they are not even sensitive to the neutrino nature [9]. In this scenario, the neutrino could be a Dirac or Majorana particle. In the first case, it would be distinct from its antiparticle, in the latter one, neutrino and antineutrino would be indistinguishable.

The neutrinoless double beta decay ($0\nu\beta\beta$) is a key tool for finding answers to the open questions on the neutrino. If observed, this process would prove that the neutrino is a Majorana particle and it could give

information regarding the neutrino masses and their hierarchy, provided that reliable Nuclear Matrix Elements (NMEs), present in the expression of the $0\nu\beta\beta$ rate, can be obtained.

Hereinafter, an overview on the double beta decay is presented.

In particular, this section is focused on the process without emission of neutrinos and on the importance for obtaining experimentally quantitative information about the relevant NMEs for the $0\nu\beta\beta$ process.

1.1.2 The double beta decay

The double beta decay ($\beta\beta$) is a rare nuclear process in which a nucleus of mass number A and atomic number Z, (A, Z), is converted into its isobar $(A, Z \pm 2)$. The literature distinguishes two types of mechanism for this process, named two-neutrino double beta decay ($2\nu\beta\beta$) and neutrinoless double beta decay ($0\nu\beta\beta$) respectively (Fig. 1.1).

The two-neutrino double beta decay mode is allowed by the Standard Model of elementary particles and it does not impose special requirements on the neutrino properties. The process, observed for more than ten nuclei [10, 11], occurs irrespective of whether the neutrino is a Majo-
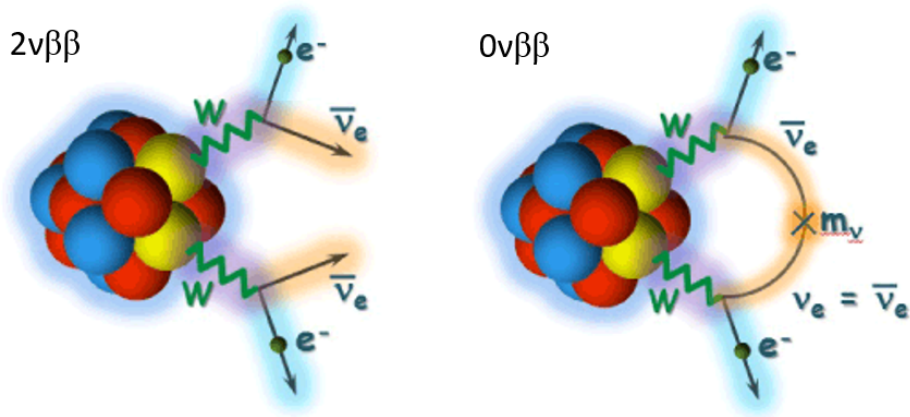

Figure 1.1: $2\nu\beta\beta$ and $0\nu\beta\beta$ on the left and on the right respectively. Taken from wwwkm.phys.sci.osaka-u.ac.jp.

rana or a Dirac particle and irrespective of whether it has a mass or not. The possible $2\nu\beta\beta$ decay modes are:

$$(A, Z) \longrightarrow (A, Z + 2) + 2e^- + 2\bar{\nu}_e \qquad (\beta\beta^-) \qquad (1.1.1)$$

$$(A, Z) \longrightarrow (A, Z - 2) + 2e^+ + 2\nu_e \qquad (\beta\beta^+) \qquad (1.1.2)$$

$$(A, Z) + 2e^- \longrightarrow (A, Z - 2) + 2\nu_e \qquad (ECEC) \qquad (1.1.3)$$

$$(A, Z) + e^- \longrightarrow (A, Z - 2) + e^+ + 2\nu_e \qquad (EC\beta^+) \qquad (1.1.4)$$

The $2\nu\beta\beta$ is a second-order weak process, resulting in an extremely slow decay rate, namely the slowest process ever observed in nature, with half-lives of the order of $10^{18} - 10^{22}$ years [12].

Therefore, the isotopes candidate for experimental observation of $2\nu\beta\beta$ are even-even nuclei for which the single beta decay is energetically forbidden or suppressed by large change in angular momentum.

In the $0\nu\beta\beta$ process, that has never been observed, only electrons would be emitted:

$$(A, Z) \longrightarrow (A, Z + 2) + 2e^- \qquad (\beta\beta^-) \qquad (1.1.5)$$

$$(A, Z) \longrightarrow (A, Z - 2) + 2e^+ \qquad (\beta\beta^+) \qquad (1.1.6)$$

$$(A, Z) + 2e^- \longrightarrow (A, Z - 2) \qquad (ECEC) \qquad (1.1.7)$$

$$(A, Z) + e^- \longrightarrow (A, Z - 2) + e^+ \qquad (EC\beta^+) \qquad (1.1.8)$$

The $0\nu\beta\beta$ process is forbidden in the Standard Model, since the lepton number conservation is violated by two units, and its observation would thus points towards the existence of physics beyond the Standard Model. This process can occur only if neutrino and antineutrino must be indistinguishable and, as a consequence, the neutrino must be a Majorana particle. In this scenario, the antineutrino emitted at one vertex can be absorbed as a neutrino at the other vertex, as shown in the process scheme in Fig. 1.1 on the right. In addition to the Majorana equivalence of neutrino and antineutrino, a non-zero neutrino mass is required to flip

the helicity since the antineutrino is right-handed and the neutrino is left-handed.

The rate of $0\nu\beta\beta$ process $\Gamma_{0\nu}$ can be factorized as the phase-space factor $G_{0\nu}$, the nuclear matrix element $M_{0\nu}$ and the effective Majorana mass $< m_{\beta\beta} >$ [13]:

$$\Gamma_{0\nu} = [T_{1/2}]^{-1} = G_{0\nu} \cdot |M_{0\nu}|^2 \cdot | < m_{\beta\beta} > |^2 \qquad (1.1.9)$$

The information concerning the neutrino mass is contained in $< m_{\beta\beta} >$:

$$< m_{\beta\beta} >= \sum_{i=1}^{3} U_{ei}^2 \cdot m_i \qquad (1.1.10)$$

where U_{ei} represents the Pontecorvo-Maki-Nakagawa-Sakata mixing matrix [14, 15], that describes the mixing between the neutrino mass eigenstates and the neutrino flavor eigenstates, and m_i are the different neutrino mass eigenvalues.

In order to obtain information on $< m_{\beta\beta} >$ from the $0\nu\beta\beta$ rate measurement, the knowledge of $G_{0\nu}$ and $M_{0\nu}$ is essential.

$G_{0\nu}$ is proportional to the 5$^{\text{th}}$ order of the decay Q-value and can be accurately calculated as explained in reference [16]. As a consequence, any uncertainty on the nuclear matrix element $M_{0\nu}$ reflects directly on the evaluation of $< m_{\beta\beta} >$.

$|M_{0\nu}|^2$ is the transition amplitude from the initial ϕ_i to the final ϕ_f nuclear states of the $\beta\beta$ process through the $0\nu\beta\beta$ decay operator $\hat{O}^{0\nu\beta\beta}$:

$$|M_{0\nu}|^2 = | < \phi_f|\hat{O}^{0\nu\beta\beta}|\phi_i > |^2 \qquad (1.1.11)$$

Since the $\beta\beta$ decay process involves transitions in atomic nuclei, nuclear structure issues must be also accounted for, in order to describe the NME. The evaluation of the NMEs is presently limited to state-of-the-art model calculations based on different methods, e.g. Quasi-particle Random Phase Approximation (QRPA), large scale shell-model, Interacting Boson Model (IBM), ab-initio, Energy Density Functional (EDF) [17–22].

14

Despite the calculations are constrained by high-precision experimental information from single charge exchange reactions, transfer reactions and electron capture, discrepancy factors higher than two are currently reported in literature [23]. The evaluation of the nuclear matrix element is a challenge in nuclear theory due to the complicated nuclear many-body nature of the problem.

1.2   The NUMEN project

NUMEN at INFN-LNS proposes cross section measurements of heavy ion induced Double Charge Exchange (DCE) reactions toward the determination of the nuclear matrix elements, present in the expression of the $0\nu\beta\beta$ rate.

Hereinafter, an overview of the research project is presented. Detailed information about the project can be found in Ref. [2].

The DCE reactions are characterized by the transfer of two charge units, leaving the mass number unchanged, and they can proceed by a sequential nucleon transfer mechanism or by meson exchange.

Despite the $0\nu\beta\beta$ decay and heavy ion DCE reactions are mediated by different interactions, they present a number of similarities, such as the initial and final nuclear states and the mathematical structure of the transition operators. The description of NMEs for DCE and $0\nu\beta\beta$ presents the same level of complexity but the DCE reaction study provides the great advantage to allow one to obtain experimental information on NMEs in laboratory controlled conditions.

The main characteristic of heavy ion induced nuclear reactions is the large number of final channels related to a large value of energy and angular momentum introduced by the heavy projectile into the initial reaction channel. In this scenario, the measurement of DCE high-resolution energy spectra and accurate absolute cross sections at very forward angles (included 0°) is crucial to identify the transitions of interest [17, 24].

The simultaneous measurement of the other reaction channels is fundamental in order to isolate the direct DCE mechanism from the competing multi-nucleon transfer processes.

Modern high resolution and large acceptance spectrometers play a key role to extract information on NMEs from DCE reactions since they allow one to effectively face the main experimental challenges, that the early studies of heavy ion induced double charge exchange reactions failed to overcome. In literature a lack of data persists because of the technical difficulties to measure very low cross sections at zero degrees and the consequent poor yields in the measured energy spectra and angular distributions [25–27].

In order to achieve its goal, NUMEN will perform its experiments using the facility already installed at INFN-LNS, composed by the Superconducting Cyclotron and the MAGNEX spectrometer [28], a modern high resolution and large acceptance magnetic system characterized by high resolution in energy, mass and angle, shown in Fig. 1.2.

NUMEN aims to carry out a series of experimental campaign in order to extract data-driven information on the nuclear matrix elements for the possible candidates to the $0\nu\beta\beta$, indicated by the neutrino scientific community, i.e. ^{48}Ca, ^{76}Ge, ^{76}Se, ^{82}Se, ^{96}Zr, ^{100}Mo, ^{106}Cd, ^{110}Pd, ^{116}Cd, ^{110}Sn, ^{124}Sn, ^{128}Te, ^{130}Te, ^{130}Xe, ^{136}Xe, ^{148}Nd, ^{150}Nd, ^{154}Sm, ^{160}Gd, ^{198}Pt.
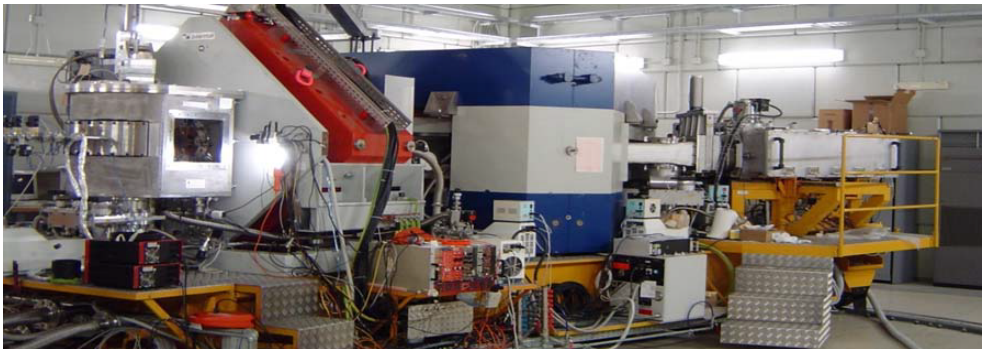

Figure 1.2: A view of MAGNEX spectrometer at Laboratori Nazionali del Sud in Catania.

The first campaigns of experiments are foreseen in sinergy with the NURE (NUclear REactions for neutrinoless double beta decay) project [29], a shorter time scale project correlated to NUMEN. It has been selected for receiving funding for 5 years in the call Starting Grant 2016 of European Research Council (ERC).

A pilot experiment was performed at INFN-LNS with the aim of verifying the feasibility of the technique proposed by NUMEN to access the NMEs [17]. In such an experiment, the $^{40}Ca(^{18}O,^{18}Ne)^{40}Ar$ DCE reaction was studied using a ^{18}O beam accelerated by the LNS Superconducting Cyclotron to the final kinetic energy of 270 MeV and detecting the ejectiles by means of MAGNEX.

The experiment demonstrated that high resolution and statistically significant experimental data can be measured for DCE processes but, for a systematic study of the many candidates for $0\nu\beta\beta$ decay, important experimental limitations need to be overcome. This implies substantial changes in the technologies of the MAGNEX spectrometer and the upgrade of the existing INFN-LNS accelerator facility.

The $(^{18}O,^{18}Ne)$ reaction will be used as a probe for the $\beta\beta^+$ transitions and the $(^{20}Ne,^{20}O)$ or the $(^{12}C,^{12}Be)$ reaction for the $\beta\beta^-$, with the aim of exploring the DCE mechanism in both directions.

The CS will provide the required beams, namely ^{18}O, ^{20}Ne and ^{12}C , at energies ranging from 15 MeV/amu to 70 MeV/amu.

The choice of the target isotopes to be used in the NUMEN experiments represents a compromise between the interest of the scientific community to specific isotopes and related technical issues. The main constraints are the possibility of separation of the ground state-to-ground state transition from that to the first excited state of the residual nucleus in the measured excitation energy spectra and the availability of thin uniform target of isotopically enriched material.

The energy resolution in the measured excitation energy spectra at for-

ward angles mainly depends on three independent factors, namely the intrinsic energy resolution of the MAGNEX spectrometer $\delta E / E_{MAGNEX}$ ($\simeq$ 1/1000 FWHM), the energy spread of the CS accelerated beam $\delta E / E_{CS}$ and a contribution due to the straggling and energy loss of the beam and ejectiles in the target $\delta E / E_{TARGET}$. The total energy resolution is thus:

$$\delta E \sim \sqrt{(\delta E_{MAGNEX})^2 + (\delta E_{CS})^2 + (\delta E_{TARGET})^2} \qquad (1.2.1)$$

The request of high resolution of the measured energy spectra implies challenging requests on the target characteristics and on the energy spread of the extracted beams from the INFN-LNS Superconducting Cyclotron. NUMEN requires an energy resolution of the CS beams equal to 1/1000 FWHM. The $\delta E / E_{TARGET}$ depends, for a given beam, on the target material and thickness and on its uniformity.

Beside the high energy resolution challenge, the exploration of nuclei of interests for $0\nu\beta\beta$ is also challenging for the following reasons, that imply low process yields:

- Low cross section of the DCE reactions;

- The $(^{18}O,^{18}Ne)$ reaction, investigated in the pilot experiment, is particularly advantageous but this reaction is $\beta\beta^+$ kind, instead most of the research on $0\nu\beta\beta$ decay is of the $\beta\beta^-$ kind.
  None of the reactions of $\beta\beta^-$ kind looks like as favourable as the $(^{18}O,^{18}Ne)$. For example, the $(^{18}Ne,^{18}O)$ requires a radioactive beam, which cannot be available with enough intensity;

- In some cases, e.g. ^{136}Xe or ^{130}Xe, gas or implanted target will be necessary. They are normally much thinner than solid targets obtained by evaporation and this implies consequent reduction of the collected yield;

- The detection in coincidence of gamma rays from the de-excitation of the populated states will be necessary for the cases for which the energy resolution is not enough to separate the ground from the excited states in the final nucleus in the measured excitation energy spectra. As consequence, a yield reduction is expected for these cases.

Due to the low process yields, high intensity beams are necessary for the DCE reaction study in order to collect significant statistics of data in a reasonable time. The challenge proposed by NUMEN and by the NURE projects is to measure rare nuclear transitions under a very high rate of heavy ions produced by the beam-target interaction.

The pilot experiment demonstrated that higher beam intensity with respect to the present one is mandatory for the NUMEN reaction study. This goal can be achieved by a substantial upgrade of the CS in order to overcome the present limit on the maximum beam power delivered by the CS ($\simeq 100$ W). By changing the beam extraction mode, we plan to extract a beam power from the CS in the range $1 - 10$ kW, corresponding to currents of the order of $10^{13} - 10^{14}$ pps for the NUMEN energy range. The increase of the beam intensity implies first of all the development of cooled isotopically enriched thin target, able to resist to the high power dissipated by the interaction of the intense beams with the target material. Furthermore, also the upgrade of the MAGNEX spectrometer is foreseen especially to take into account the higher rate of incoming ejectiles on its detection system. In addition, as above-mentioned, the use of a gamma detector system close to the target is expected for the discrimination of nearby energy states.

Due to the expected high beam power extracted by the CS, the radioprotection issues must be considered. A careful evaluation of radiation levels along the new dedicated beam tranport line, is mandatory, together with the study of its effects on detectors, electronics and various equipment in

the MAGNEX experimental hall.

1.3 New research in nuclear physics and astrophysics using intense radioactive ion beams

The use of Radioactive Ion Beams (RIBs) in the nuclear physics experiments has been allowing since last decades to investigate many properties of unstable nuclei. The RIBs can be produced by the Isotope Separation On Line (ISOL) [30] and the in-flight [31] production techniques.

Many facilities for RIBs production are present worldwide, one of which is installed at INFN-LNS in Catania, and many others are still under construction [32–34].

The FRIBs@LNS (in Flight Radioactive Ion BeamS at LNS) facility [35] has been operating in Catania for the last 15 years allowing one to carry out nuclear physics experiments for the investigation of the properties of short-lived nuclear species. The RIBs are produced, using the in-flight technique, by fragmentation of a fast projectile on a thick Beryllium made target. The CS has a key role within the FRIBs facility because it delivers the accelerated primary beams, in particular ^{12}C, ^{20}Ne, ^{40}Ar and ^{58}Ni ions at energies between 40 MeV/amu and 60 MeV/amu. The reaction processes occur close to the CS exit where the thin target is placed.

Since a multitude of nuclei, mainly stable, are produced after the incidence of the primary beam on the thin target, a magnetic analysis is needed to select the RIBs of interest according to the specific nuclear physics study to be carried out. In the FRIBs@LNS facility, the produced exotics fragments are selected, transported and focused by the same optical elements of the beam line normally used for the transport of the beams to the LNS experimental halls.

As shown in Fig. 1.3 below, the fragment separator consists on two 45° bending dipole magnets D1 and D2, three quadrupoles triplets Q1-Q3, Q4-Q6 and Q7-Q9 and two sextupoles correctors S4, S9 near the quadrupoles Q4, Q9.

The bending dipole magnets are used for isotope selection according to the magnetic rigidity, the quadrupoles allow one the beam focusing.

A degrader can be placed at the intermediate focus.

The produced RIBs are delivered to many experimental halls, housing detectors as CHIMERA [36], FARCOS [37], MAGNEX [38].

Figure 1.3 above shows the 3D layout of the LNS with the beam lines and the experimental halls.

Since the magnetic analysis does not allow one to separate isotopes with the same mass-to-charge ratio and, in addition, it has always a finite dp/p acceptance ($\simeq 1\%$ in the case of FRIBs), an event-by-event identification (tagging) of each nucleus of the secondary beam, before it interacts with the secondary target, is performed in the beam line.

The tagging technique combines Time of Flight (ToF) and energy loss ΔE measurements, with detectors placed in the beam line and close to the scattering chambers in the experimental halls. The use of the ΔE-ToF method has the advantage of not stopping the incoming ions and to modify as less as possible their characteristics.

The investigations on the properties of unstable nuclei have been always limited to nuclei not far away from the stability valley, e.g. ^{10}Be, ^{16}C, ^{18}Ne, ^{68}Ni, with beam intensities of about $10^4 - 10^5$ pps. Typical energies of the RIBs produced are between 20 MeV/amu and 45 MeV/amu.

The limit on the maximum beam power delivered by the CS and the radio-protection issues related to the fragment separator shielding do not allow to obtain higher intensities for these nuclei and, in addition, to perform investigations on nuclei far away from the stability valley, being the yields for very exotic nuclei are very low. Nevertheless, impor-
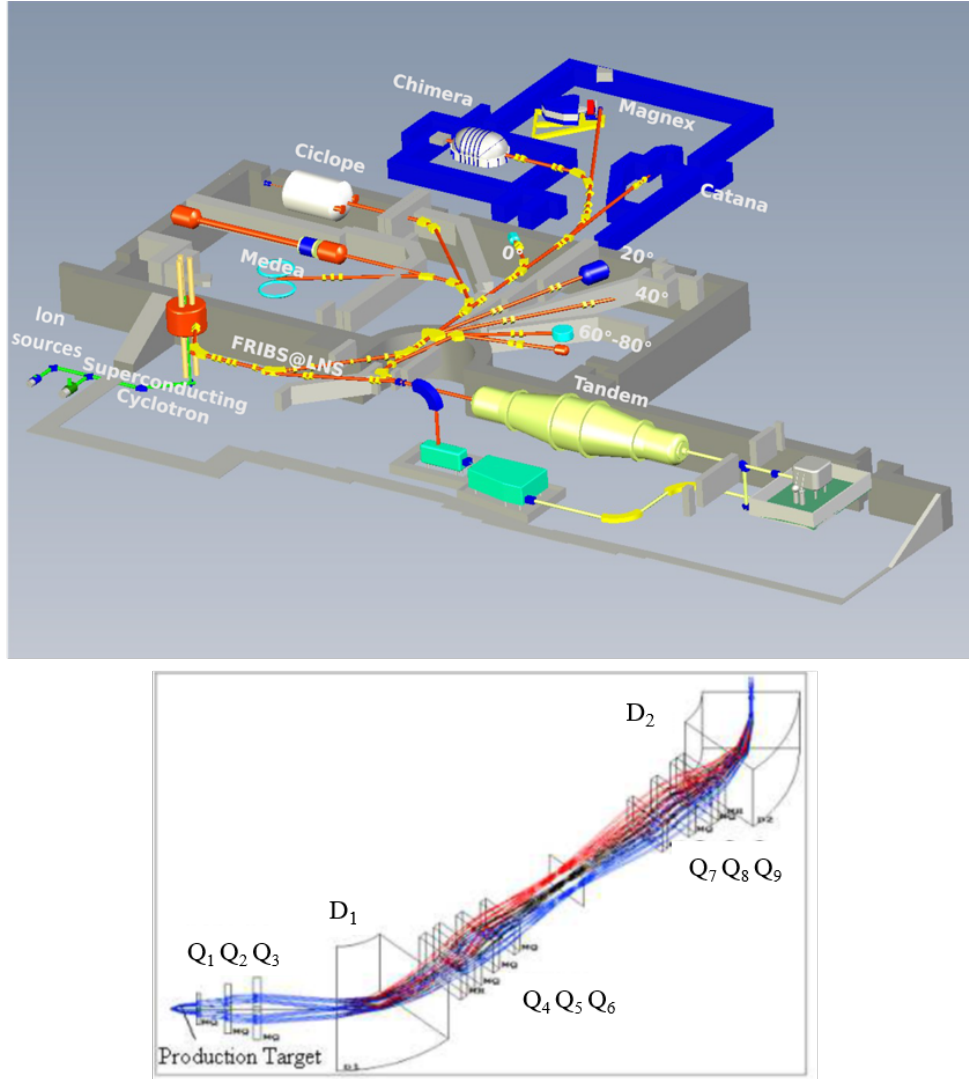
Figure 1.3: Above: 3D layout of the LNS laboratories with the beam lines and the experimental halls. Below: layout of the Fragment Separator used in the FRIBs project.

tant physics cases have been investigated by using the RIBs delivered by FRIBs@LNS [3].

In the perspective of the upgrade of INFN-LNS Superconducting Cyclotron, a new FRAgment Ion SEparator (FRAISE) [3] is now under study at INFN-LNS. More detail about the status of the FRAISE study are presented in Chapter 3. The expected higher beam power for primary

beams delivered by the CS would be used to produce very intense RIBs also for ions very far from the stability valley. Consequently, progress in production method of the RIBs coupled with advances in experimental techniques and detection device could open new interesting perspectives of research at INFN-LNS in the field of the exotic nuclei, interesting cluster physics, nuclear structure and isospin physics studies. With FRAISE, it is also foreseen to extend the use of RIBs towards the low energy domain (few MeV/amu) for nuclear astrophysics studies [3].

1.4 The improvement of the INFN-LNS Superconducting Cyclotron performances

The INFN-LNS Superconducting Cyclotron has been operating in axial injection mode for about 18 years delivering beams of various ion species and energies with currents up to few hundred of enA.

As described in Chapter 2, the present beam extraction system is composed of two electrostatic deflectors followed by a set of magnetic channels. Unfortunately, the accelerator compactness limits the extraction efficiency at about 60% and consequently the maximum beam power that can be delivered by the CS.

Turn separation is a critical aspect when the beam extraction occurs by means of electrostatic deflectors and especially in compact cyclotrons, as in the case of the CS. The lack of separation between last turns in the INFN-LNS cyclotron implies a beam loss on the first electrostatic deflector. The maximum beam power that the CS can deliver is also limited by the thermal issues of the first electrostatic deflector. Indeed, although it is water cooled, the electrostatic deflector is not reliable when the dissipated beam power exceeds 100 W. As a consequence, the extraction of beam power up to 10 kW is not feasible using the present extraction system.

The stripping extraction seems to be a valid alternative to increase the extraction efficiency for the ion species with mass number A < 20 and energies higher than 15 MeV/amu. For these ions and energies, the stripping extraction would allow one to achieve extraction efficiencies higher than 99% [39]. However, the new extraction method would be very efficient also for medium mass nuclei with mass number A $\sim$ 40, that are of interest for RIBs production.

The extraction by stripping of the light-medium ion beams for NUMEN and RIBs production, together with the increase of the injection efficiency, would allow one to extract 100 times higher beam power than the present one.

Table 1.1 shows the expected beam currents and beam power at the exit of the upgraded INFN-LNS Superconducting Cyclotron for some of the ion beams of interest for NUMEN. Conservative values of the beam currents delivered by the ion source and injected and accelerated by the cyclotron are also given.

In order to extract by stripping ion beams, a significant upgrade of the CS is foreseen. Accurate simulation studies, followed by changes of the technologies currently used and the development of new ones, are mandatory in order to transform the CS in a high intensity cyclotron.

Hereinafter, a brief description of the project of the CS upgrade is given. A detailed description of it is presented in Chapter 3.

The main changes in the INFN-LNS Superconducting Cyclotron will consist in the replacement of the existing cryostat and the superconducting coils with new ones. The coils will have the same form factors of the present ones but smaller height to significantly increase the vertical gap available for the new extraction channel, that it is foreseen to be machined and used for the stripping extraction.

At the same time, the CS has to continue to deliver all the beams presently accelerated in order to satisfy the requests of the already exist-

ing research projects at INFN-LNS.

For this reason, the CS will be equipped with two extraction systems and two extraction channels, in particular, the present one to be used for the extraction by electrostatic deflectors and the new one for the stripping extraction.

The expected energy spread of the beams after the stripping extraction is around ±0.3% FWHM, value exceeding the stringent request of the NUMEN research project. A new transport line to be used as an energy selector to reduce the beam energy spread as well as a fragment in-flight separator for the production of radioactive ion beams is under study at INFN-LNS.

Ion	Energy MeV/amu	I_{source} eμA	I_{inj} eμA	I_{extr} eμA	I_{extr} pps	P_{extr} Watt
$^{12}C^{4+}$	45	400	60(4+)	90(6+)	$9.4 \cdot 10^{13}$	8100
$^{12}C^{4+}$	60	400	60(4+)	90(6+)	$9.4 \cdot 10^{13}$	10800
$^{18}O^{6+}$	29	400	60(6+)	80(8+)	$6.2 \cdot 10^{13}$	5220
$^{18}O^{6+}$	45	400	60(6+)	80(8+)	$6.2 \cdot 10^{13}$	8100
$^{18}O^{6+}$	70	200	30(7+)	34.3(8+)	$2.7 \cdot 10^{13}$	5400
$^{20}Ne^{7+}$	28	400	60(7+)	85.7(10+)	$5.3 \cdot 10^{13}$	4800
$^{20}Ne^{7+}$	70	400	60(7+)	85.7(10+)	$5.3 \cdot 10^{13}$	12000

Table 1.1: Expected beam currents and power delivered at the exit of the upgraded Catania cyclotron for some of the ion beams of interest for the NUMEN research project.

Chapter 2

The INFN-LNS Superconducting Cyclotron

The construction of the LNS Superconducting Cyclotron (CS) was funded by INFN (Istituto Nazionale di Fisica Nucleare) in 1981.

The CS was born from the collaboration between two INFN laboratories, LASA in Milan and LNS in Catania. In particular, the design of the accelerator and the construction of its main components were performed at LASA [40] while the cyclotron was assembled in its final location in Catania in 1990 [41, 42]. The CS was at that time the first cyclotron to have travelled more than 1000 km from the place of conception to its final site.

During the first four years of operation, the cyclotron worked as a booster of the 15 MV Tandem accelerator, previously installed at INFN-LNS [43]. The Tandem beams were radially injected into the cyclotron, where a stripper foil, located on a hill, increased the charge state of the ions before the acceleration in the CS.

The first beam extracted from the CS, ^{58}Ni^{16+} with a final kinetic energy equal to 30 MeV/amu, was available in the experimental rooms of the LNS laboratory in June 1995 and the first nuclear physics experiment was successfully performed the following month [44].

In the year 2000 the radial injection mode was replaced by the axial in-

jection mode and, since then, the CS has been working in stand alone mode.

The main reason behind the introduction of the axial injection was the possibility to increase the intensity of light ion beams using an external ECRIS (Electron Cyclotron Resonance Ion Source) in order to give the CS the role of primary accelerator for the production of radioactive ion beams in the frame of the EXCYT (EXotics with CYclotron and Tandem) project at INFN-LNS [45].

This chapter is devoted to present the main features of the INFN-LNS Superconducting Cyclotron.

2.1   Main characteristics

The INFN-LNS cyclotron is a compact superconducting cyclotron characterized by the three-fold rotational symmetry.

It is a multi-particle variable energy cyclotron, able to accelerate ions from the lightest ones up to Uranium, mainly used for nuclear physics research.

Although the CS is not able to accelerate proton beams, since 2002 protons has been used for radiotherapy. Indeed, H_2^+ molecules are accelerated and extracted and then broken into two protons when crossing a stripper foil placed in the beam line out of the cyclotron.

The isochronous magnetic field, in the range of 2.2-4.8 T, is produced by the combined contribution of two superconducting main coils, three fully saturated iron spiralled pole sectors, the yoke and twenty trim coils wound around each hill.

The CS was the first cyclotron in Europe to use superconducting coils to generate the main field. The trim coils are used for the fine-tuning of the isochronous magnetic field for the acceleration of many ions with different final kinetic energies.

The bending limit K_B (depending on the product of the maximum mag-

netic field at the extraction and the extraction radius) is 800 and the focusing limit K_F (depending on the flutter and on the spiral angle) is 200. For any ion charge-to-mass ratio Q/A, K_B and K_F set a limit on the maximum kinetic energy per nucleon T/A. In particular, for a given Q/A, the maximum T/A is the smallest between the following values:

$$T/A = K_B \cdot (Q/A)^2 \tag{2.1.1}$$

$$T/A = K_F \cdot (Q/A) \tag{2.1.2}$$

The operating diagram of the CS in the $(B_0, Q/A)$ plane, where B_0 is the centre magnetic field, is shown in Fig. 2.1. The bending K_B and focusing K_F limits are shown, together with lines of constant kinetic energy per nucleon. The minimum operating field B_0 is 22 kG, limit imposed by the resonance $\nu_r + 2 \cdot \nu_z = 3$, where ν_r and ν_z are respectively the radial and
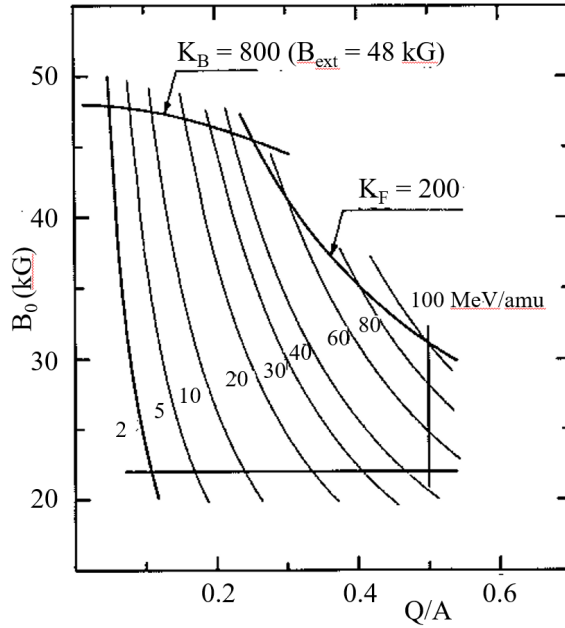

Figure 2.1: Operating diagram of the CS in the $(B_0, Q/A)$ plane, where B_0 is the centre magnetic field. Bending K_B, focusing K_F and low field limits are indicated. Constant kinetic energy per nucleon lines are also shown.
The present limit on the maximum energy is 80 MeV/amu and not 100 MeV/amu.

28

vertical betatron oscillation frequencies [46].

At low Q/A and T/A, the operating diagram is bounded by the bending limit K_B, while the focusing limit becomes more restricting at high Q/A and T/A.

The CS was designed for energies between 100 MeV/amu for fully stripped light ions and down to 20 MeV/amu for heavy ions like Uranium.

Any beams with an appropriate charge-to-mass ratio Q/A and desired kinetic energy T/A, that lie within the diagram, could in principle be accelerated. Actually, the limit on the maximum energy is lower than 100 MeV/amu due to components of the CS, like the electrostatic deflectors, that prevent the cyclotron from achieving the best performance. The actual maximum energy allowed is 80 MeV/amu for fully stripped light ions.

Harmonic numbers h equal to 1, 2, 3 and 4 are available for acceleration in a wide range of energy. The synchronism condition is given by:

$$f_{RF} = h \cdot f_0 \qquad (2.1.3)$$

with

$$f_0 = \frac{\omega_0}{2\pi} \quad \text{with} \quad \omega_0 = \frac{qB_0}{m} \qquad (2.1.4)$$

where f_{RF} is the frequency of the RF accelerating voltage and f_0 is the ion orbital frequency. In Eq. (2.1.4) q is the ion charge, m is the particle mass and B_0 is the isochronous value of the magnetic field in the cyclotron centre.

Figure 2.2 shows the ion energy per nucleon as a function of the RF frequency, for the 1st, 2nd, 3rd and 4th harmonic modes of acceleration. The operating frequency range of the RF cavities is 15-48 MHz.

The CS has almost always worked in harmonic $h = 2$ in order to obtain beam energies in a wide range, between 8 MeV/amu ($\simeq$ Coulomb barrier) and 100 MeV/amu. Only the energies in the range 2-8 MeV/amu, lower than the Coulomb barrier, are excluded, as shown in Fig. 2.2 .
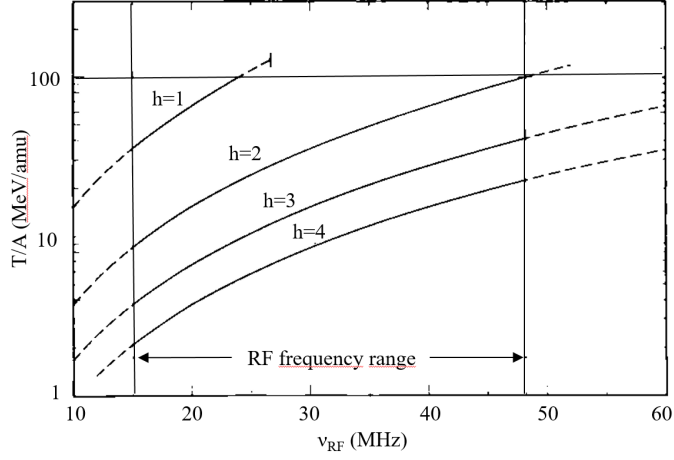
Figure 2.2: Energy per nucleon as function of the RF frequency for the harmonics equal to 1, 2, 3 and 4. The operating frequency range of the RF cavities of the CS is 15-48 MHz.

The accelerating system consists of three $\lambda/2$ coaxial resonators loaded with 60° dees placed in the valleys. Because of the presence of the cryostat and the small distance between the superconducting coils, the inductive parts of the RF cavities extend vertically. The central region, designed before 2000, was optimized to work in 2nd harmonic mode of acceleration. The beams are generated by two ECR ion sources and axially injected into the median plane through a spiral inflector.

The present extraction system consists of two electrostatic deflectors, placed on consecutive hills, and a set of passive magnetic focusing channels.

The main cyclotron parameters are listed in Table 2.1.

Figure 2.3 shows on the left the sketch of the cyclotron with its main components. On the right of Fig. 2.3 a picture of the INFN-LNS Superconducting Cyclotron is presented.
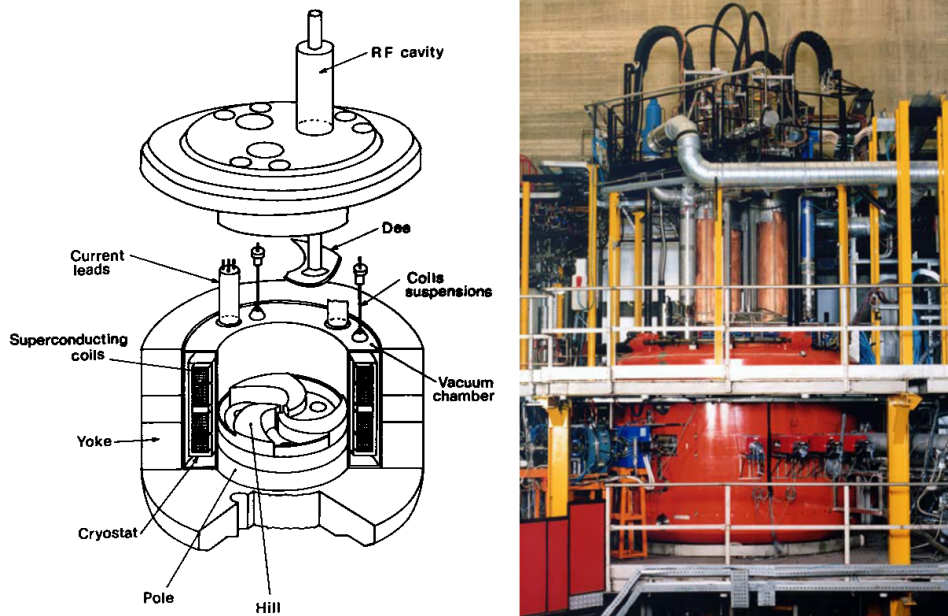
Figure 2.3: The INFN-LNS Superconducting Cyclotron. On the left, the sketch of the cyclotron with its main components. On the right, a picture of the cyclotron.

Bending limit K_B	800
Focusing limit K_F	200
Center field [min-max]	22-48 kGauss
Pole radius	900 mm
N$^{\underline{o}}$ of sectors	3
Superconducting coils	2 pairs
N$^{\underline{o}}$ of trim coils	20 (for sector)
N$^{\underline{o}}$ of dees	3 (in valleys)
RF frequency range	15-48 MHz
Harmonics h	1, 2, 3, 4 (only 2 used)

Table 2.1: Main parameters of the INFN-LNS Superconducting Cyclotron.

2.2 The magnetic structure

As in all compact superconducting cyclotrons, the main magnetic field of the CS is generated by three different structures:

- the pole expansion;

- the superconducting coils;

- the yoke.

The trim coils give only a small contribution (of the order of 0.1-1 %) to the total magnetic field but very important for the isochronism.

The superconducting coils, together with the yoke, provide the main magnetic field contribution, which is variable for different beams and they are used for the ion confinement. Instead, the pole expansion gives the azimuthal modulation used for the vertical focusing of the accelerated beams. The principle of the AVF (Azimuthal Varying Field) cyclotron was proposed for the first time in 1938 by L. H. Thomas [47] to overcome the problem of the insufficient vertical focusing in the classical cyclotron. The vertical focusing is further increased in the CS by the spiral shape of the iron sectors.

A view of the vertical cross section and median plane of the CS accelerator is presented in Fig. 2.4 and 2.5 respectively. Fig. 2.6 shows a picture from the top of the CS magnet.

Hereinafter, a description of the main components of the CS magnetic system is presented. More detail can be found in Ref. [46, 48].

2.2.1 The iron structure

The main parameters of the CS magnet are listed in Table 2.2.
The full magnet weight, including the sectors, is 176 tons.

The yoke is cylindrical with the inner and outer radius equal to 1340 mm and 1903 mm respectively. It is composed of pieces of steel with
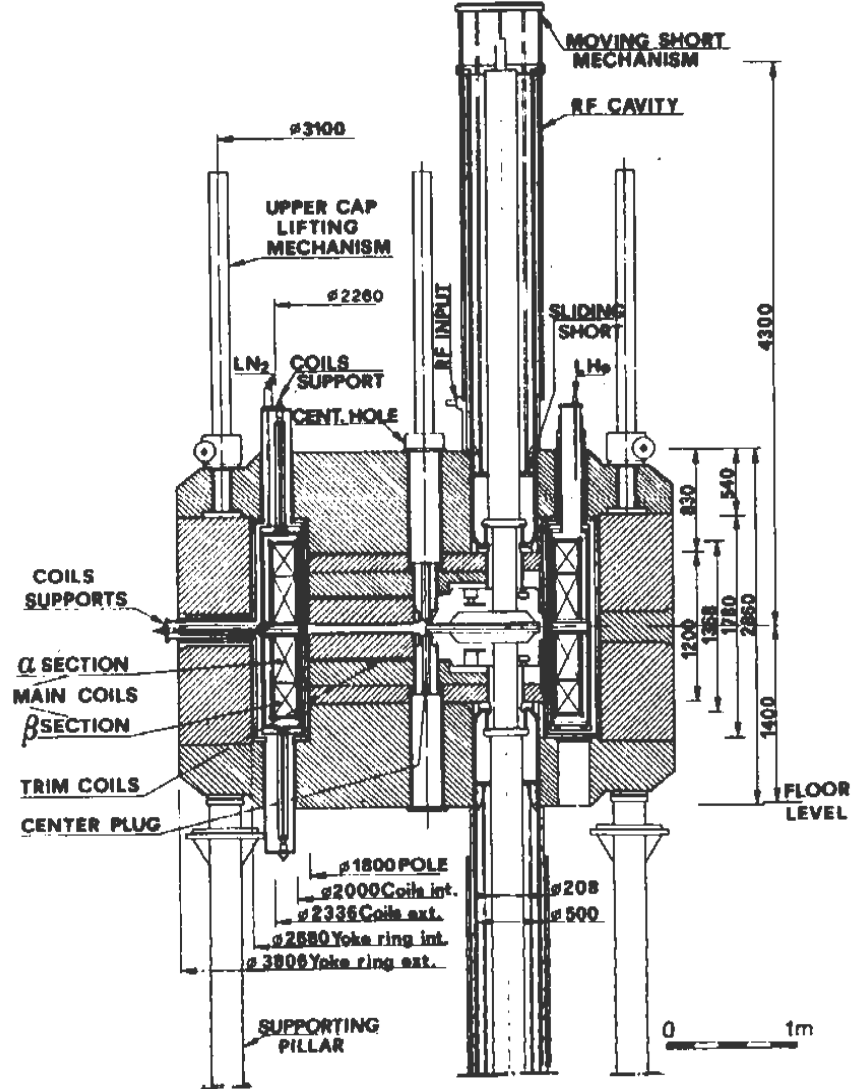
Figure 2.4: Sketch of the vertical cross section of the INFN-LNS Superconducting
Cyclotron. All dimensions are in mm.

very good magnetic properties (carbon content < 0.01 %): the upper
and lower cap and the return yoke to reduce the stray magnetic field.
The pole has a radius equal to 900 mm and extends up to 600 mm from
the median plane. The minimum hill gap is 86 mm and the maximum
valley gap is 916 mm.
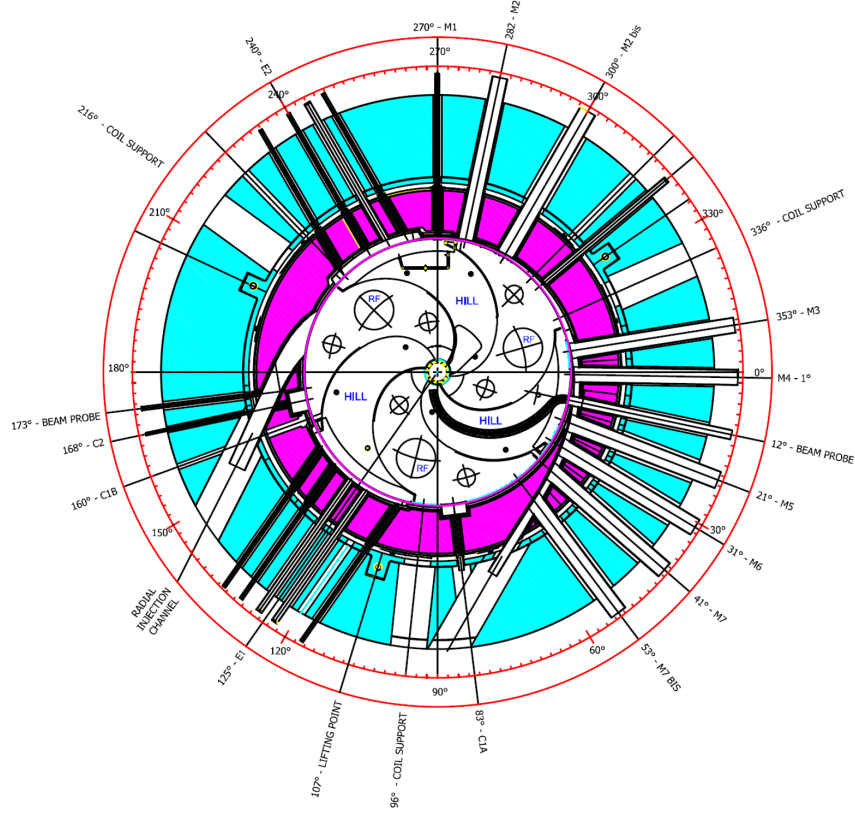
Figure 2.5: Sketch of the CS median plane. All the radial penetrations are visible.

The azimuthal width of the hills is 33° at the radius of 90 mm, beyond which it increases as the radius rises, achieving the maximum value of 52° in the region immediately before the pole radius. Also the spiral constant increases with rising radius, from 1/45.7 rad/cm to 1/31.4 rad/cm.

Each hill is composed of two parts 200 mm thick in order to provide space for winding the twenty trim coils around the upper part. The part of each hill closer to the median plane has rounded edges in order to facilitate the winding of the trim coils. A picture of the pole sectors with the three split hills is presented in Fig. 2.7.

In each valley various holes are provided for the RF cavities and for the leads of the trim coils, as shown in Fig. 2.5.

Shims of proper height are present in the valleys in order to correct the
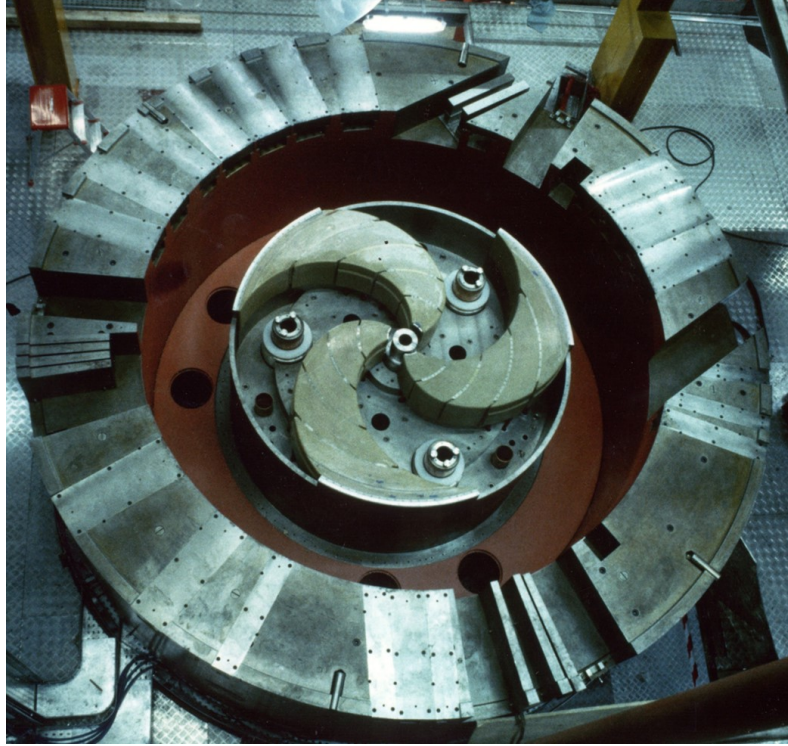
Figure 2.6: Picture from the top of the magnet of the CS.

Rotational symmetry	Three-fold
Steel	Carbon content $< 0.01\%$
Total weight	176 tons
Yoke inner radius	1340 mm
Yoke inner radius	1903 mm
Yoke full height	2860 mm
Pole radius	900 mm
Minimum hill gap	86 mm
Maximum valley gap	916 mm

Table 2.2: CS magnet parameters.

Figure 2.7: Pole sectors of the CS. Each hill is split in two parts. The upper part has rounded edge in order to facilitate the winding of the trim coils around it. The picture was taken in Milan before the installation of the CS in Catania.

iron imperfections in the pole sector and to produce the desired average magnetic field. The shim on the valley between the radii 875 mm and 900 mm, together with the inner wall of the vacuum tank (a ring with a 24 mm thickness and a vertical extension up to 60 mm from the median plane), are such that the radius of the isochronous orbits is very near to the pole radius.

A vertical central hole of 70 mm diameter is provided for the beam axial injection. The hole increases to a 250 mm diameter through the pole and the yoke to provide more room for the buncher, placed at 500 mm from the median plane. A centre iron plug, consisting of a cylindrical part and a hill part 33° wide is present to prevent that the flutter goes to zero quickly and then it provides some vertical focusing.

2.2.2   The superconducting coils

The isochronization of the magnetic field, for different ions to be accelerated to different final kinetic energy, is mainly obtained with the excitation of the two superconducting coils, since they produce up to 70 % of the total magnetic field while the contribution of the trim coils is only of the order of few hundreds Gauss.

The coils are subdivided into two independent sections so that their currents can be varied in order to obtain the radial gradient adjustment of the isochronous field, necessary for the acceleration of any ion within the CS operating diagram.

Figure 2.8 shows the sketch of the vertical section of the CS upper coil. The coil section closest to the median plane is named α and the other one β. In order to achieve a magnetic field level close to 5 T and the proper radial field shape, the coils are placed as close as possible to the median plane and to the pole. The internal and external radii of the coils are 1000 and 1168 mm respectively and the minimum distance from the median plane is 62 mm.

These values were chosen taking into account the constraints imposed by the radial penetrations needed for the extraction elements.

The size, position and sections subdivision of the coils were opportunely chosen, together with the optimization of the iron field, during the design study of the CS, in order to minimize the trim coil power throughout the operating range of the cyclotron. A low trim coil power is needed to reduce residual field errors and consequently make negligible the oscillations in the phase curve and of the focusing frequencies for the accelerated ions.

The minimization method is based upon the selection of two appropriate ions which can be thought as representative of the extreme isochronous fields required, in the operating range of the CS.

The isochronous magnetic $B_{iso}(r)$ field, required by a generic ion indexed

as the superscript i, can be written as:

$$B_{iso}^i(r) = B_{iron}(r) + F_\alpha(r)I_\alpha^i + F_\beta(r)I_\beta^i + \sum_{k=1}^{N} F_k(r)I_k^i + \epsilon^i(r) \quad (2.2.1)$$

where $B_{iron}(r)$ is the magnetic field generated by the iron configuration, $F_\alpha(\text{r})$, $F_\beta(\text{r})$ and $F_k(\text{r})$ are the form factors of the main coil sections and of the kth trim coil (N coils total) while I_α, I_β and I_k the corresponding currents and $\epsilon(r)$ is the field error with respect to isochronous field. If one evaluates equation 2.2.1 for the least and most relativistic particles in the operating range of the cyclotron, and then subtracts the two equations, it gets:

$$\Delta B_{iso}(r) = F_\alpha(r)\Delta I_\alpha + F_\beta(r)\Delta I_\beta + \sum_{k=1}^{N} F_k(r)\Delta I_k + \Delta\epsilon(r) \quad (2.2.2)$$

where $B_{iron}(r)$ is assumed to be equal for the two ions.

An ordinary least squares fitting procedure of the quantity $\sum_r [\Delta\epsilon(r)]^2$ permits to find the minimizing following conditions:

$$\epsilon^1(r) + \epsilon^2(r) = 0 \qquad \text{for every radius} \qquad (2.2.3)$$

$$I_k^1 + I_k^2 = 0 \qquad \text{for every trim coil} \qquad (2.2.4)$$

More information can be found in Ref. [49].

The minimization of the trim coil power imposes that the current density in the section β must be negative for the acceleration of fully stripped ions. The current density J_a in the α section varies between $+1500$ A/cm^2 and $+3500$ A/cm^2, the current density J_b in the other section goes from -1500 A/cm^2 to $+3500$ A/cm^2. Since the use of high currents leads to strong axial forces on the coils, also of opposite sign for different sets of currents, a careful analysis of the forces and stresses on the coils was carried out during the design study of the CS. The α section is always attracted toward the median plane, the β section is pushed away from the median plane for negative current densities. As shown in Fig. 2.8, a

set of Cu-Be tie rods are used to prevent the β coil axial lifting but also to produce a sufficient pre-load of the α section.

The axial suspension of the coils is made with three pairs (upper -lower) of 16 mm diameter Ti-alloy rods, of about 1 m length. The coils are wound with the double pancake technique and consist of 38 turns of 26 layers in the α section and 18 layers in the other one [50].

The maximum current density is $+3500$ A/cm^2 for both sections, corresponding to a total of $6.5 \cdot 10^6$ At. The main coils characteristics, included the cable features, are listed in Table 2.3.

In order to maintain the coils in the superconducting state, they are in a liquid helium bath at atmospheric pressure (T = 4.2 K).

The Helium vessel, where the superconducting coils are placed, is made of stainless steel and it is surrounded by a liquid nitrogen cooled ther-
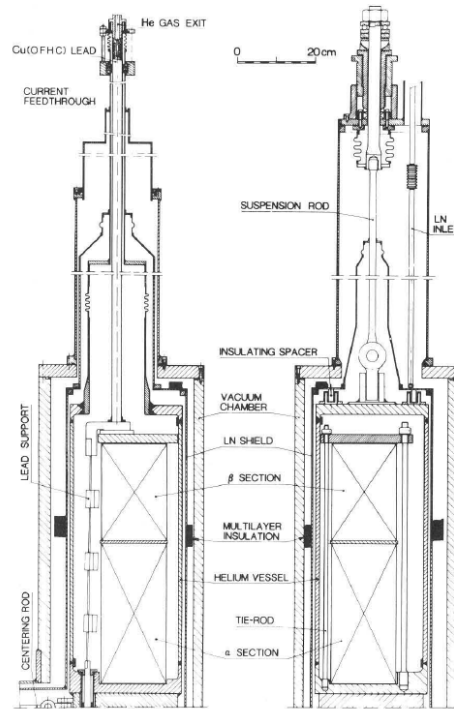
Figure 2.8: Coil and cryostat sections [50].

Max Ampereturn	$6.5 \cdot 10^6$ At
Max engineering current density	3500 A/cm^2
Internal radius	1000 mm
External radius	1168 mm
Minimum distance from MP	62 mm
Height of α section	364 mm
Height of β section	252 mm
Turns/pancake	38
Layers in α section	$2 \cdot 13$
Layers in β section	$2 \cdot 9$
Cable type	Nb-Ti insert in Cu cable
Overall Cu-Sc. ratio in the cable	20:1
Cable dimensions	$13 \cdot 3.5$ mm^2
Total conductor length	22.6 Km

Table 2.3: Main parameters of the CS coils.

mal shield and by the vacuum chamber. The outer wall of the vacuum chamber iron made, so it is part of the iron circuit. The coil position is fixed by axial and radial tie rods placed every 120°.

2.2.3 The trim coils

The twenty trim coils, wound around the upper part of each hill, are divided into five groups, separated by radial spacers and each one composed by four coils, as shown in Fig. 2.9 on the left. The trim coils are numbered starting from the CS centre. The coils, indicated by the numbers 3, 4, 19 and 20, are named harmonic coils, because of their harmonic contribution to the total magnetic field. The first two harmonic coils are placed immediately outside the central region for the beam centring, the

other ones in the extraction region.

All the trim coils are water cooled and covered by a thin isolating coating, as shown in Fig. 2.9 on the right. The maximum carried current is 500 A.

The squared cable section is not the same for all the trim coils, in particular the harmonic coils closest to the centre have a smaller cable section (side=3/16", hole diameter = 1/8") with respect to the other ones (side=1/4", hole diameter = 3/36") in order to reduce their azimuthal extent around the hill in the cyclotron center.
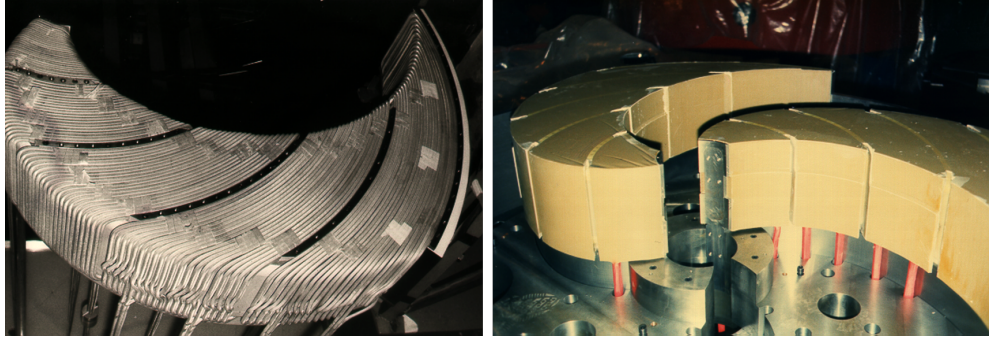
Figure 2.9: Correction trim coils in the INFN-LNS Superconducting Cyclotron. Five groups of trim coils, each one composed by four coils, are visible on the left. The thin isolating material coating the trim coils is visible on the right.

2.3 The extraction system

When the ions have reached their final kinetic energy, they are extracted from the CS by means of two electrostatic deflectors placed on two consecutive hills.

A horizontal constant electric field is present between the two electrodes of each electrostatic deflector. The beam is deflected when it enters the extractors, as shown in Fig. 2.10, because of the electric force acting on the beam particles opposite to the magnetic force inward directed.

The sketch of the CS electrostatic deflectors is presented in Fig. 2.11
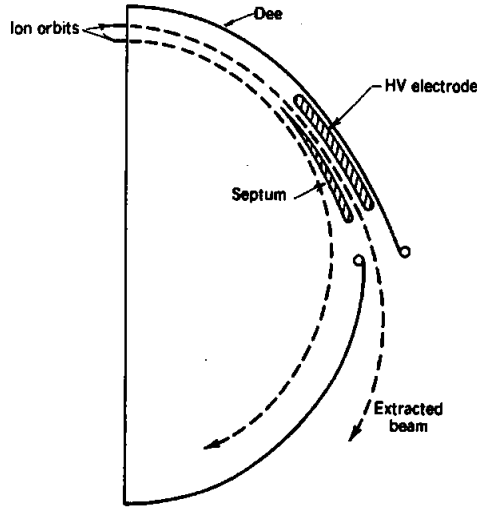
Figure 2.10: Sketch of the extraction from a cyclotron by electrostatic deflector. The electric field between the HV electrode and the septum, which is at zero potential, is radial.

on the left. The inner electrode of each extractor, called the septum, is placed between the last and second to last turn. It is on ground potential so that the inner orbits in the cyclotron are not affected. The distance between the septum and the other electrode is 6 mm.

The septum of the first electrostatic deflector is very thin (thickness of the order of 0.3 mm) to minimize the beam losses on the septum itself. It is water cooled and, furthermore, the beginning of the septum is V-shaped, as shown in Fig. 2.11 on the right, in order to better distribute the heat due to beam losses.

The other electrode of each extractor is on negative high potential, being that all the accelerated ions have a positive charge. The maximum voltage applicable is about –60 kV, corresponding to a limit on the electric field equal to 100 kV/cm.

The septum, screwed to the liners, is Tungsten made whereas the housing and the liners, surrounding the negative high voltage electrode, are made of OFHC copper.

Being the CS a multi-particle variable energy cyclotron, the magnetic
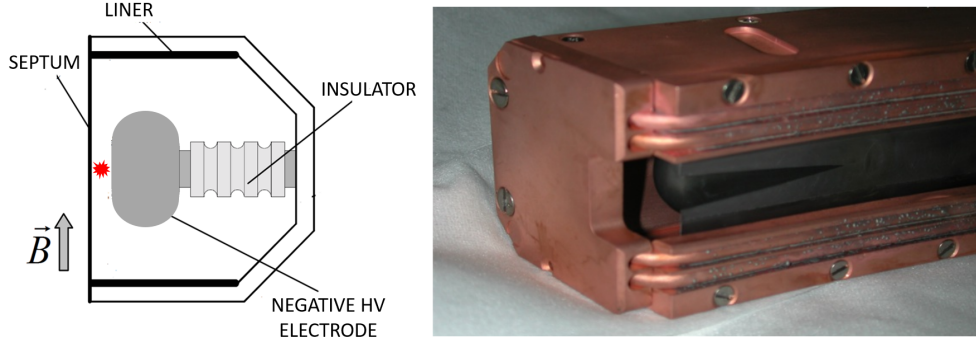
Figure 2.11: On the left, the sketch of the CS electrostatic deflectors with their main components. The red star represents the beam passing between the septum and the high negative voltage electrode. On the right, a photograph of the beginning of the first electrostatic deflector of the CS. The septum, screwed to the liners, is V-shaped in order to reduce the hit load from the beam.

field varies considerably from ion to ion, and the ions extracted at low and high magnetic field exhibit different orbit scalloping in the electrostatic deflectors [51]. In order to extract a large variety of ions with different energies, the CS electrostatic deflectors are radially movable over a range of about 30 mm. In addition, they are split in two parts of about same length connected by a swivel joint to adapt in shape to the different trajectories to be extracted. This solution is also adopted at MSU (Michigan State University) for the K500 cyclotron [52].

After passing the electrostatic deflectors, the ions enter into the fringing field of the magnet. In this region the beams are subject to a strong horizontally defocusing action, which is due to the negative gradient (in outward direction) of the magnetic field. In order to prevent the beam from diverging too much, passive magnetic focusing channels are placed along the extraction path, in particular inside the vacuum chamber and throughout the cryostat traversal. The first two magnetic channels, named M_1 and M_2, immediately follow the electrostatic deflectors. Other five magnetic channels, labelled M_3, M_4, M_5, M_6 and M_7, are placed along the extraction path in the fringing field of the third hill and

through the cryostat traversal. Another magnetic channel, named M_8, is inserted in the yoke exit.

The magnetic channels are composed of three small iron bars which are magnetized by the main field of the cyclotron. Due to the different requirements on the field and on the radial focusing along the extraction path, the magnetic channels are not identical. Only the magnetic channels from M_3 to M_7 have the same shape whereas the other ones are differently designed. Fig. 2.12 shows the vertical cross section of all the magnetic channels.

The bars are shaped and arranged in such a way that the magnetic field produced by them has an approximately constant positive gradient in outward direction normal to the beam. This field shape counteracts the defocusing action of the fringing field of the magnet. As an example, Fig. 2.13 shows the magnetic field and transverse gradient created by the magnetic channel M_1. Three iron bars, named C_{1A}, C_{1B} and C_2, are present to compensate the first harmonic perturbation due to the magnetic channels from M_1 to M_7.

Since the median plane penetrations through the cryostat were drilled before the magnetic field measurements, two extra holes, named $M_{2\ bis}$ and $M_{7\ bis}$, were designed during the study of the extraction from the CS as alternative positions for the magnetic channels M_2 and M_7 respec-
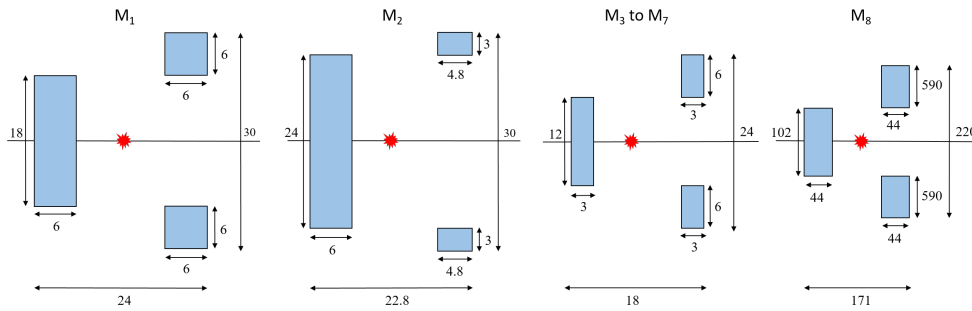
Figure 2.12: Vertical cross section of the magnetic channels of the Catania cyclotron. All dimensions are in mm. The red dots represent the beam position.

44
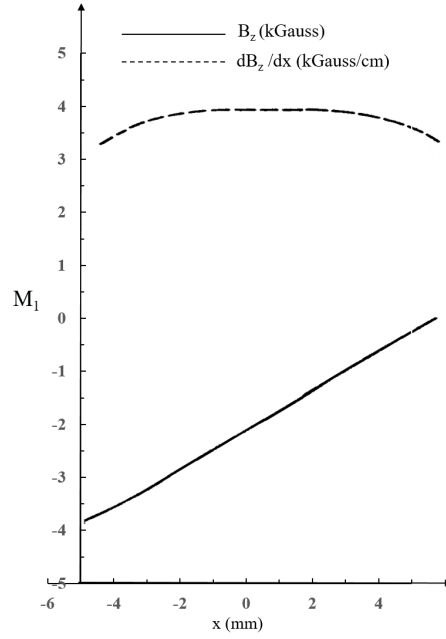
Figure 2.13: Magnetic field and transverse gradient created by the magnetic focusing channel M_1.

tively for the extraction of the more critical ions.

Figure 2.14 on the left shows the sketch of the CS median plane with all the elements of the extraction system. On the right, the penetrations in the yoke needed by the extraction system are shown.

The relevant parameters of the CS electrostatic deflectors are listed in Table 2.4.

The polar coordinate system assumed in Fig. 2.14 and in Table 2.4 is such that the polar angle θ increases for rotations in clockwise orientation, starting from the reference axis defined in Fig. 2.14, corresponding to $0°$.

2.4   The injection system

As already reported in the introduction, in the year 2000 the radial injection was replaced by the axial injection. This choice has permitted to

Figure 2.14: On the left, the sketch of the extraction system of the CS. On the right, the median plane view of the CS yoke with all the penetrations needed by the extraction system. The radial injection channel, no longer used, is also shown. The polar angle θ increases for rotations in clockwise orientation [51].

	θ (°)	R (cm)	$\pm \Delta$R (cm)	E_{max} (kV/cm)
E_1	104.00	85.76	1.32	100
	156.00	87.55	0.79	
E_2	222.00	88.28	1.00	100
	262.00	91.12	0.31	

Table 2.4: Main parameters of the electrostatic deflectors of the INFN-LNS Super-conducting Cyclotron: the initial and final azimuth, the average central ray position and the excursion around it at the two azimuths, the maximum electric field. The polar angle θ increases for rotations in clockwise orientation [51].

improve the performance of the INFN-LNS Superconducting Cyclotron, in terms of both beam intensity and energy, and to extend the number of the ion species that the CS was able to accelerate.

Indeed, the EXCYT project required acceleration of light ion beams (from C to Ne) with higher intensity with respect to those obtainable using the CS as a booster of the 15 MV Tandem. Furthermore, since

the Tandem requires negative ions for first acceleration, only atoms with positive electron affinity could be used.

The first upgrade of the CS was made possible by means of the installation in 1998 at INFN-LNS of a high performing superconducting Electron Cyclotron Resonance Ion Source, designed and constructed by INFN-LNS in collaboration with the CEA of Grenoble. This source, named SERSE, is currently operated at INFN-LNS and it is able to produce stable highly charged ion beams with higher intensities with respect to room temperature ion sources. In order to ensure the continuous operation of the cyclotron, a second ECRIS with room-temperature magnets, named CAESAR, was also installed a few years later.

A detailed description of the CS ion sources and of their characteristics can be found in reference [53].

The axial injection mode implied the replacement of the stripper system with the axial injection system composed by the spiral inflector and central region. An injection line was also designed and constructed for the beam transport from the ion source to the spiral inflector, used for the 90° bending of the beam onto the median plane.

In this section, a description of the components of the CS injection system, including the two ion sources and the injection line, is presented.

2.4.1 The SERSE ion source

The SERSE superconducting ion source is one of the most performing sources among those currently used in the various worldwide laboratories, being able to produce totally stripped Argon ions (Ar^{18+}) with a current of 0.2 μA and up to 2 μA of Xe^{36+} [54].

Figure 2.15 shows a picture of the SERSE ion source in its location at INFN-LNS. The plasma chamber is constituted by a 450 mm long aluminium cylinder with 130 mm inner diameter, closed by the injection and extraction flange at the two ends.

The magnetic field is generated by three superconducting solenoids (enabling axial plasma confinement) and by sextupole (enabling radial plasma confinement). All the coils are made of a superconducting cable Nb-Ti made. The magnet cooling system uses a 1310 mm long cryostat with a 1000 mm diameter containing liquid helium (LHe) at the temperature of 4.2 K. The superconducting magnetic system generates a magnetic field of $\sim$ 2.7 T at microwaves injection, while magnetic field at extraction is $\sim$ 1.6 T. Maximum radial magnetic field generated by the hexapole is 1.6 T. So high values of confining magnetic field enable to improve plasma confinement and therefore to increase the maximum charge state the source can generate.

Nominal operating frequency of the SERSE source is 18 GHz. The use of two microwaves generators (usually a klystron and a Traveller Wave Tube (TWT)) enables to work in Two Frequency Heating (TFH), improving the source performance [55].

The extraction of ions takes place through a system of electrodes, with a total extraction voltage of around 20 kV (maximum applicable voltage is 25 kV).

Once extracted, the beam is focused by a solenoid, while a 90° analysis magnet selects the desired charge states as a function of Q/A.

2.4.2 The CAESAR ion source

The normal-conducting CAESAR ion source was funded in 1997 and installed in 1999 at LNS. The availability of a second ECRIS has allowed the continuous operations of the LNS accelerator facility, leaving SERSE free for developments [53, 56].

A picture of CAESAR source at the INFN-LNS is shown in Fig. 2.16.

Normal conducting magnets generate a maximum magnetic field which overcomes 1.1 T either in injection and extraction region. Microwave power is produced by a klystron, operating in the range 14-14.5 GHz,

Figure 2.15: The SERSE ion source at INFN-LNS.

Figure 2.16: The CAESAR ion source at INFN-LNS.

while a second frequency, generated by a TWT at 18 GHz enables TFH operation.

The beam extraction is performed by means of a three electrode extraction system, able to operate up to a maximum voltage of 30 kV.

Table 2.5 lists the intensity of some beam generated by the SERSE and CAESAR ion sources.

Ion	SERSE [eμA]	CAESAR [eμA]
O^{6+}	540	720
O^{7+}	208	105
Ar^{16+}	21	2
Ar^{18+}	0.4	//
Kr^{22+}	66	10
Kr^{27+}	7.8	1
Kr^{31+}	0.2	//
Xe^{36+}	0.9	//
Au^{41+}	0.35	//

Table 2.5: Intensity of some beam generated by the SERSE and CAESAR ion sources.

2.4.3   The injection line

The injection beam line provides the transport of ions from the two external ion sources onto the median plane of the CS for their subsequent acceleration. At the final stage of transport, ions move along the symmetry vertical axis of the cyclotron within the hole in the magnet yoke and they are deflected onto the CS median plane by a spiral inflector. Figure 2.17 shows the injection beam line of the CS [57].

The beam injection line is composed of two parts. In the first one, the charge distribution analysis of the extracted ions and the subsequent

separation of the required beam are performed. The ECR ion source and the analysis magnet are component of this part.

The beam focusing in the first part of the injection line is provided by a solenoid installed between the ion source and the analysis magnet.

The second part of the beam injection line is composed of twelve solenoids and four quadrupoles. The solenoids are used for the beam confinement, the four quadrupoles allow the matching of the beam with respect to the optical properties of the cyclotron axial bore. The last ones are installed at the end of the horizontal section of the beam injection line, as shown in Fig. 2.17.

The vertical section of the beam injection line was designed in order to obtain beam envelope confinement and a small beam size at the entrance of the spiral inflector. It is composed of two couples of solenoids, one positioned quite close to the cyclotron yoke. This last one has a special
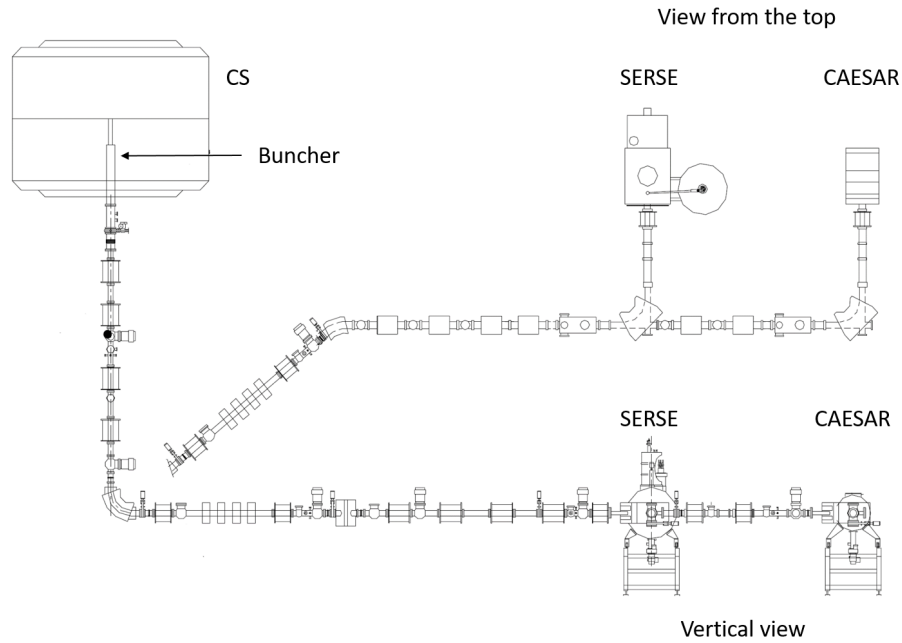

Figure 2.17: Layout of the axial injection line of the CS. Top and vertical view are shown.

iron yoke, designed by taking into account of the magnetization induced by the cyclotron stray field [58].

A buncher is installed in the vertical section of the beam injection line, inside the CS yoke at about 500 mm from the median plane [59]. Operating at the same RF frequency of the CS, it is used to compress the DC beam, generated by the two ion sources, into bunches. The buncher allows to increase the beam intensity of an estimated factor equal to three into 36°, the present RF phase acceptance of the CS central region.

The energy spread of the injected beam introduced by the bunching process is $\Delta E/E_{Buncher} = 7$ %.

2.4.4   The central region

The accelerating structure of the CS is composed of three spiralled dees, that are part of the RF cavities, positioned in the valley regions and of the RF liner, that is a contoured grounding cover, placed over the magnet pole. A RF electric field is present in the gap between the grounded copper plate covering the hill surface, the so-called dummy-dee, and the dee.

The dees extend radially from 100 mm out to the extraction radius.

The inner part (from r = 0 to 100 mm) is occupied by the central region. This consists of a set of electrodes attached to the dees and the dummy-dees driving the beams along the first two turns in the cyclotron, after their axial injection onto the median plane by a spiral inflector.

Figure 2.18 shows the full accelerating structure of the CS.

The design study of the CS central region in 1998 was carried out taking account of the need to accelerate ion beams intense enough for the production of secondary beams required by the EXCYT project [45, 60], still maintaining the possibility of accelerating each ion type in a wide energy range, within the operating diagram of the cyclotron.

Although the CS allows to accelerate ions using the harmonic modes of

Figure 2.18: Accelerating structure of the CS. The phase slit system is also visible.

acceleration 1, 2, 3 and 4, the present central region was designed to operate in second harmonic mode of acceleration $h = 2$. This means that the ratio of the frequency of the RF accelerating voltage, f_{RF}, to the ion's orbital frequency, f_0, is equal to 2. As already described in the first section of this chapter, the energy of the accelerated beams are in the interval 8-100 MeV/amu for $h = 2$.

The central region of the CS operates in constant orbit mode. This means that, for a given harmonic mode h, all the ions follow the same trajectory independently of their charge to mass ratio Q/A and of the magnetic field level B_0. This imposes a scaling law for the voltage of the ion source, spiral inflector and dees, as compared to a reference case [61] :

$$\frac{V}{\omega_0 \cdot B_0} = constant \tag{2.4.1}$$

where V is the peak voltage of the dees, ω_0 the orbital frequency of the ion and B_0 the magnetic field level in the cyclotron centre.

The quantity on the left in Eq. 2.4.1 is known as Reiser parameter.

The maximum voltage of the dees is used for the acceleration of ions on

the focusing line ($K_F = 200$) of the cyclotron (see Fig. 2.1). Therefore, any ion along this line can be assumed as reference ion with respect to which the scaling law can be applied.

The constant orbit mode operation do not allow an equivalent dynamic for all the beams since isochronous fields and focusing properties do not scale exactly with the field level. Therefore, the acceleration properties are very similar only in the first few turns for all the ion beams.

The constant orbit operation mode is almost mandatory when the central region has many electrodes crossing the median plane and reduced clearance, as in the case of the CS central region.

Pillars crossing the median plane are located at the first two turns of the CS, in particular three are mounted on the tips of the dees, the same number of grounded electrodes are connected to the tips of the dummy-dees. Figure 2.19 shows a picture of the central region of the CS.

The spiral inflector and central region occupy a very little space in the CS since the injected ions bend very strongly in the CS centre, due to the high magnetic field. In Fig. 2.19 only the pillars on the dummy-dees tips are visible.

Pillars are used in the central region of a cyclotron to reduce the transit time factor and to increase the vertical focusing.

The transit time factor takes into account the time variation of the RF electric field during particle transit through the accelerating gap.

It is a measure of the reduction in the energy gain caused by the sinusoidal time variation of the field in the gap.

For an accelerating gap of negligible length, the gap transit by a ion occurs in a very small time during which the variation of electric field can be considered negligible. In reality, each accelerating gap has a finite dimension and therefore the ion takes some time to reach the gap centre during which the electric field varies. As a consequence, a lower energy gain of the particle is expected. The smaller the energy of the ion, the

Figure 2.19: Central region of the CS. The housing surrounding the spiral inflector is also visible in the centre.

greater the transit time factor.

The shape, the size and the position of each electrode in the central region have to be set in order to provide good transport properties, in particular the centring and the vertical focusing of the beams. Indeed, during accelerating gap crossing, ions are affected by vertical focusing forces produced by the same RF field which is responsible for their acceleration. If an accelerating gap is well positioned with respect to the RF phase of the particle, it can act as an electrical lens providing some electrical focusing [62]. In addition, a small vertical gap could further help to obtain an efficient electric focusing in the vertical plane.

In the CS the vertical distance between the accelerating electrodes in the centre is 19 mm, six mm lower than the value outside the central region. The electrical focusing plays an important role in the cyclotron centre where the magnetic focusing tends to be very weak because the flutter goes to zero. The electrical focusing rapidly falls with increasing beam energy. However, after a few turns the magnetic focusing becomes sufficient to produce the vertical focusing of the accelerated ions.

A small magnetic field bump (of the order of few hundred Gauss) is present in the CS centre. The negative gradient of the bump has the

effect to create a RF phase slip improving the vertical focusing effects due to the electric field. The magnetic field bump is mainly generated by a centre cone and the fine-tuning of the current in the first two trim coils, wound around each hill, allows to adjust the magnetic field bump profile according to the ion to be accelerated.

The preliminary design of the CS central region was based on the new design of the central region of the MSU K500 cyclotron, which was upgraded to be coupled to the K1200 cyclotron [63].

The shape and position of the pillars were modified with respect to the MSU central region design according to the different ion species to be accelerated and their final kinetic energy to be achieved. Ions with charge-to-mass ratio Q/A equal to 0.5 accelerated to final kinetic energy of 100 MeV/amu were selected as reference ones since they require maximum source voltage and dee voltage [58].

2.4.5 The spiral inflector

The spiral inflector is an electrostatic device commonly used in the axial injection system of cyclotrons which use external ion sources, as in the case of the INFN-LNS Superconducting Cyclotron.

It is composed by two parallel electrodes at opposite voltage, gradually twisted in order to take into account the spiralling of the trajectory, induced by the vertical cyclotron magnetic field. The spiral inflector was invented by Belmont and Pabot, which derived the equation for the reference trajectory through the spiral inflector [64].

To study the spiral inflector, it is convenient to define the so-called optical coordinate system, moving along the central trajectory, with unit vector $(\vec{u}, \vec{h}, \vec{v})$. $\vec{v}$ points along the beam direction, $\vec{h}$ is parallel to the median plane and orthogonal to $\vec{v}$ and $\vec{u}$ is orthogonal to the vectors $\vec{v}$ and $\vec{h}$.

The design of the spiral inflector is such that the electrical field is always perpendicular to the velocity vector of the central particle and therefore this last one moves on an equipotential surface without any energy variation. This design is complicated mainly due to the electrical fringe fields at the inflector entrance and exit and the not uniform magnetic field in the spiral inflector volume.

The spiral inflector has two free design parameters that can be used to place the reference particle on the correct equilibrium orbit onto the median plane. These parameters are the electrical radius A and the so-called tilt parameter k'. A is the electrical radius of the trajectory which the ion would have if it were acted upon by an electric field of magnitude E_u:

$$A = \frac{m \cdot v^2}{q \cdot E_u} \qquad (2.4.2)$$

where m, q and v are respectively the mass, the charge and the velocity of the ion. A is also known as the height of the spiral inflector.

The tilt parameter k' represents a gradual rotation of the electrodes around the particle moving direction.

Figure 5.6 shows the spiral inflector of the CS. The design study of the CS spiral inflector was performed considering the same reference ions of the CS central region study, i.e. ions staying along the focusing line of the operating diagram of the CS, for which the injection voltage is equal

Figure 2.20: The spiral inflector of the INFN-LNS Superconducting Cyclotron.

57

to 30 kV.

The height of the spiral inflector is 27 mm and the maximum electric field between the electrodes is 22 kV/cm. The distance between the electrodes d is constant, being the tilt parameter equal to zero, and equal to 6 mm. The ratio between the width s and the gap d of the electrode surface, the so-called aspect ratio, is equal to 2. A copper housing, which surrounds the spiral inflector, allows to avoid the interaction between the RF cavities electric fields and the inflector electric field. The housing, shown in Fig. 2.21 together with the spiral inflector, has a exit circular hole of diameter equal to 4 mm.

Furthermore, a copper collimator, with a 6 mm diameter and placed at 44 mm from the spiral inflector entrance, allows to protect the spiral inflector electrodes from the ion hits.
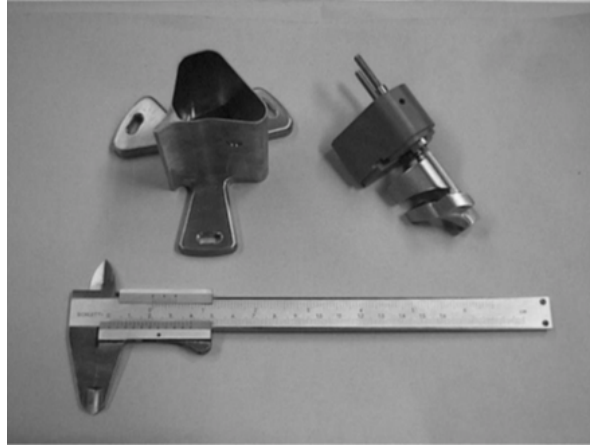

Figure 2.21: A picture of the housing and spiral inflector of the INFN-LNS Superconducting Cyclotron.

2.4.6 The phase selection

A phase selection is performed in the CS both in the central region and immediately outside of it.

The central region performs a first phase selection, reducing the phase range to approximately 35°, which corresponds to the acceptance of the

	d	6 mm
	s/d	2
Spiral inflector	A	27 mm
	k'	0
	Max E-field	22 kV/cm
Housing	Exit hole diameter	4 mm
Collimator	Hole diameter	6 mm
	Distance from SI	44 mm

Table 2.6: Main features of the spiral inflector, housing and collimator of the INFN-LNS Superconducting Cyclotron.

cyclotron. In the year 2000 a phase selection system was installed, together with the axial injection system, in order to perform fine phase selection outside the central region. This selection is performed introducing a radius-phase correlation. The excitation of the harmonic coils, placed immediately outside the central region to change the horizontal centring of the beam, together with the movement of the phase slits, allow to reduce the phase interval to about 10° and then to reduce the bunch length at about 1 nsec (33 MHz) or less.

The phase selection system is composed by three small Tantalum wedges, with a maximum thickness of 2 mm, one in each dee.

A mechanical system, host in the three main holes of the dees, allows the movement of each wedge on a inclined plane with a rise of 25 mm.

The wedge is completely on the median plane when it is placed at a distance from the CS centre between 190 and 210 mm.

The slits can also be removed from the median plane, going down inside the dees. Figure 2.22 shows one of the three phase slits and the mechanical system for its movement.

Figure 2.22: One of the three phase slits in the INFN-LNS Superconducting Cyclotron.

The phase selection system was installed in the CS in order to increase the extraction efficiency. As already mentioned in the introduction, since the CS is a compact cyclotron, turn separation plays an important role when the beam extraction occurs by means of electrostatic deflectors. Despite the reduction of the phase range of the beam to be extracted and the use of a first harmonic bump to excite the $\nu_r = 1$ resonance, there is no full separation between orbits at extraction. However, the phase selection process allows to intercept at low energy particles that would be stopped in the electrostatic deflectors reducing their activation. In addition, the CS is able to deliver beam bunches as short as one nsec (corresponding to a RF frequency of 33 MHz), often a strong condition required by many nuclear physics experiments at INFN-LNS.

Chapter 3

The upgrade of the INFN-LNS Superconducting Cyclotron

3.1 Main aspects of the project

The upgrade of the INFN-LNS Superconducting Cyclotron is an excellent possibility for the LNS laboratories to enrich its physics program of research with innovative experiments like NUMEN.
It poses ambitious goals that require innovative technical and technological solutions to overcome the current limitations of the LNS cyclotron for delivering high beam power up to 10 kW, first of all the low efficiency of the process of extraction by electrostatic deflectors.

The beam extraction by electrostatic deflectors is usually a critical process in cyclotrons because of significant losses that usually occur at the deflector septum during extraction. The radius increment per turn Δr_0 of the beam centre is related to the energy gain per turn ΔE_0 by the following relation:

$$\frac{\Delta r_0}{r_0} \cong \frac{1}{2} \frac{\Delta E_0}{E_0} \tag{3.1.1}$$

where E_0 is the kinetic energy at the radius r_0. Thus, the relative radial increase is only half the relative energy increase. Because of this, the

turns pile up closely together near the extraction radius. Therefore, it is difficult to extract a single orbit and beam losses on the septum of the electrostatic deflector could be important. The usual difficulties of the use of electrostatic deflectors are amplified in the compact cyclotron case due to the very small separation between turns at the extraction radius and the small space where the deflectors must be placed, which imposes constraints on their sizes.

On the contrary, in separated sector cyclotrons more space is available for the installation of large electrostatic deflectors, and, due to the large sizes of the accelerators, the separation between turns is significantly larger than in compact cyclotrons.

Usually, in compact cyclotrons harmonic extraction coils are used for excitation of the $\nu_r = 1$ resonance by a first harmonic in the magnetic field in order to facilitate in principle the beam extraction by electrostatic deflectors. Indeed, in the region where $\nu_r = 1$ a coherent beam oscillation is created: the beam is subject to radial kicks all in phases that have the effect to increase the beam oscillation amplitude linearly with turn number. In the INFN-LNS Superconducting Cyclotron the last two trim coils, wound around each hill, are used as harmonic extraction coils.

The beam extraction from the CS by electrostatic deflectors has always limited the maximum beam power that the cyclotron is able to deliver to the LNS users for their experiments. The limit is set by the extraction efficiency that is about 60% [65], due to the cyclotron compactness and thermal issues of the first electrostatic deflector, that further contribute to limit the maximum beam power that can be extracted from the CS. Indeed, despite the beam extraction occurs exciting the $\nu_r = 1$ resonance, the last orbit is not fully separated from the previous ones and thus part of the beam power is dissipated on the septum of the first electrostatic deflector.

At the beginning of 2000s, the use of the CS also for delivering ion beams

for the CATANA [66] and EXCYT facilities at INFN-LNS, which were developed respectively for the proton treatment of the ocular diseases like uveal melanoma and the production of radioactive ion beams, required the redesign of the initial electrostatic deflectors in order to improve the extraction process in terms of extraction efficiency, maximum deflected beam current and beam current stability [67].

The first deflector was redesigned in order to improve the thermal exchange by water cooling up to a beam power of 500 W, value required by the EXCYT project. The septum was redesigned with a "V-shaped" entrance side in order to dissipate the beam power loss on a larger surface of the septum, as reported in Chapter 2. In addition, the new septum was made in Tungsten and no longer in Tantalum, as in the first version, for its better thermal properties. Despite the efforts, the first electrostatic deflector begins to be less reliable when beam loss exceeds a power of 100 W.

The stripping extraction is a valid solution to achieve a higher extraction efficiency, also close to 100%, for the set of light-medium ion beams with mass number $A leq 40$ and energy higher than 15 MeV/amu required by the NUMEN and FRAISE projects.

The advantages of the stripping extraction compared to the extraction by electrostatic deflectors is the lack of the turn separation requirement. In order to extract the beam, each particle passes a thin stripper foil (usually Carbon made) by which one or more electrons are removed from the ion. Obviously, for that not completely stripped ions have to be accelerated. After stripping, the charge state of the ion changes and correspondingly its magnetic rigidity. The orbit of the ion after the stripping process is totally different from the closed one.

The relation between the local radius before (ρ_b) and after (ρ_a) stripping process is given by:

$$\rho_a = \frac{Z_b}{Z_a}\frac{m_a}{m_b}\rho_b \tag{3.1.2}$$

where m_b and Z_b are the ion mass and particle charge before stripping and m_a and Z_a are the ion mass and particle charge after stripping respectively. m_a and m_b are always the same, except in the case of H_2^+ which is stripped into two protons. The ratio Z_a/Z_b is usually named as the stripping coefficient.

The stripping extraction of H^- ions and molecular hydrogen H_2^+ is used to deliver proton beams by commercial cyclotrons fabricated for example by IBA (Cyclone 30, C18/9, C10/5) and General Electric (PETtrace). Protons are mostly used for the production of short-lived radioisotopes for medical diagnosis and for positron emission tomography.

Positive heavy ion beams can be also extracted using the stripping extraction, as in the case of the AVF cyclotrons of the Flerov laboratory [68]. After the stripping process, the heavy ion moves on an off-center single turn orbit, that depends on the radial and azimuthal position of the stripper foil and on the ratio between ion charge after and before stripping. For a better understanding, Fig. 3.1 shows, as example, the reference particle orbits of light ion beams with stripping coefficient from 1.35 up to 2 extracted by stripping at energies from 35 MeV/amu up to 50 MeV/amu from the U400 cyclotron of the Flerov laboratory [68]. For each ion species and stripping coefficient, the stripper position has been chosen in order that all the extracted beams exit the cyclotron in a common position and with the same position.

In the case of H^-, we have $H^- \rightarrow H^+ + 2e^-$ and the local radius of curvature changes sign. Due to this the stripped particle is immediately deflected outward, away from the cyclotron centre. When heavy ions penetrate through the stripper foil of thickness x, charge-changing collisions involve a number of different processes. It is possible to distinguish three main mechanisms for fast projectile ions: i) Coulomb capture ii) radiative capture and iii) excitation to continuum. Therefore, the charge-state composition of the beam will vary because of capture and loss events and,

for each value of x, certain relative charge-state populations will be observed. When x becomes large enough, the charge state distribution do not change further and equilibrium is reached. This is referred to as the equilibrium charge state distribution and the stripper thickness for which it starts to occur is named the equilibrium thickness of the stripper.

Table 3.1 shows the equilibrium charge fractions of the ^{12}C, ^{16}O and
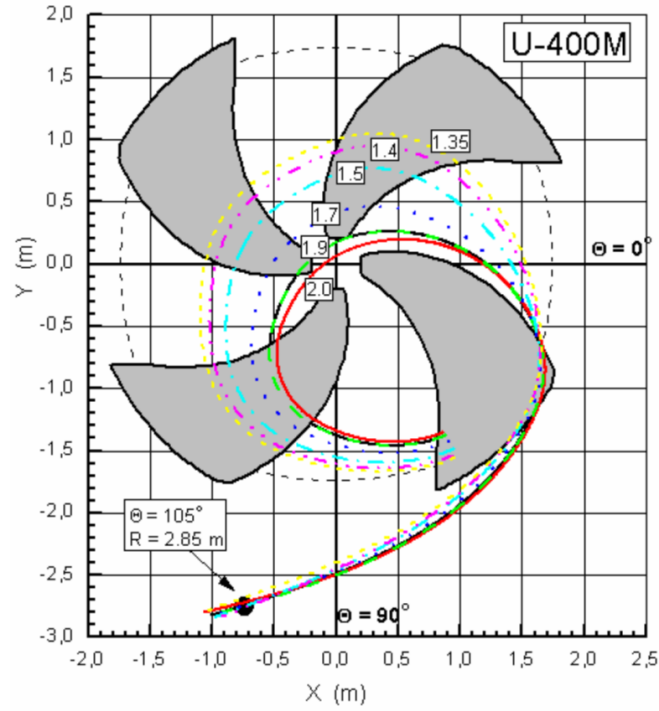
Figure 3.1: Reference particle orbits of light ion beams with stripping coefficient from 1.35 up to 2 extracted by stripping at energies from 35 MeV/amu up to 50 MeV/amu from the U400 cyclotron of the Flerov laboratory. All the extracted beams exit the cyclotron at the same position and with same direction [68].

^{20}Ne few-electron ions with energies higher than 15 MeV/amu after passage through a Carbon foil. The expected equilibrium charge fraction F(Q) is almost 1 when the ion charge Q is equal to the nuclear charge Z after the stripping process [39]. This means that, accelerating the few-electron ion beams reported in Table 3.1, the percentage of ions fully stripped after the stripping process is higher than 99%. Consequently, it

Ion	Energy	Charge fraction		
	[MeV/amu]	F(Z-2)	F(Z-1)	F(Z)
C	15	$1.74 \cdot 10^{-7}$	$8.35 \cdot 10^{-4}$	0.99917
	20	$2.56 \cdot 10^{-8}$	$3.20 \cdot 10^{-4}$	0.99968
O	15	$2.48 \cdot 10^{-6}$	$3.14 \cdot 10^{-3}$	0.9969
	20	$4.18 \cdot 10^{-7}$	$1.29 \cdot 10^{-3}$	0.9987
	30	$3.50 \cdot 10^{-8}$	$3.74 \cdot 10^{-4}$	0.99963
Ne	15	$2.00 \cdot 10^{-5}$	$8.90 \cdot 10^{-3}$	0.9911
	20	$2.66 \cdot 10^{-6}$	$3.26 \cdot 10^{-3}$	0.9967
	30	$2.26 \cdot 10^{-7}$	$9.51 \cdot 10^{-4}$	0.99905

Table 3.1: Equilibrium charge fractions F(Q), with Q equal to (Z-1), (Z-2) and Z, for C, O and Ne ions with energies higher than 15 MeV/amu, after passage through a Carbon foil [39].

is foreseen to achieve an extraction efficiency higher than 99% for these ion species and energies of the beams required by the NUMEN project. However, the new extraction method would be very efficient also for the ion beams of interest of the FRAISE project for RIBs production, i.e. medium mass nuclei with mass number A $\leq$ 40.

All the other ion species inside the operating diagram of the CS and currently accelerated by the cyclotron will continue to be extracted by electrostatic deflectors.

Although the extraction by stripping allows to achieve high extraction efficiency, its application is not trivial in the case of multi-particle variable energy cyclotrons. There are two effects that need to be considered in the case of stripping extraction: (i) the trajectories of accelerated ions with different masses, charge states and energies highly differ from each other after stripping, as shown in Fig. 3.1, and (ii) large beam ra-

dial and vertical envelopes are expected. Therefore, the exit channel is usually larger than the one requested for the extraction by electrostatic deflectors. Moreover, the individuation of the extraction channel position requires careful studies due to the large variety of ions to be extracted at different energies.

These difficulties are amplified in the LNS cyclotron because of the small distance of the superconducting coils from the median plane that reduces significantly the vertical space available for the extraction channel. Moreover, all the modifications to be apported in the LNS cyclotron have to not mechanically interfere with the existing structure of the CS and of its components already installed in the cyclotron since the CS has to continue to deliver all the ion beams currently demanded by the LNS users. The CS has already an extraction channel, that is currently used for the beam extraction by electrostatic deflectors. However, its current dimensions would not allow also the exit from the CS of the high power beam extracted by stripping and thus its enlargement should be necessary.

It is planned the use of two independent channels for the ion beams exit from the CS, the present one to be used for the extraction by electrostatic deflectors and a new one for the stripping extraction, with a larger horizontal and vertical size than the existing one. This solution should be less critical than the enlargement of the existing extraction channel to be used for both extraction mode. Indeed, the existing extraction channel is drilled through the cryostat traversal. The strong attractive force between the coils could produce serious deformations of the Liquid Helium (LHe) vessel inside the cryostat if a larger extraction channel is drilled through the LHe vessel. Moreover, the use of the existing extraction channel would not facilitate the extraction by stripping of the NUMEN ion beams. Indeed, a feasibility study of the stripping extraction from the CS demonstrated that the fast fall-off of the magnetic fringing field, during the ion beam transit in the existing extraction channel, has the

effect to highly defocus radially the beams and a high number of passive magnetic channels (from 5 to 8) with gradient up to 2.5 kG/cm would be necessary in the channel to prevent the beams diverges too much.

In order to limit the defocusing effect, the extraction channel has to be shorted as possible. A new extraction channel, rotated with about 30° with respect to the existing one, would facilitate the extraction by stripping of all the NUMEN ion beams [69, 70].

Part of this thesis has dealt with the study of the stripping extraction from the CS finalized to individuate the features of the new extraction system, in particular the position of the stripper foils for all the considered ion beams, the features of the new extraction channel and the field value and gradient of the passive magnetic channels to be used in the new exit channel for all the considered ion beams.

The results of the study are reported in detail in Chapter 4.

Hereinafter, the most important results of the study are briefly described for a better understanding of the CS modifications planned within the upgrade project of the LNS cyclotron and described in this chapter.

In order to facilitate the design of the new extraction channel, a common exit point from the CS for all the ion beams to be extracted by stripping has been set. At this point a new beam transport line is foreseen, as explained in Section 3.5.

The sizes of the new extraction channel larger than the existing one implies the replacement of the existing superconducting coils with new ones with smaller height in order to obtain more axial room for the new extraction channel but, at the same time, the new coils have to produce the same "field form factor" of the existing ones, as described in Section 3.2.

The new extraction channel simplifies the extraction by stripping of all the NUMEN ion beams because only two passive magnetic channels are necessary inside it and gradients lower than the ones necessary in the

existing extraction channel are required for all the ion beams.

The values of the field and gradient of the new passive magnetic channels have been individuated and are the same for all the ions to be extracted by stripping, as reported in Chapter 4. However, the iron profile of the passive magnetic channels able to generate the required gradients is not yet well-defined. Indeed, the study of the passive magnetic channels, together with the iron compensating bars, is ongoing at LNS laboratories. For this reason, they will be not discussed in this thesis.

Two areas where to place the stripper foils have been individuated during the study of the stripping extraction from the CS, one of which is coincident with the present position of one of the two electrostatic deflectors. Moreover, the new extraction channel would interfere mechanically with the handling system of the electrostatic deflector placed on the hill.

This implies a technological effort to find solutions, from the mechanical point of view, that allow the extraction of ion beams from the CS by two different extraction mode. Therefore, the stripping extraction from the CS implies substantial changes in the cyclotron.

Moreover, the improvement of the performance of the ion sources, injection line and central region and the replacement of the liners with new ones are other important aspects of the project of the CS upgrade, all finalized to further enhance the performance of the LNS cyclotron, in addition to the stripping extraction.

Hereinafter, the main aspects of the project of upgrade of the INFN-LNS Superconducting Cyclotron are presented in more detail.

3.2   New cryostat and main coils

The size and position of the new extraction channel in the CS is not compatible with the structure of the existing superconducting magnet for two reasons: (i) more axial space around the median plane is required for the new extraction channel and, consequently, the closest to the mid-

plane end of the alpha coils has to be moved from $z_{min} = 62$ mm, as in the existing magnet, to at least $z_{min} = 90$ mm and (ii) the new extraction channel is rotated with about 30° with respect to the existing one, according to the results of the study of the stripping extraction from the CS reported in Chapter 4.

The replacement of the cryostat and the main coils with new ones compatible with the new extraction channel is the key point inside the project of the CS upgrade for two reasons: (i) the technological efforts required to fit an already existing structure and (ii) the considerable cost.

The conceptual design of a new cryostat including new superconducting coils for the existing LNS cyclotron has been performed by the Massachusetts Institute of Technology (MIT) in collaboration with the LNS laboratories [71]. The magnetic, thermal and structural analysis for evaluating the feasibility and critical characteristics of the magnet structure were performed. Two constraints have been taken into account during the design study performed by MIT: (i) the new cryostat has to fit in the existing iron yoke of the CS and (ii) for each of the coils, the "field form factor", defined as the magnetic field calculated without iron at the median plane, has to match that of the respective coil of the existing magnet up to the extraction radius, i.e. up 900 mm, with an accuracy better than 0.1%.

In order to obtain more vertical space for the new extraction channel, new main coils with a lower height will be used. The conductors have been designed with an overall current density of 54 A/mm² and no longer with the present value of 35 A/mm².

The increase of the overall current density is compatible with the use of epoxy impregnated (potted) coils. The choice of this type of coils is primarily due to its more conventional design leading to a lower cost of manufacturing. The decrease of the coil height and the use of epoxy impregnated coils would allow to replace the current tie-rods (see Fig. 2.8),

used to prevent radial displacement of the main coils, with a different compression system, composed of a set of compression bolts placed on the top of the upper beta coil and on the bottom of the lower beta coil, as shown in Fig. 3.2.

The elimination of the tie rods from the LHe vessel allows for a remarkable reduction of the LHe vessel radial sizes with the advantage of increasing the separation between the LHe vessel and the room temperature wall of the cryostat and consequently a significant reduction of the LHe and Nitrogen consumptions is achieved.
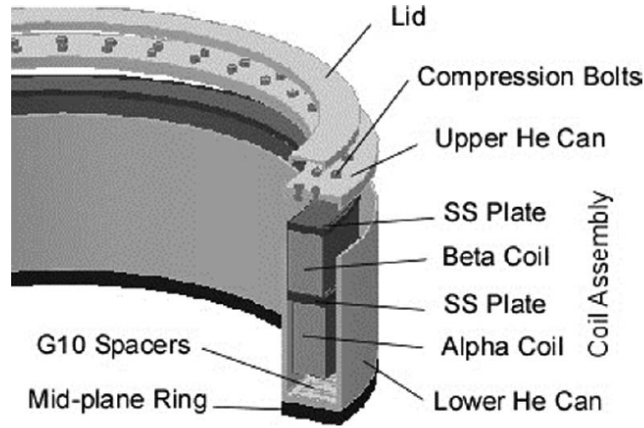
Figure 3.2: Compression bolts together with the coil assembly and Helium can[71].

3.3   Main modifications of the median plane

The extraction by stripping of high intensity ion beams from the CS implies substantial modifications of the median plane of the LNS cyclotron. A magnetic and mechanical analysis for evaluating the feasibility and critical characteristics of the new extraction channel is ongoing at INFN-LNS [72].

Fig. 3.3 shows the layout of the current median plane of the CS and of

the new one after the modifications required by the CS upgrade, according to the mechanical study ongoing at LNS laboratories.

The new extraction channel, that is rotated with about 30° with respect to the existing one, has dimensions larger than the present one used for the extraction by electrostatic deflectors. According to Fig. 3.3, its position within the CS would mechanically interfere with the position of one of the lifting point of the cryostat chamber. This incompatibility has forced to change the position of the lifting point of the cryostat chamber from the current one, corresponding to 107° in the reference system used in the figure, to 90°. Due to the small space in the area between 90° and 110° for placing both the lifting point of the cryostat chamber and one of the horizontal coil support, the position of this last one and, consequently, also of the other two have to be changed.

The new position of the horizontal coil supports are reported in Fig. 3.3 below. The placement of the horizontal coil supports in their new position is possible only suppressing the magnetic channels named M_2 and M_7.

They are part of the existing system of extraction by electrostatic deflectors but have never been used. The position of new extraction channel also interferes mechanically with the handling system of the first electrostatic deflector and of the existing magnetic channel M_8. Solutions to these mechanical problems are under study at INFN-LNS.

The mechanical interference between the new extraction channel and the handling system of the first electrostatic deflector could be solved welding the new extraction channel with the deflector penetrations and a flange, as shown in Fig. 3.4. This would not have critical consequences because all the components are steel made. Two interchangeable extraction chambers to be coupled with the terminal flange of the assembly have been designed, according to each extraction mode. Moreover, the handling system of the stripper foils interferes mechanically with the first
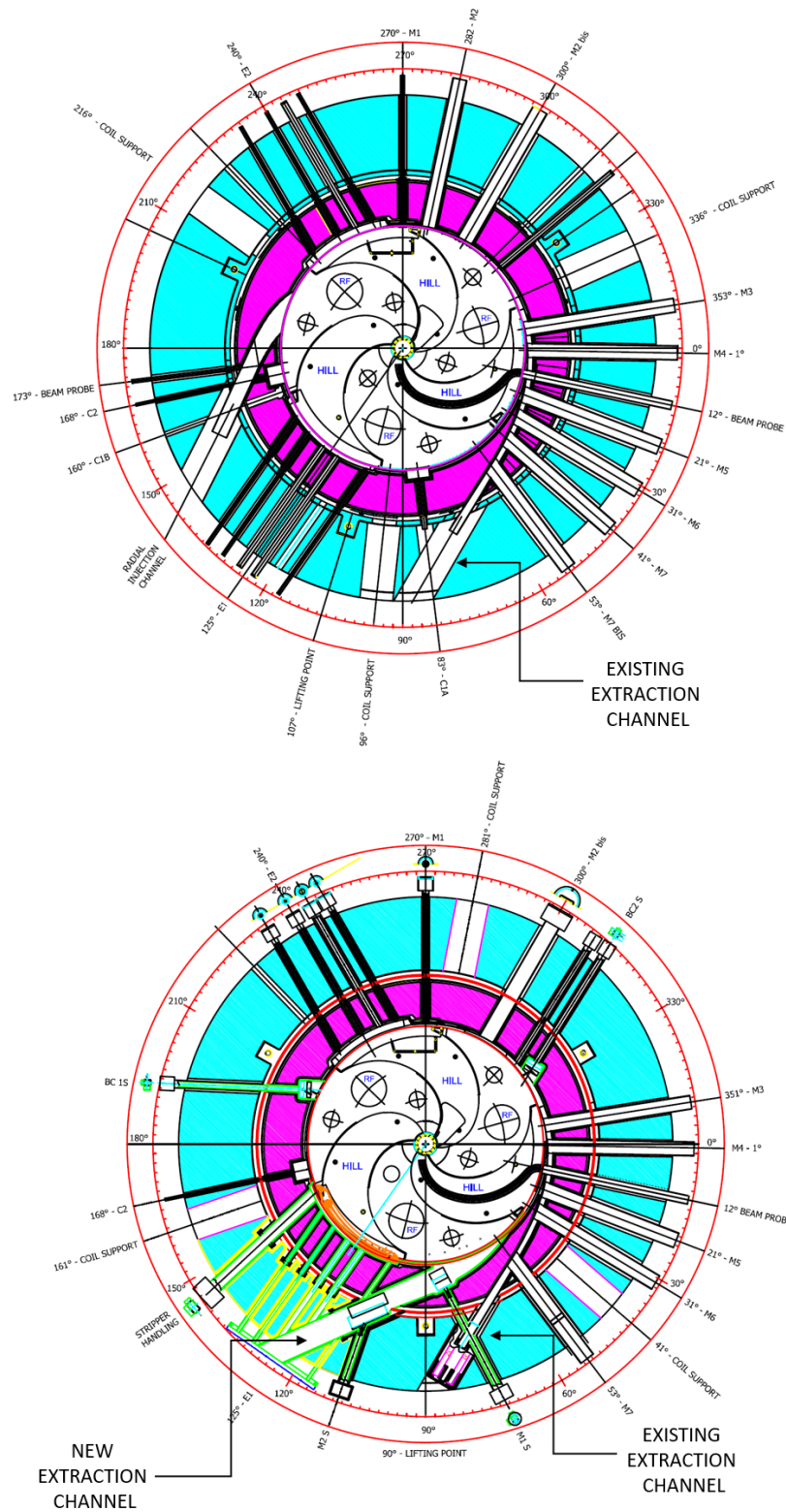
73

Figure 3.3: Current median plane (above) and new median plane of the LNS cyclotron after the modifications required by the CS upgrade (below).

electrostatic deflector. Because of this, it is planned to extract by stripping intense ion beams approximately six months per year and, for the remaining time, the LNS cyclotron will deliver ion beams to the LNS users using the two electrostatic deflectors.

Other modifications to the CS median plane present in Fig. 3.3 are: (i) the elimination of the channel for the radial injection from the Tandem, no longer used since the year 2000, and (ii) the presence of new penetrations for allocating the handling system of the new passive magnetic channels, named as M1 S and M2 S, and of the new iron bars, named as BC1 S and BC2 S, used to compensate the first harmonic perturbation due to the new magnetic channels.

3.4 New liners

The replacement of the existing liners with new ones is foreseen within the project of the LNS cyclotron in order to improve the vacuum in the acceleration chamber of the CS. Indeed, vacuum level worsening of about one order of magnitude has been observed after 24 years of operation of the LNS cyclotron.

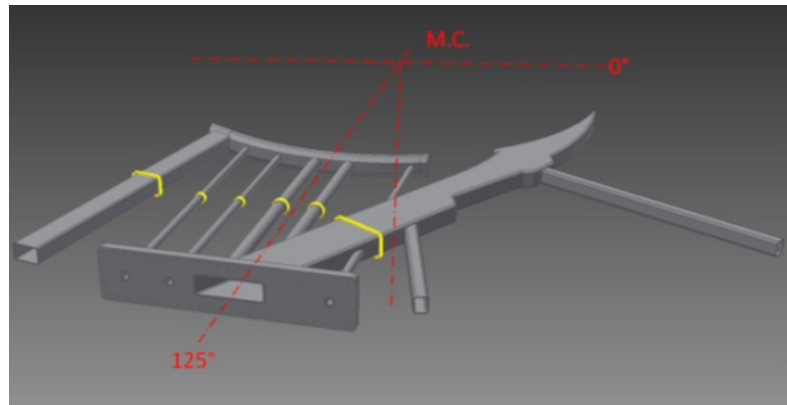The upper and lower liners constitute a copper skin covering the hills

Figure 3.4: New extraction channel assembled to the penetrations of the first electrostatic deflector of the LNS cyclotron. [72]
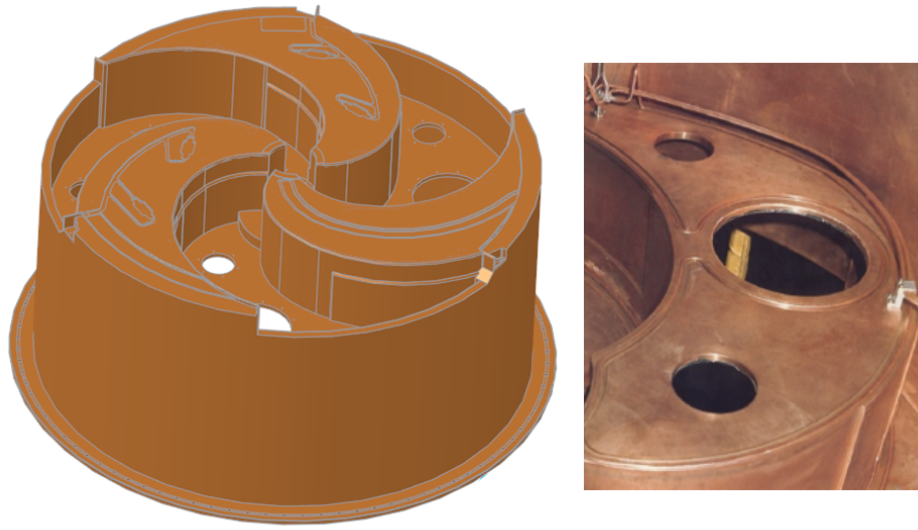
74

Figure 3.5: Liner of the LNS cyclotron. On the left, the 3D drawing of the lower liner is shown, on the right cooling groves are shown.

and valleys of each pole and closing the RF and the vacuum systems.

Fig. 3.5 on the left shows the 3D design of the lower liner.

Each liner is made of welded Cu sheet of different thickness.

Water cooling pipes are brazed along the contours of the three plates that cover the hills, on the bottom of the valleys and around the aperture of the coaxial cavities. Fig. 3.5 on the right shows cooling grooves on the bottom of a valley. The sheet covering the hill plates is quite thick (15 mm), because it is equipped with grooves for phase probes that have never been installed.

The liners separate the acceleration chamber, that is also delimited by the inner wall of the cryostat, from the below regions that enclose the magnet poles and the trim coils wound around each hill.

The pressure inside the acceleration chamber have to be low, at least of the order of 10^{-7} mbar. High vacuum is essential to apply high voltages on the accelerating electrodes as well as to mitigate beam losses by scattering of ions with any other gas molecules during beam acceleration.

A differential pumping is provided in the space below the RF liners and the typical pressure inside this region should be about 10^{-1} mbar.

Recently, an increase of the pressure in the acceleration chamber have been observed simultaneously to the worsening of the vacuum in the region below the liners. The reason behind this is the presence of vacuum leaks through some welded joints of the liners.

It is important to improve the primary to secondary vacuum isolation, especially in view of the high intensity beams circulating in the CS after the upgrade of the accelerator. Indeed, vacuum leaks could have the negative effects to increase beam losses during acceleration and the probability to have sparking problems of the RF cavities, thus reducing the reliability of the CS.

The idea is to use new techniques nowadays available for the liner construction in order to avoid or reduce as much as possible the welding of the liner parts. Also the possibility to machine the new lower and upper liners as a single piece and no longer as an assembly of welded pieces is under evaluation at LNS. Nowadays however, with the wide availability of computer controlled milling machines, this should be simpler than in the past.

The lack of welding, especially in critical areas connecting two or more parts of the liners would reduce the probability to have in the future problems of vacuum leaks as the present ones.

The replacement of the liners with new ones is also a good opportunity to increase the vertical gap inside the acceleration chamber from the present value of 24 mm up to 26-27 mm in order to take into account the larger sizes of the accelerated high intensity ion beams. In order to achieve this, it is planned to reduce the thickness of the liner plates covering the hills of about 1.5 mm. Obviously, also the accelerating electrodes, the so-called dees, have to be slightly modified according to the increment of the vertical distance between the lower and upper liners.

The increase of the vertical gap of the acceleration chamber would allow to reduce beam losses and to increase the chamber conductance e therefore the improvement of the vacuum in the region crossing by the ion beams.

3.5 A new beam transport line and fragment in-flight separator

A new beam transport line, that connects the new extraction channel to the existing beam transport line for delivering the beams to the LNS experimental halls, is under study at LNS laboratories [73].
The existing beam transport line will be maintained considering that the CS has to continue to deliver to the LNS users the low power beams that currently accelerates. Figure 3.6 shows the layout of the LNS cyclotron equipped with the existing beam transport line and the new one to be used for the transport of high power beams extracted by stripping.

The new beam transport line starts at the exit of the new extraction channel, corresponding to the common exit position from the CS of all the beams extracted by stripping, and transports the ion beams up to the so-called achromatic waist position, where here it connects to the existing beam transport line, as shown in Fig. 3.6.
According to the layout reported in Fig. 3.6, the first element of the new extraction line is a steering magnet, an active device for the adjustment of the beam direction in a range of $\pm 0.5°$. It has an effective length of about 300 mm and the requested magnetic field is lower than 8 kG.
The steering magnet is followed by two quadrupoles, named as Q1 and Q2 in Fig 3.6, and by two bending magnets, named as D1 and D2 in the same figure, with a horizontally focusing quadrupole Q3 in between.
This first part of the beam transport line has the role to cancel the

energy-position and energy-angle correlations of the incoming ion beams (double achromatic system).

After this section, two additional quadrupoles, named as Q4 and Q5, reduce the vertical beam envelope size to a value smaller of 26 mm, which is the vertical gap of the vacuum chamber of the existing bending magnet ED1. Finally, three quadrupoles, named as Q6, Q7 and Q8, that are also part of the existing beam transport line, produce a small beam spot at the achromatic waist position.

The new beam transport line is designed for the transport of beams with a maximum magnetic rigidity of 2.7 T · m and with a normalized emittance of 1 π mm-mrad. Figure 3.7 shows the radial and axial beam envelopes and the horizontal dispersion along the beam transport line for the beam of fully stripped ^{20}Ne ions extracted at the energy of 71 MeV/amu, that is one of the ion beams for which a high intensity is required.

The upgrade of the LNS cyclotron opens new perspectives for the production of radioactive ion beams, as described in Chapter 1.
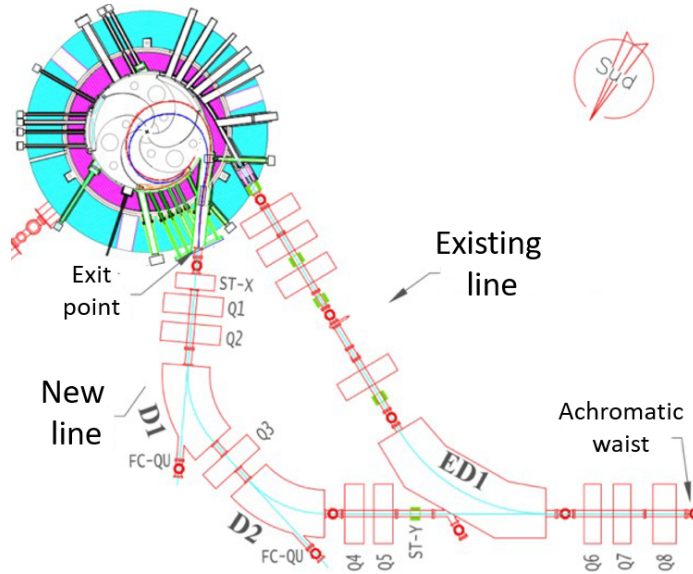

Figure 3.6: Layout of the LNS cyclotron equipped with the existing beam transport line and the new one to be used for the transport of high power beams extracted by stripping [73].

Due to the expected high power beams delivered by the upgraded CS, radio-protection issues impose to place the fragment separator in a position different from the present one, shown in Fig. 3.8, because it would be not possible to efficiently shield this area. In order to maintain the possibility to deliver the beams in the largest possible number of target positions, FRAISE, the FRAgment In-flight SEparator, will be installed in the area in which the 20° and 40° LNS experimental halls are currently present. This area is indicated by a circle in Fig. 3.8.

According to performed simulations, a primary beam power up to 2 kW can be efficiently and safely used in this new configuration [74].

The preliminary design of FRAISE, that allows to deliver RIBs to the CHIMERA and MAGNEX experimental halls, has a symmetrical configuration and consists of 4 dipoles and 6 quadrupoles. It is designed in order to have an achromatic beam line and to reduce as much as possible the high order aberrations of the beam line, also thank to the use of three sexstupoles. The layout of FRAISE is shown in Fig. 3.9.
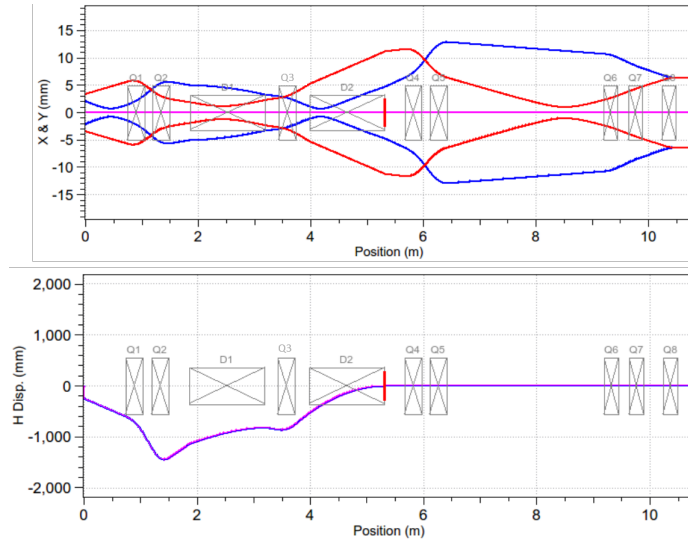

Figure 3.7: Above, radial (blue line) and axial (red line) beam envelopes along the beam transport line for the ion ^{20}Ne fully stripped at the energy of 71 AMeV. Below, horizontal dispersion vs. beam transport line length for the same ion of the above figure.
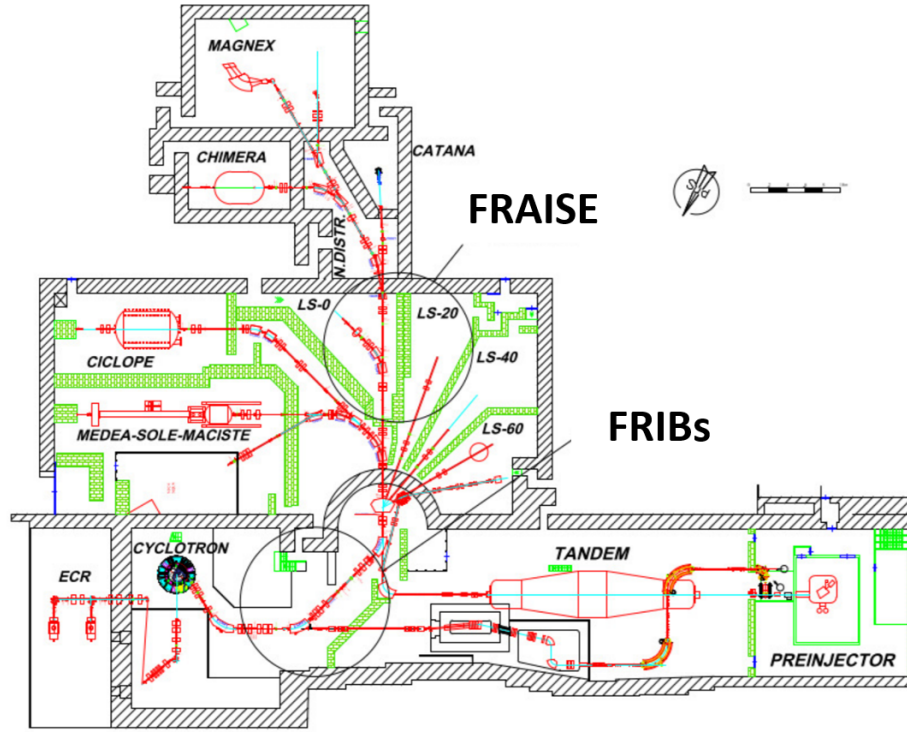
Figure 3.8: Schematic view of the INFN-LNS beam lines and experimental halls. The position of the existing fragment separator, FRIBs, and of the new one, FRAISE, are indicated by circles [3].

FRAISE is able to accept ion beams with a maximum magnetic rigidity of 3.2 T·m. The momentum and the solid angle acceptance are $\pm 1.2\%$ and 2.5 msr respectively and the energy resolution $\Delta E/E$ is equal to 1/2600 with a beam spot size of ± 1 mm.

On the symmetry-dispersive plane, a mechanical slits system for the control of beam profile and a degrader for performing a better rejection of the undesired ions will be placed. In addition, it is planned to place another mechanical slits system at the exit of the fragment separator for a further selection/control of the beam profile.

FRAISE, with its high energy dispersion feature at the symmetry-dispersive plane, can be also used as an energy selector. This feature allows to limit the energy spread of the ion beams extracted by stripping to $\pm 0.1\%$ FWHM in order to satisfy the NUMEN requirements on the beam en-
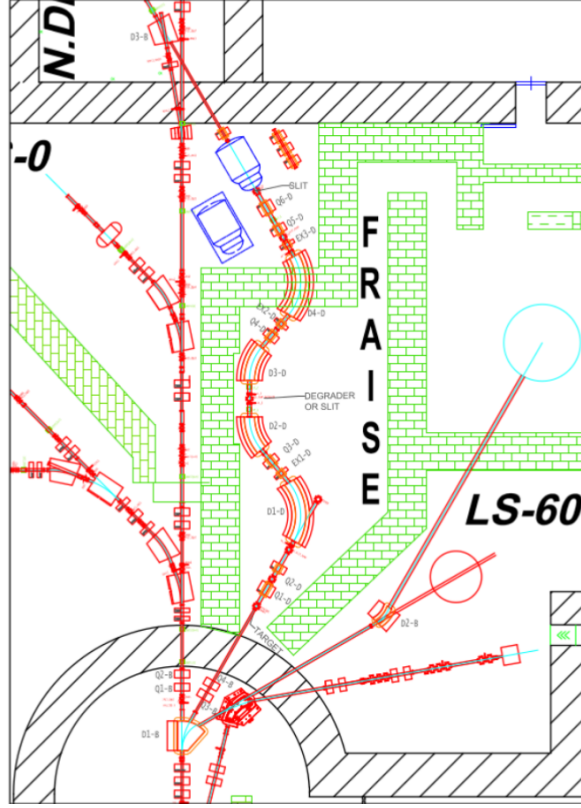
Figure 3.9: Preliminary design of FRAISE in the new dedicated area indicated by a circle in Fig. 3.8.

ergy. However, only 2 kW beam power could be stopped by FRAISE due to radiation limit imposed by the wall shielding.

3.6 Improvement of the ion sources and injection line

The improvement of the ion beam production and of the beam transport from the ion sources into the LNS cyclotron is an aspect that can not be neglected within the upgrade project of the CS because the quality of the accelerated ion beams also depends both on the beam features at the ion source extraction and at the end of the axial injection line before the acceleration in the cyclotron.

In order to increase the produced beam current of heavy ions, possible solutions are under study at LNS laboratories, first of all the improvement of the SERSE ion source.

An upgrade of the SERSE plasma chamber in order to operate at higher extraction voltages than the present ones (20-25 kV), up to a value of 35 kV, could be important for the following reasons: (i) high currents of highly charged heavy ions could be obtained because the extracted beam current (in space charge limited regime) increases as $V^{3/2}$, (ii) beam losses in the low energy beam transport could be reduced, (iii) improvement of the matching to the acceptance of the CS could be achieved.

The possible upgrade of the SERSE ion source has been studied from the mechanical point of view but a complete thermomechanical analysis has to be carried out. Moreover, the CAESAR ion source could be replaced with the more performing ion source, named AISHa (Advanced Ions Source for Hadrontherapy) [75].

The new ion source, that is actually under commissioning at LNS laboratories, would operate in synergy with the SERSE ion source.

AISHa is a hybrid ECRIS: the radial confining field is obtained by means of a permanent magnet sextupole, while the axial field is obtained with a Helium-free superconducting system.

It was designed taking into account the requirements of the CNAO (Centro Nazionale di Adroterapia Oncologica) hospital facility, where a synchrotron accelerator is used to deliver carbon and proton beams.

In particular, AISHa is optimised to provide highly charged ion beams with low ripple, high stability and high reproducibility. Although AISHa is an ion source for specific uses in adrotherapy facilities, it could be easily adapted for nuclear physics demands.

Another aspect within the CS upgrade project is the improvement of the beam transport efficiency and the minimization of the present beam losses along the existing CS injection line. It is important for the injection line

to match exactly the beam phase space with the cyclotron acceptance. The injection line of the CS is not currently equipped with devices devoted to measure accurately the beam phase space and features along the line, as for example beam emittance measurement devices and beam monitors. Therefore, an improvement of the beam diagnostics along the CS injection line is necessary in order to monitor constantly the beam and to individuate possible mismatch sources as for example misalignments of the elements that constitute the beam line.

3.7   Spiral inflector and central region study

As described in section 3.1, the expected efficiency of the stripping extraction for the light-medium ion beams required by the CS upgrade project is about 100%, almost a factor two higher than the current efficiency of the extraction by electrostatic deflectors. The increase of the extraction efficiency is not sufficient to obtain beam power up to 10 kW. Indeed, also a high injection efficiency of about 15% is required to obtain the beam power values reported in Table 1.1, assuming no losses along the injection line from the ion source into the LNS cyclotron and a bunching efficiency equal to three.
Presently, the injection efficiency is smaller of about a factor three, including the buncher effects. Therefore, the study of the spiral inflector and central region plays an important role within the project of the INFN-LNS Superconducting Cyclotron in the same way of the study of the stripping extraction, being both finalized to the improvement of the overall efficiency. This is part of this thesis work and the results of the carried out study are reported in Chapter 6. The study has been performed using the IBA orbit code, named as AOC, in the frame of a collaboration with the IBA (Ion Beam Application) company.
The evaluation of the overall efficiency, that includes the processes of beam injection, acceleration and extraction by stripping from the CS, is

constrained by the NUMEN requirement on the beam energy spread.

The expected energy spread of the NUMEN beams extracted by stripping is about $\pm 0.3\%$ FWHM, as reported in Chapter 4, a factor three times higher than the NUMEN requirement. In order to reduce the beam energy spread, the new fragment separator will be used as energy selector. Therefore, the overall efficiency has to take into account also the process of energy selection outside the LNS cyclotron. However, only 2 kW beam power can be stopped by FRAISE due to radiation limit imposed by the wall shielding. This means that the energy spread of the extracted beam should be as low as possible.

In case of stripping extraction, the extracted beam energy spread depends on the energy gain per turn and on the radial beam size (more detail is present in the dedicated chapter on the stripping extraction from the CS). Hence, for achieving a small final energy spread of the beam, it is important to have a good accelerated beam quality. Indeed, in presence of off-centring, coherent oscillations of the beam centre occur and after many turns, they smear out and directly lead to increase of the circulating beam emittances and, consequently, of the beam sizes. This aspect is amplified in the LNS cyclotron due to the large emittance injected into the CS, that poses a limit on the minimum extracted beam energy spread can be achieved.

For a given energy spread requirement, the overall efficiency is individuated by the losses in the spiral inflector and central region, the losses in the extraction system and energy selection system.

The central region has to allow a good horizontal and vertical beam dynamics but, at the same time, to maximize the ion transmission and consequently the injection efficiency. Ion losses in the central region are expected because the cyclotron is a RF accelerator that is not able to accelerate the full DC beam coming out from the ion source and the central region geometry plays an important role in individuate the RF

phase acceptance of the accelerator. Radial losses are concentrated near the structure elements like the pillars. Also vertical losses on the accelerating electrodes can occur if the beam is not well vertically focused in the cyclotron centre. Therefore, simulation of ion tracking from the axial bore entrance, through the existing spiral inflector and central region up to the stripping extraction, including the energy selection system, are essential for understanding how the injection efficiency can be increased, looking, at the same time, at the ion transmission from the central region and the beam energy spread at the extraction.

Chapter 4

Study of extraction by stripping from the CS

4.1 Introduction

The extraction of beam power up to 10 kW from the INFN-LNS Superconducting Cyclotron is not feasible using the existing extraction system, composed of two electrostatic deflectors, for the reasons already explained in the previous chapter.

It is planned to extract by stripping the light-medium ion beams with energy of interest for the NUMEN experiment and RIBs production since an extraction efficiency also close to 100% is expected (see Table 3.1).

The advantages of stripping extraction compared to extraction by electrostatic deflector is the absence of the turn separation requirement.

Moreover, usually the stripping extraction is easier to manufacture and operate since only a thin carbon foil is used and no electric fields are involved as in the case of extraction by electrostatic deflector.

However, the extraction trajectory and dynamics of an ion beam after stripping are highly dependent on the ion energy and specific charge. Therefore, when a multi-particle variable energy such as the CS is concerned, it is not so easy to deliver a variety of ion beams into the same high energy transport line and, at the same time, preserve a reasonable

compactness of the extraction system.

In the case of the LNS cyclotron, the situation is complicated by the constraint on the coexistence of the new extraction system with the existing one since the CS has to continue to deliver to the LNS users the present ion beams extracted by electrostatic deflectors.

Investigation on the feasibility of the stripping extraction from the CS has been done in past years [69] and the study highlighted that a new extraction channel is needed to facilitate the exit of all the ion beams to be extracted by stripping, as already explained in Chapter 3.

The study of extraction by stripping accomplished in this thesis work has allowed to individuate the features of the new extraction system necessary to guide the NUMEN ion beams from the accelerated orbits inside the CS to a common position outside the cyclotron.

The goals of this study were to individuate: i) the stripper foil position for each ion to be extracted by stripping, ii) the transverse dimension and direction of the new extraction channel in the CS to be used for all the ions to be extracted by stripping and iii) the features of the magnetic channels to be installed inside the new extraction channel.

Hereinafter, a description of the method used in the study to calculate the extraction trajectory and dynamics of the ion beams after stripping and the results of the simulations are presented.

4.2   Method description

During interaction of a positive ion with a thin carbon foil, some ion electrons are stripped and the ion increases its charge. Due to the presence of magnetic field, the change of the ion charge state caused by the stripping process results in the change of the ion orbit. In particular, a positive ion decreases its orbit radius after the stripping process, according to Eq. 3.1.2. Therefore, it makes at least one loop before exiting the cyclotron, as already shown in Fig. 3.1.

However, the extraction of a beam that makes more than one loop after the foil crossing should be avoided. This effect is used for extracting ion beams by stripping from a cyclotron. Since the magnetic field of a cyclotron is not uniform, the ion behaviour after its interaction with the stripper foil depends on the foil position in the cyclotron. Radial movement of the stripper foil allows to change the energy of the extracted ion beam.

Usually, the charge of a positive ion beam after its interaction with the stripper foil is not unique and the distribution of the ion charge after the stripping process depends on ion energy and atomic mass. In our case, we expect that the accelerated ^{12}C, ^{18}O and ^{20}Ne partial stripped ions extracted at the energy of interest for NUMEN are fully stripped after the stripping process. Indeed, the probability that the ions are not fully stripped are only of the order of 10^{-4}-10^{-7} (see Table 3.1).

Usually, a stripping foil extraction system consists of: i) one or more carbon foils, ii) a mechanism for holding, positioning, and exchange of the foils, iii) an exit channel that has to be machined in the cyclotron and iiii) guiding elements used to focus and bend the beam after it interacts with the stripper foil and before it enters a high energy transport line. The guiding elements can be passive magnetic channels placed inside the vacuum chamber or active magnetic elements located outside. In our case, only passive magnetic channels will be used and placed inside the new exit channel. The passive magnetic channels will allow to prevent that the beam diverges too much due to the magnetic fringing field action inside the new exit channel. Moreover, it has been planned to use them also as steering magnets to adjust the direction of the beam inside the extraction channel. Obviously, this requires an appropriate handling systems of the magnetic channels to change their position according to the ion to be extracted by stripping.

The extraction system has to provide extraction not of a single ion beam,

but of the group of accelerated light-medium ion beams of interest for the NUMEN research project and RIBs production. The design parameters of the stripping extraction system are the coordinates of the stripper foil position (angular and radial position) and the parameters of the passive magnetic channels (position, size, maximum focusing requirements), once individuated and set the direction of the extraction channel.

The study of the stripping extraction from the CS has been carried out by simulation of beam dynamics with the aid of two software, named GENSPE and ESTRAZ, originally developed at the MSU by Prof. Gordon and modified over time to meet local needs at LNS.

These software solve the three coupled, non-linear partial differential equations that describe a charged particle motion in a magnetic field using the fourth-order Runge-Kutta method. The two codes are used to simulate the process of extraction by stripping. It is assumed that the stripper foil is positioned along the equilibrium orbit of the ion to be extracted, defined by its mean radius. The GENSPE software allows to determine the ion parameters along the equilibrium orbit. The input parameters required by GENSPE are: i) the type of ion (mass and charge state), the magnetic field map on the median plane in a sector of the cyclotron, the normalized emittance of the beam. A value equal to 1π mm-mrad has been assumed for all the ions considered in the study.

The isochronized magnetic field of the ion is calculated taking into account the measured magnetic field map $B(r,\theta)$ of the LNS cyclotron, stored in a polar mesh with $\Delta\theta = 1°$ and $\Delta r = 1$ cm. Values of the magnetic fields outside the median plane are determined using Taylor's expansion, as well as numerical derivation of the median plane magnetic field.

GENSPE gives in output detail on each closed orbits with a step of energy chosen by the user. For each ion beam and chosen energy and position on the equilibrium orbit, coincident with that one of the stripper foil, the

GENSPE code allows to evaluate the initial properties of the beam centroid and of eight particles that describe the beam eigen-ellipse in the (x, x') and (y, y') phase spaces at the stripper position. The code ESTRAZ is used to simulate the stripping process assuming the initial conditions of the particles at the stripper foil evaluated by means of GENSPE to calculate the extraction trajectory of the beam centroid and the radial and axial beam envelopes along the extraction trajectory. ESTRAZ starts to integrate the orbit from the point (R, θ) on the equilibrium orbit, where the stripper is assumed to be placed, up to the exit of the CS, outside the yoke. For a better understanding of the simulation results, the beam centroid trajectory calculated by ESTRAZ can be imported in AUTOCAD for its visualization in the median plane design of the LNS cyclotron.

The ESTRAZ code allows also to simulate the action of passive magnetic channels on the ion beams both in terms of radial focusing gradient and field steering magnet.

4.3   Simulation results

The study of stripping extraction has been constrained by requirements related to the full cyclotron design: i) the orbits have to pass at least 70 mm away from the CS centre to avoid any interference with the central region components, ii) the axial beam envelopes have to be lower than ± 15 mm inside the pole and ± 25 mm along the new extraction channel.

Moreover, in order to facilitate the connection between the new extraction channel and new extraction beam line, we set a common exit point from the CS. This point has been also chosen taking into account that the new extraction channel has to be as short as possible, as already explained in detail in Chapter 3. The common exit point corresponds to the angular position $126°$ at the radius of 2000 mm. From now on,

the angles are referred to a clockwise polar coordinate system, i.e. we consider that the polar angle θ increases for rotations in clockwise orientation [51].

In the simulation study we considered a beam energy spread equal to $\pm 0.3\%$ for all the ion beams with different energies to be extracted by stripping. The energy spread at the extraction depends on the ion and energy, however it always remains in the neighbourhood of 0.3% for all the cases, according to analytical calculations [76]. The energy spread of the beam at the extraction can be explained considering that, when a beam is extracted by stripping, more turns occur before that all the particles are extracted, as described in Chapter 6.

Since the orbits of ions with different masses, charge states and energy differ each other after the stripping process, the determination of a common exit direction of the orbits for all the ions to be extracted by stripping and passing through the chosen common exit point has not been trivial. In fact, to identify for any ion and for any energy the radial and angular position of the stripper, satisfying all the limits previously described, it was necessary to carry out from 4 to 7 attempts for each case, changing time to time the angular position and/or the radial position of the stripper foil.

For each considered ion, the best azimuthal position of the stripper foil has been found in order that the extraction orbit pass as close as possible to the common exit point. We were able to size down the region where to place the stripper foils in two main areas for all ions of interest, one on the hill, $106° < \theta_{stripper} < 122°$, (just where the electrostatic deflector ED1 is placed) and the other one on the valley, $60° < \theta_{stripper} < 88°$, just before the ED1. Figure 4.1 shows a zoom of the positioning area of the stripper foils. The red and blue colours refer to the stripper positions on valley and on hill respectively. The operating area of the mechanism for stripper foil positioning and exchange cover as many as possible foil posi-
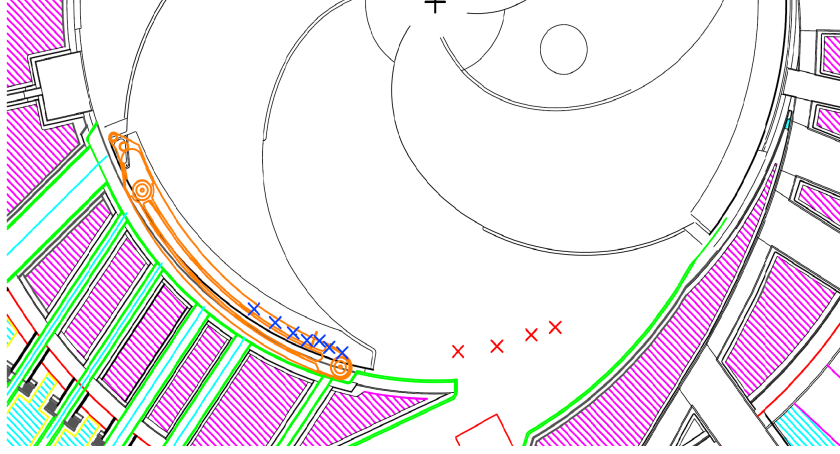
Figure 4.1: A zoom of the positioning area of the strippers foils. The red and blue colours refer to the stripper positions in valley and in hill, respectively.

tions corresponding to the desired ion beams. The design of the stripper foil handling system is complicated by geometric limitations inside and outside the CS due to the presence of the existing extraction system that can not be removed definitively. As already reported in previous chapter, the LNS engineering staff is working to find mechanical solutions that allow to perform the extraction by stripping, however maintaining the existing extraction system.

As one can see in Fig. 4.1, the handling system of the stripper foils placed on the hill interferes mechanically with the first electrostatic deflector. As already explained in Chapter 3, it has been planned to extract by stripping intense ion beams approximately six months per year and, for the remaining time, the LNS cyclotron will deliver ion beams to the LNS users using the two electrostatic deflectors.

Table 4.1 contains the list of the ion to be extracted by stripping with the relative energy at the extraction. For each ion, the angular and radial position of the stripper foil is reported. As one can see, for the 29.2 MeV/amu $^{18}O^{6+}$ and 45.5 MeV/amu $^{18}O^{6+}$, two possible positions of the stripper foil have been found, one on the hill and the other one on the valley. Radial and vertical beam envelopes have been computed for each

case study. As an example, Fig. 4.2 shows the radial and axial beam envelopes of ^{18}O at energy 65 MeV/amu computed with the ESTRAZ code. The radial envelopes obtained by simulations performed with and without beam energy spread is also shown. As one can see in the figure, the energy spread affects the radial beam envelope leading to its increment. Figure 4.3 shows the new median plane of the INFN-LNS Superconducting Cyclotron after the modifications required by its upgrade. A description of the modifications to be applied to the CS median plane has already given in the previous chapter. The two extraction channels, the existing one and the new one, are visible in the figure. As one can see, the transversal dimension of the new extraction channel is larger than the new one. In the figure, also the extraction orbits relative to all the studied case are present. The red orbits have been obtained simulating the extraction by stripping with the stripper foil placed in the valley, the other ones in the event that the stripper foil is placed on the hill where the first electrostatic deflector is currently mounted.

One of the most relevant results of this study was that only two passive magnetic channels, named MC1S and MC2S, placed in the new extrac-
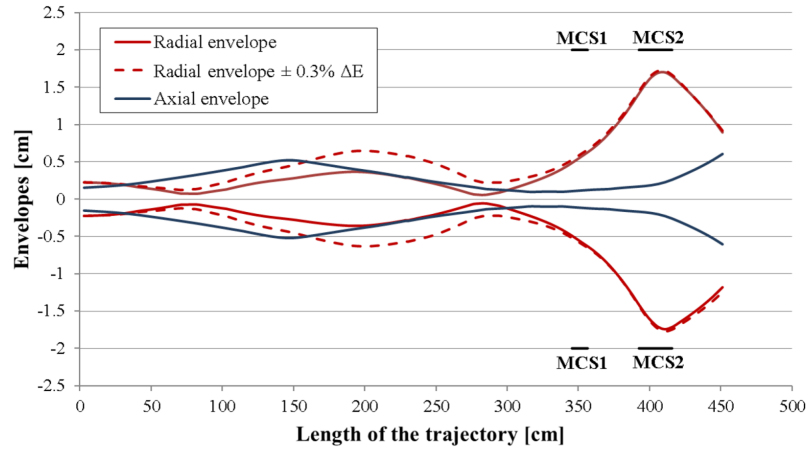

Figure 4.2: Radial and axial envelopes for the ion beam ^{18}O at stripping energy equal to 65 MeV/amu along the stripping trajectory. The effect of an energy spread $\pm 0.3\%$ is also shown.

93

Ion	$\frac{Q_{acc}}{Q_{ext}}$	Energy (Mev/amu)	$\theta_{stripper}$	$R_{stripper}$
^{12}C	4/6	45.8	112	88.2
		60.8	106	87.9
^{18}O	6/8	29.2	60	84.2
		29.2	118	87.7
		45.5	68	84.7
		45.5	110	87.1
		60	80	84.6
		60.9	106	88
		65	88	84.9
^{20}Ne	7/10	29	122	87.7
		45.6	114	87.9
		60.3	108	87
		71	108	87.9

Table 4.1: List of the ions to be extracted by stripping and specification of the stripper position.

tion channel, are sufficient to permit the extraction of the beams of all ions of interest with different charge states and energies. The gradient for both magnetic channels is 1.8 kG/cm. This result reduces considerably the complexity of the stripping extraction system since it will not necessary to open the CS when the ion to be extracted by stripping changes. The passive magnetic channels will also be used as steering magnets for adjusting the direction of the extracted orbits inside the new extraction channel in order that each ion passes close as possible to the chosen exit point from the CS. According to the simulation results, the steering action of each magnetic channel must be different for each ion. This means that the reference trajectory has to enter the magnetic channels in a different point. In order to do this, a handling system for each magnetic channel will be necessary to adjust their positions according to the ion to be extracted by stripping. The study of this system is already ongoing at LNS laboratories.
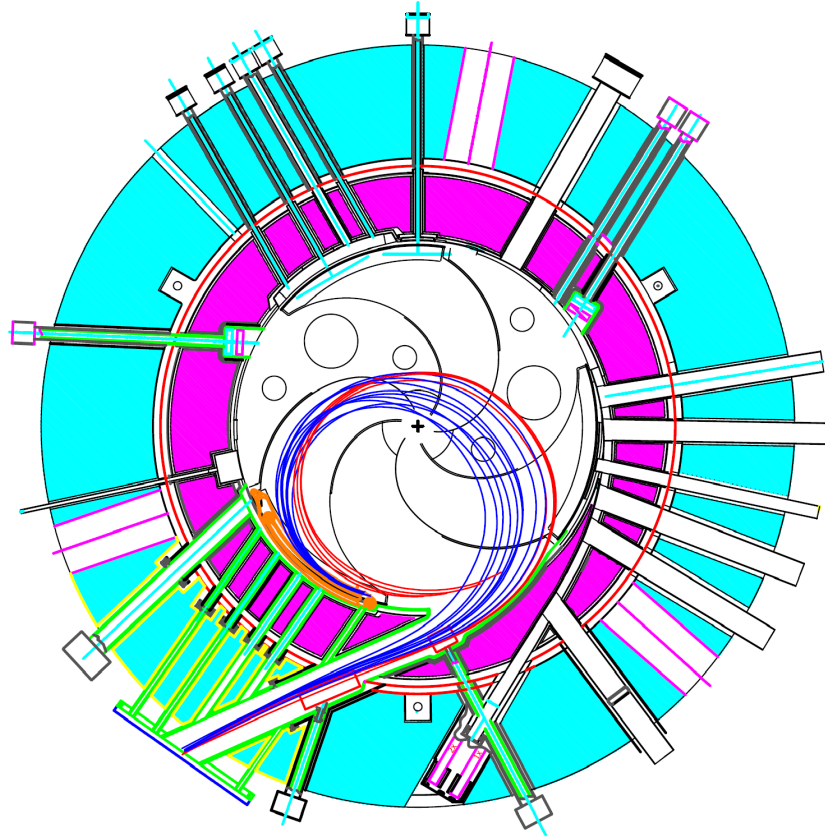
Figure 4.3: the CS median plane with the new extraction channel and the stripping trajectories of all the studied cases.

Chapter 5

Dalevelopment of the accelerating and magnetic structure models of the CS

Computations of particle orbits in a cyclotron require the creation of models of the magnetic and accelerating structures for magnetic and electric field calculation.

The INFN-LNS Superconducting Cyclotron was designed more than thirty years ago, when advanced three-dimensional (3D) programs for electromagnetic modelling were not yet available.

Its central region was designed at the end of 1990s using RELAX3D [77], a program developed at TRIUMF by H. Houtman and C.J. Kost, to solve the Poisson or Laplace equation $\nabla^2 \phi = \rho$ for a general 3D geometry using the successive over-relaxation method.

Modern design tools available today, enable to evaluate with great accuracy 3D magnetic and electric fields.

This thesis work includes the development of the model of the existing accelerating structure of the CS, including also the spiral inflector, in order to evaluate the electric field map needed to perform studies of beam dynamics from the axial injection into the LNS cyclotron up to the extraction. The purpose of these studies has already been explained in

Chapter 3 and more details are presented in Chapter 6.

The Opera-3d software package from Dassault Systèmes [78] has been used for this purpose. It is a commercial software based on the Finite Element Method (FEM), a numerical technique for obtaining approximate solutions of problems for general 3D geometry described by partial differential equations which can not be analytically solved, as in the case of the electromagnetic potential.

In this chapter, the 3D modelling approach developed in this thesis for designing the accelerating structure of the LNS cyclotron and the main model features are presented.

The same software has been used at INFN-LNS for creating the model of the existing CS magnetic structure, that has been utilized in this thesis work for evaluating the magnetic field map to be used for the beam dynamic studies above-mentioned. Even if the development of the magnetic model of the LNS cyclotron is not part of this thesis work, its main features are reported in this chapter in the interests of providing fuller information.

5.1   3D modelling approach

The accelerating structure of the INFN-LNS Superconducting Cyclotron has been simulated in Opera-3d using the modelling approach developed at IBA, consisting in the fully parametrization of the model and its generation using macro [79].

Examples of properties that are parametrized in the modelling macro are:

- all important dimensional parameters;

- sizes and other properties of the finite-element mesh;

- properties of the boundary conditions;

- solver tolerance.

This design approach allows the fast modification and optimization of the design, i.e. parameters values can be easily changed and consequently the corresponding new model is quickly obtained.

Using this design technique, modifications to the present design of the CS accelerating structure have been easily performed allowing a strong reduction of the modelling time. Details about these modifications are presented in Chapter 6 with the related simulation results.

The main structure of the macro for the 3D modelling of the CS accelerating structure is shown in Fig. 5.1. The blocks in pink show the principal steps: (i) creation of the model in the Opera-3d Modeller, (ii) solution of the model using the Opera-3d solver, (iii) post-processing analysis of the simulation results.

The blocks in light orange illustrate the steps needed to create the model in the Opera-3d Modeller: after the reading all parameters from a file, individual subsystems are created, later they are assembled into a model representing the full system and finally a database is created, saved and
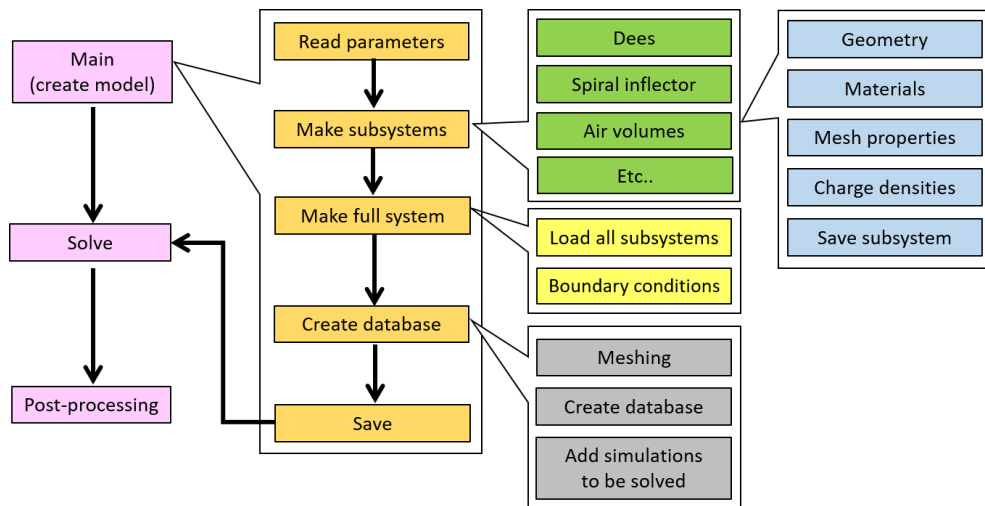

Figure 5.1: Logical structure of the macro used for the fully parametrized and automatized creation of the Opera-3d model of the CS accelerating structure.

used as input for the solver. Each subsystem is an element of the CS accelerating structure or an air volume. In Fig. 5.1 only few elements are listed in the green blocks for simplicity.

The light blue blocks show some details about the operations for designing each subsystem: geometry modelling, material properties definition, charge density and mesh properties assignment. Details about the geometry modelling are presented in the next section.

A small charge density is allocated to all the electrodes of the CS accelerating structure. This charge density is so small that it does not change the electric fields. In the AOC code [80], used in this thesis for the ion tracking in the LNS cyclotron, the charge density serves as indicator for electrode hits, as described in Chapter 6. Moreover, the same material label, named as copper, is assigned to all the electrodes.

Once a subsystem is designed, it is saved in a file. The full system is generated loading all the subsystems and assigning the boundary conditions required by the physical problem to be solved (blocks in yellow in Fig. 5.1). For the matter in question, the boundary conditions consist in the assignment of a scalar potential to the surfaces of the electrodes, in particular zero for the grounded electrodes and one for the other ones.

Indications about the operations needed for the database creation are reported in the grey blocks in Fig. 5.1.

First, the creation of the database requires the meshing process (surface and volume mesh), i.e. the discretization of the geometry in small domains by means of a set of points, the so-called nodes.

This step plays a decisive role in the simulations, establishing the accuracy and quality of the fields calculated at the end of the processing phase. The mesh size can be locally adapted to the details of the geometry. As an example, only a good surface mesh is needed in the case of an electrode because, as it is well known, the electric field inside it is zero. Air volumes allow to control the maximum mesh size in the region

crossed by the ion beam.

Whenever possible, it is always worth diminishing the number of nodes in the 3D model, which consequently reduces also the time of calculations but also the disk storage. This can be done by the application of all possible symmetries (rotational and/or with respect to one or more planes) to the system. Unfortunately the full model is always necessary when one or more elements that compose the system are asymmetrical, as in the case of the accelerating structure model of the CS.

The accelerating electrodes are symmetrical with respect to the median plane and, excluding the central region, they also have a three-fold rotational symmetry. The presence of the spiral inflector in the CS centre forces to create a full model without any type of symmetry because the spiral inflector is a asymmetric device.

For creating the analysis database, information for the type of analysis program to be used to solve the field equations are given.

Opera-3d has a wide variety of solver types for solving various physical problems. TOSCA solver is used to calculate the electric field created by the accelerating structure of the CS in static approximation, and the electrostatic field generated by the spiral inflector. In general, a static solver can be used if the size of the structure is small compared to the wavelength of the RF. Otherwise, a real RF-solver (CST or Soprano) is needed.

A linear analysis of the physical problem is set, i.e. material properties are assumed constant. Consequently, the Maxwell equations describing the physical problem are linear and the principle of superposition of the solutions can be applied. This implies that the total electric field to be used in the beam tracking model for computation of beam dynamics can be written as the linear superposition of field maps produced by all the separate electrodes existing in the cyclotron (each one driven by a separate boundary condition).

The creation of the database enables the inclusion of different cases to be solved in cascade. In the case of the CS accelerating structure model, the total number of simulations to be solved is equal to five, of which one for each not-grounded electrode that constitutes the accelerating structure and two for the spiral inflector.

The electric fields generated by the three dees are calculated separately because the three RF cavities do not work in phase but they oscillate $\pm 120°$ out phase with respect to each other, being the LNS cyclotron a three-fold symmetry cyclotron working in $h = 2$ harmonic mode.

At the end of the solving process, all the solutions are saved in a single analysis database. For each solution, an eletric field map is extracted and saved in a file to become part of the electric field input map for the AOC orbit code. Electric field output maps can easily be adapted to the requirements for orbit integration, providing as input to Opera-3d Post-Processor the set of points where the fields have to be evaluated and written. The main features of the 3D electric field map required by the AOC orbit code are described in Chapter 6 in the section dedicated to the development of the beam tracking model.

The Opera-3d Post-Processor can be used to process and display the calculated results by the TOSCA solver.

It can be also used to display the trajectories calculated by the AOC orbit code in a colourful way. For this purpose, IBA has developed a dedicated tool for converting the AOC trajectory output file in the format used by the Opera-3d Post-Processor.

5.2   Main features of the accelerating structure model

The Opera-3d model of the existing CS accelerating structure has been created starting from the 3D engineering drawing of all the present

electrodes saved in a CAD (Computer Aided Design) format file.

Opera-3d can import and read CAD files and, in almost all cases, complex geometries read from these files may need modification and simplifications before performing the meshing process, as in the case of the CS accelerating structure.

All the electrodes, excluding the spiral inflector, have been designed from scratch in the Opera-3d Modeller using the macro described in the previous section. The "wire-edge" and "sweep" Opera-3d operations have been sequentially applied to create the bi-dimensional (2D) profile of each body of the system, using the coordinates of the contourn points extracted from the CAD file. Once created a body profile on a 2D plane as a union of straight or curved wire-edges connected by points, it has been extended in the third dimension to create the body volume in the 3D space. When needed, complex geometries have been created merging, intersecting or subtracting many objects in the 3D space.

Detailed geometrical features, playing a negligible effect on the simulation results, have been not included in the simulations. As example, the engineering drawing of one of the dees and the simplified geometry of the same electrode, created using the Opera-3d Modeller, are presented in Fig. 5.2 on the left and on the right respectively.

All the details of the existing geometry not highly influencing the beam dynamics in the cyclotron, as for example the RF cavity hole and the cooling grooves in the dees case, have been neglected during the modelling phase in order to facilitate the meshing process. Also the blends have not been included because their presence does not affect significantly the simulation results.

Figure 5.3 on the left shows the existing accelerating structure of the CS designed using the Opera-3d Modeller. In the figure, only the electrodes below the median plane are shown for a better visualization. Different colours are used to distinguish the elements: the dees are in pink and
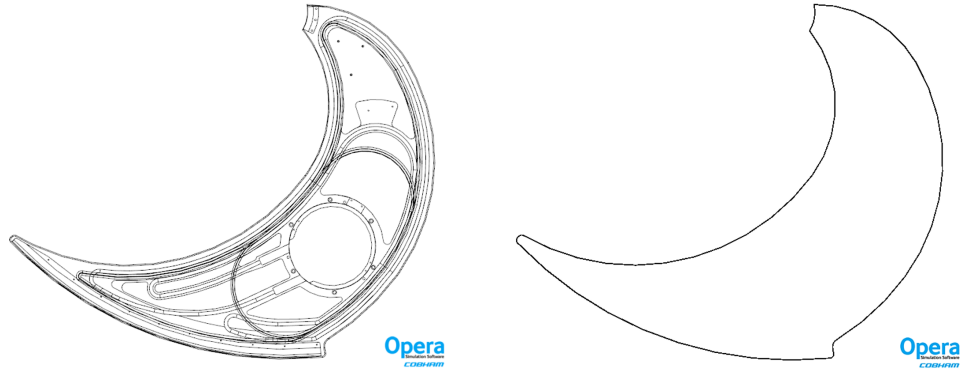
Figure 5.2: On the left, engineering drawing of one of the dees of the LNS cyclotron. On the right, simplified geometry of the same electrode, created using the Opera-3d Modeller.
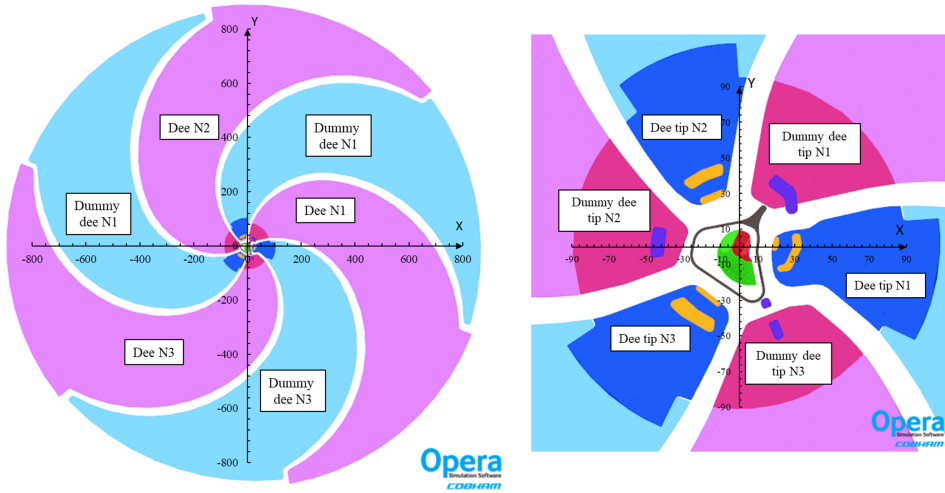
Figure 5.3: On the left, the Opera-3d model of the existing accelerating structure of the LNS cyclotron. On the right, the drawing of the existing electrodes of the CS central region together with the spiral inflector and the housing surrounding it. All the dimensions are in mm.

their tips in magenta, the grounded electrodes are in light blue and their tips in blue. The drawing of the existing CS central region is present in Fig. 5.3 on the right. The collimator, that has the same 2D profile of the housing and is placed before the spiral inflector entrance, is not shown in the figure for a better visualization of the housing and spiral inflector. The orange pillars are at the same potential of the dee tips, the other

ones are grounded electrodes.

Different maximum mesh sizes have been defined for the air volumes crossed by the beam. A small size has been chosen along the principal vertical axis, in the cyclotron centre and very close to the median plane of the LNS cyclotron, while a larger value has been set far away from the CS centre. It is very important to use a fine mesh size in the cyclotron centre in order to estimate accurately the electric field generated by the accelerating structure in this region. Indeed, due to the flutter that goes quickly to zero in the cyclotron centre, the vertical focusing in the first turns is provided by the electric field generated by the accelerating structure, in particular by the first few accelerating gaps.

After few turns, when the energy of the particles is increased sufficiently, the magnetic focusing starts to become important and the electric focusing rapidly falls. In the region where this happens, the use of a very fine mesh size becomes less mandatory.

Using the Opera-3d Post-Processor, simulation results have been extracted in a useful mode, for example by the display of variable values in graphs, charts or tables. Hereinafter, some cases are reported.

Fig. 5.4 shows the azimuthal and vertical components of the electric field in the accelerating gap between the dummy dee N1 and dee N2, according to Fig. 5.3. The plots have been obtained considering two circular arcs with radius equal to 120 mm and 500 mm with respect to the CS centre respectively. The azimuthal component of the electric field E_t is given in the median plane (z = 0 mm) while the electric field z-component E_z is given for different values of the vertical coordinate z (z = 3, 6, 9, 12 mm). The plots show that the vertical component of the electric field does not vary linearly increasing the distance from the median plane. This is one of the reasons why it is important the use of tools for evaluating 3D electric field maps for beam dynamics studies in cyclotrons.

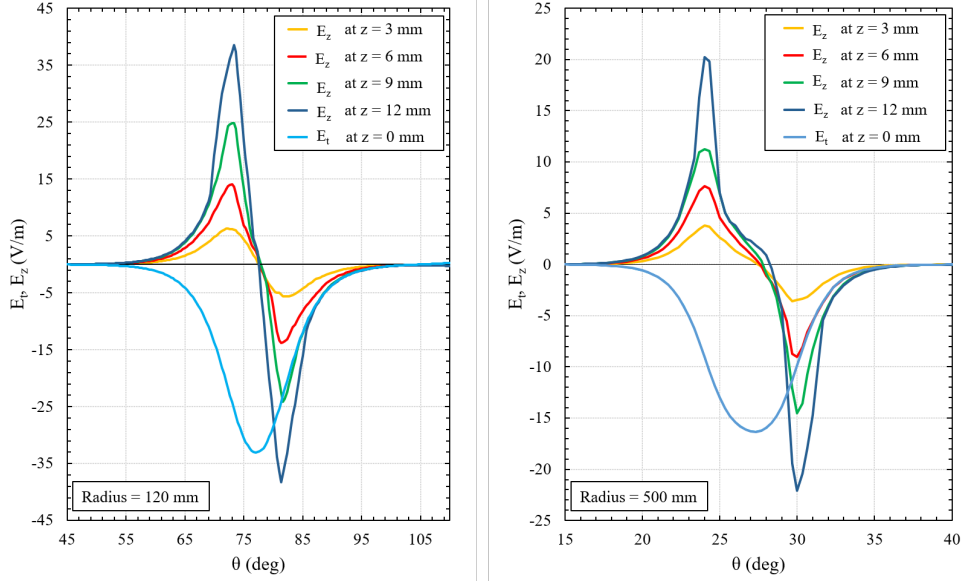The lack of noise (smoothness) in the calculated field in Fig. 5.4 on the

Figure 5.4: Azimuthal E_t and vertical E_z components of the electric field in the accelerating gap between the dee N2 and dummy dee N1. They have been evaluated considering two circular arcs of 120 and 500 mm radius respectively. The angle $\theta = 0°$ coincides with the x-axis direction. E_t is given in the median plane, E_z is given at z= 3, 6, 9, 12 mm.

left indicates a good quality of the chosen mesh size in the central region. The same is valid also for the other plot.

With Opera-3d it is also possible to plot the equipotential lines in a plane specified by the user. As example, the equipotential lines in the median plane in the central region are shown in Fig. 5.5. Orbits accelerated by the LNS cyclotron are also shown. The figure is referred to the case when all the dees are excited at the same voltage simultaneously and does not correspond with the $h = 2$ harmonic mode case.

In order to obtain this figure, the Opera-3d model of the CS accelerating structure has been solved assigning at the same time the same scalar potential to the surfaces of all the dees.

The figure shows that the equipotential lines are not very concentrated in the accelerating gaps and ions do not cross the equipotential lines in the first gap perpendicularly.
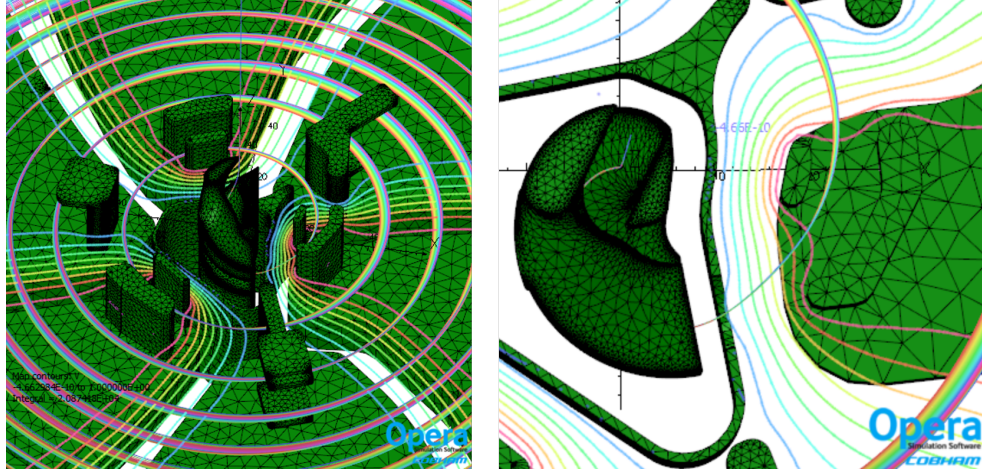
Figure 5.5: Equipotential lines in the median plane in the CS central region.
The figure is referred to the case when all dees are excited at the same
voltage simultaneously. The lines are evaluated with step equal to 10%
of the maximum value. Orbits accelerated by the LNS cyclotron are also
shown.

The spiral inflector has not been designed from scratch but the simplified
CAD geometry has been included in the CS accelerating structure model.
Indeed, due to the complex shape of the electrodes, it is not possible to
design the spiral inflector using the same technique applied for the accel-
erating electrodes of the LNS cyclotron.

Figure 5.6 shows the Opera-3d model of the CS spiral inflector in the
central region.

As reported in Chapter 2, the spiral inflector is surrounded by the so-
called housing. In the figure, only the portion of the housing below the
median plane is shown for a better visualization of the spiral inflector.

The whole housing is shown in Fig 5.7. Also the collimator is present in
the same figure. It is placed at 20 mm from the housing entrance and at
about 44 mm from the spiral inflector electrodes.

Figure 5.8 shows the equipotential lines and the electric field vectors at
the inflector entrance on the vertical plane x-z. The figure shows that the
electric field is present, not only in the region between the two electrodes,
but it extends also in the region before the entrance gap, decreasing in in-
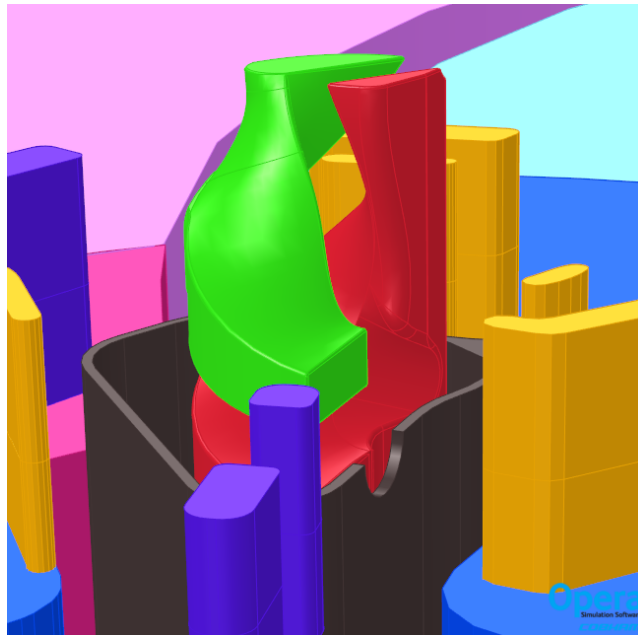
Figure 5.6: Opera-3d model of the CS spiral inflector in the central region. Only the portion of the housing below the median plane is shown for a better visualization of the spiral inflector.
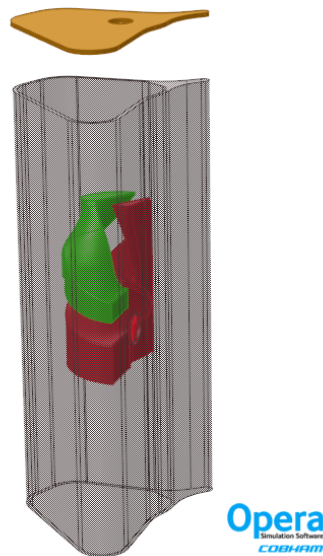

Figure 5.7: Collimator and housing of the CS spiral inflector. The collimator is placed at about 44 mm from the spiral inflector electrodes and at 20 mm from the housing entrance.

Figure 5.8: Equipotential lines and the electric field vectors at the inflector entrance on the vertical plane x-z. The electrical potential lines are evaluated with step equal to 10% of the maximum value.

tensity, when increasing the distance above the spiral inflector electrodes. As described in Chapter 6, the electric fringe fields at the inflector entrance and exit influence the motion of a particle that enters the spiral inflector moving along the cyclotron vertical axis. Consequently, it is essential to take into account the electric fringe fields in the design of a spiral inflector. Only if a reasonable model of the electric fringe fields is used, the particle orbit in the inflector will slightly differ from the ideal design orbit of the device and the small deviations can be corrected by slight adjustments of the voltage on the inflector electrodes. In the case of the existing design of the LNS spiral inflector, it is sufficient to adjust the spiral inflector voltage in order to optimize the beam centroid motion without the need to redisegn from scratch the spiral inflector, as reported in the next chapter.

5.3 Main features of the CS magnetic model

Tracking particles in a spiral inflector requires 3D magnetic field data in the whole injection volume. Therefore, the development of the 3D model of the cyclotron magnet is essential.

At INFN-LNS in Catania the 3D model of the existing magnetic structure of the CS has been created using Opera-3d, as in the case of the development of the accelerating structure.

The CS magnet model has been used in this thesis work for extracting the 3D magnetic field map in the whole injection volume. Further out a measured median plane field map has been used and the magnetic field outside the median plane has been calculated by the AOC orbit code by expansion in the vertical direction. The two magnetic field maps have been merged at the chosen transition radius equal to 50 mm.

More details about the magnetic field computation for ion tracking are presented in Chapter 6 in the section dedicated to the development of the beam tracking model.

The created Opera-3d model contains the existing iron structure and the two pairs of superconducting coils. Fig. 5.9 shows the section of the model below the median plane. The azimuthal field modulation is produced by high-field sectors (hills), separated by low-field regions (valleys). The hill sectors are mounted on upper and lower plates of the yoke and are surrounded by the return yoke. The superconducting coils occupy, together with the cryostat, the space between the yoke and the pole sectors. The trim coils are not included in the model. This has no significantly effect on the ion tracking simulations from injection up to extraction for two reasons: (i) the first trim coil wound around each hill is at about 120 mm from the CS centre and, consequently, its effect is negligible in the region below the transition radius, (ii) the measured median plane field map contains the contribution of all the trim coils to the total magnetic field.
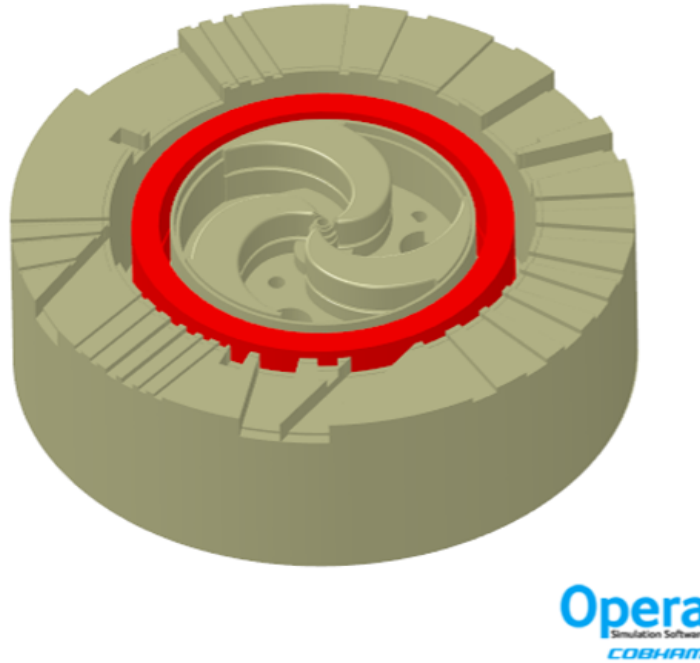
Figure 5.9: Opera-3d model of the magnetic structure of the LNS cyclotron.

The 3D model of the CS magnetic structure is symmetrical with respect to the median plane. Three-fold symmetry is not applicable to the model because of the presence of not-symmetrical radial penetrations in the yoke. These penetrations, that are visible in Fig. 5.9, were machined in the iron for different purposes, for example for the allocation of the coil supports or the handling systems of the elettrostatic deflectors.

More details about the existing penetrations in the yoke can be found in Fig. 2.5 in Chapter 3.

The same material label, named as iron, has been assigned to all the iron components of the system. Using this material label, a non-linear BH curve has been set to all the components of the CS magnet.

The current density value of each couple of the superconducting coils has been set for the acceleration of the chosen reference ion for the beam tracking study reported in Chapter 6, i.e. the ^{16}O fully stripped ion accelerated at the maximum energy of 100 MeV/amu, which lie on the

focusing line ($K_F = 200$) in the CS operating diagram (see Fig. 2.1). The TOSCA solver has been used for the calculation of the magnetic field created by the CS magnet and a non linear analysis has been set. As in the case of the 3D model of the CS accelerating structure, the Opera-3d Post-Processor has been used to process and display the calculated results by the TOSCA solver. Hereinafter, an example is shown. Fig. 5.10 shows the magnetic field along the vertical symmetry axis of the CS from the the yoke entrance up to the median plane. The curve is characterized by two sharp gradients, one close to the median plane, as in the conventional AVF cyclotrons, and the other one close to the plug extension end. Afterwards the field decreases almost linearly and, close to the yoke entrance, a slight positive gradient is present. The magnetic field close to the median plane is 31 kGauss.

Different contributions determine the behaviour of the field along the vertical symmetry axis of a superconducting cyclotron, as simulated by Bellomo and his co-workers for the MSU K1200 superconducting cyclotron (k800 at that time) [81]. The linear part of the curve comes from the coils, the first two peaks close to the median plane are due to the plug, placed in the cyclotron center to increase the beam vertical focusing, while the iron is responsible of the rapid decrease of the field immediately before the linear region and of the field gradient close to the yoke entrance. They also demonstrated that the curve trend remains the same changing the coil excitations for the acceleration of various ions at different final energies.

The high magnetic field along the vertical symmetry axis of a superconducting cyclotron acts as solenoid lens on the beam. It rotates the beam and the sub-phase spaces get correlated, as shown in the next chapter. For efficient injection, the beam has to be matched with respect to the optical properties of the cyclotron axial bore.
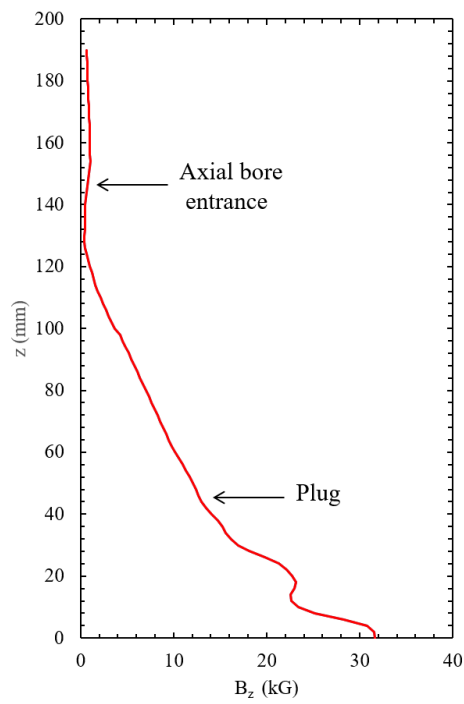
Figure 5.10: Magnetic field along the axial bore of the LNS cyclotron. The current density value of each couple of the superconducting coils has been set for the acceleration of the ^{16}O fully stripped ion at the maximum energy of 100 MeV/amu.

Chapter 6

Development of the beam tracking model

The quality of an accelerated beam, defined in terms of emittance, intensity and energy resolution, is to a large extent determined in the first few turns in the cyclotron centre. Therefore, the shape and the position of each electrode in the central region have to be designed such as to obtain good beam properties especially in terms of horizontal centring, vertical focusing and phase acceptance. The process of the beam acceleration in the first turns in the cyclotron requires careful studies, also in our case of the upgrade of the CS.

Numerical beam tracking simulations from the axial bore entrance, through the present spiral inflector and central region, up to the extraction system have been done and are presented in this chapter.
Beam tracking up to the extraction system is needed in order to obtain the beam characteristics, in particular the energy spread, of the extracted beam. As already mentioned in chapter 3, a beam energy selection system will be placed outside the CS to reduce the energy spread, if it would be larger than the NUMEN requirement. However, only 2 kW beam power can be stopped by this system due to radiation limit imposed by the wall concrete shielding. Therefore, the extracted beam energy spread should be as low as possible.

A process of RF phase selection in the CS central region has been also investigated as further means to reduce the energy spread.

The final energy spread at extraction depends not only on the energy gain per turn but also on the radial beam size. This second factor plays an important role in the case of the CS due to the large injected emittance.

The most important question in this chapter concerns the overall efficiency of beam transmission from the cyclotron bore injection up to the energy selection process; for a given energy spread requirement, this efficiency is determined by the losses in the spiral inflector and central region, the losses due to the RF phase selection process, the losses in the extraction system and the losses due to the energy selection process.

Hereinafter, a brief description of the chapter sections.

In Section 6.1 the main features of the tracking model are described.

In Section 6.2 the optimization of the beam centroid through the spiral inflector and central region is presented.

The spiral inflector is a complicated 3D electrostatic structure that provides a 90° bend from the vertical direction into the median plane.

The design of a spiral inflector is complicated mainly for two reasons: i) the electrical fringe fields at the inflector entrance and exit form a substantial part of the total electric field integral and ii) the magnetic field in and around the spiral inflector volume is not uniform.

A good design requires that: i) the beam at the exit of the inflector is well centered vertically with respect to the median plane, ii) the beam after transmission through the central region is well centred radially with respect to the vertical cyclotron axis and iii) the losses in the inflector itself are as small as possible. As first step, the motion of the beam centroid through the spiral inflector was studied, in order to verify that these requirements were correctly met. This is indeed the case: the vertical centring can be slightly adjusted and optimized by fine-tuning of the

electrode voltages. It is found that there is no direct need to re-design this inflector; we therefore kept it as it is in our studies.

Calculations of RF phase acceptance of the CS are also presented in the same section. A cyclotron is an RF accelerator and is therefore not able to accept and accelerate the full DC beam coming out from the ion source. A buncher can be used to compress the DC beam into bunches that are better matched to the RF structures in the cyclotron.

Besides that, also the cyclotron central region geometry is a dominant factor for determining the RF phase width that can be accepted.

There are two effects that need to be considered: i) the axial ion motion in the cyclotron centre is dominated by strong phase dependent RF electric forces in the dee gaps and ii) the orbit centring shows a dependence on the particle RF phase.

In the CS, the spiral inflector and its housing can be rotated around the vertical axis. We evaluated the RF phase acceptance for three different angular positions in order to estimate the optimum orientation of the inflector. We also studied the effect of the dee voltage extensively.

In Section 6.3 the study of the beam optics in the injection system is presented. Beam optics depends on the phase space of the injected beam. The injected beam emittance is reasonably well known; however, the precise shape of the phase space is not and this complicates the study.

We therefore made two assumptions about the injected beam as follows: i) the injected beam has rotational symmetry (with respect to the beam axis) and ii) the beam is well matched with respect to the optical properties of the cyclotron axial bore. The reasoning behind this is as follows: i) in general the matched beam provides the best condition for optimum transmission through an optical system (in terms of beam losses and beam quality), ii) the CS injection line has a matching section that allows to inject optimally into the cyclotron iii) it is assumed that a natural tuning process of the injection line will approach the matched solution.

The best match was found with the aid of the optical beam transport program TRANSPORT [82]. Besides the matching, also the RF phase dispersion effect in the axial bore and through the spiral inflector has been studied and the results are presented in the same section.

The results of the simulations about the injection efficiency are reported in Section 6.4. In Section 6.5 and 6.6 simulations of the extracted energy spread and of the total transmission efficiency are presented respectively. The use of central region phase selection slits is studied as well as the use of an energy selection system outside the CS.

In Section 6.7 some possible improvements of the central region, resulting in better injection efficiency are presented.

6.1   Main features

The interest in precise accelerator beam dynamics simulations has grown in recent years enabled by rapidly increasing computer technology capabilities. The beam tracking model of the INFN-LNS Superconducting Cyclotron has been developed using AOC (Advanced Orbit Code) [80], a precise ion tracking code. It is a C based simulation code, developed by the IBA (Ion Beam Applications) company for orbit and beam simulations in all their different types of accelerator, such as isochronous cyclotrons, synchro-cyclotrons, rhodotrons, for medical and industrial applications. IBA is involved in the project of the LNS cyclotron upgrade concerning the central region study. Its orbit tracking code has been used in this thesis work for particle orbit calculations in the LNS cyclotron under the combined action of magnetic and electric fields.

As already described in Chapter 2, the CS operates in the so-called constant orbit mode in order for the central region to be valid for the acceleration of all the ions within the operating diagram of the LNS cyclotron. According to the scaling rule given by Eq. (2.4.1), an ion which requires the highest dee and injection voltages was chosen as reference ion for the

beam tracking study reported in this chapter. In particular, all the simulations have been carried out for the fully stripped ^{16}O ion accelerated at the maximum energy of 100 MeV/amu, which lies in the focusing line ($K_f = 200$) in the CS operating diagram (see Fig. 2.1).

The particle rest mass and charge of the reference ion are given as input in the AOC code. Table 6.1 contains the CS operating setting for injection and acceleration of the chosen reference ion used in the beam dynamics study.

A left-handed coordinate system is set in the AOC code such that a positive ion moving in a magnetic field aligned along the positive z-axis, rotates counter-clockwise (i.e. in the direction of increasing azimuth). Then, the equation of motion for each accelerated particle is given by:

$$\frac{d}{dt}(m\vec{v}) = e(\vec{E} - \vec{v} \times \vec{B}) \qquad (6.1.1)$$

Here, t (time) is the independent variable, m is the relativistic mass of the particle, e is the charge of the ion, $\vec{v}$ is the particle velocity vector and $\vec{E}$ and $\vec{B}$ are the electric and magnetic fields acting on the particle. The ions move in a static magnetic field and they are accelerated by

Centre magnetic field	31.3 kG
Coil currents	I_α: 1609.43 A
	I_β: -539.89 A
Source voltage	30 kV
Spiral inflector voltage	$\pm$ 6.3 kV
Dee-voltage	86 kV
RF-frequency	48.1 MHz
Harmonic h	2

Table 6.1: Operating setting of the CS for injection and acceleration of the fully stripped ^{16}O ion up to the final kinetic energy equal to 100 MeV/amu.

time-varying electric fields. The static electric field generated by the spiral inflector is used for the axial injection of ions onto the median plane. As already explained in Chapter 5, the total electric field $\vec{E}(\vec{r}, t)$ to be used in the simulation study can be written as the linear superposition of field maps produced by all the separate electrodes existing in the cyclotron, each one driven by a separate boundary condition on the dee voltage. The total electric field is written as follows:

$$\vec{E}(\vec{r}, t) = V_{dee\ N1}\ \vec{E}_{dee\ N1}(\vec{r})\ sin(h\omega_0 t)\ +$$

$$+ \sum_{Ni=2}^{3} V_{dee\ Ni}\ \vec{E}_{dee\ Ni}(\vec{r})\ sin(h\omega_0 t +\ \phi_{dee\ Ni}) + \sum_{i=1}^{2} V_{SI_i}\ \vec{E}_{SI_i}(\vec{r}) \quad (6.1.2)$$

Here, $V_{dee\ Ni}$ $(Ni = 1, 2, 3)$ is the voltage amplitude applied to the dee Ni, V_{SI_i} $(i = 1, 2)$ is the voltage amplitude applied on the spiral inflector electrode i, $\vec{E}_{dee\ Ni}(\vec{r})$ $(i = 1, 2, 3)$ is the 3D electric field map obtained by applying a voltage of 1 Volt to the dee Ni, $\vec{E}_{SI_i}(\vec{r})$ $(i = 1, 2)$ is the 3D electric field map obtained by applying a voltage of 1 Volt to the inflector electrode i, h is the harmonic number, ω_0 is the circular frequency of the ion and $\phi_{dee\ Ni}$ $(i = 2, 3)$ is the phase of the N2 and N3 dees with respect to the other one, assumed as reference. Since the three-fold symmetry LNS cyclotron works in $h = 2$ harmonic mode, the RF cavities oscillate $\pm 120°$ out phase with respect to each other.

Numerical integration of the equation of motion of the accelerated particles is done using as independent variable the time conveniently scaled. A new independent variable τ is defined, which measures the phase advance of the RF voltage, divided by the harmonic number h:

$$\tau = \omega_0 t = 2\pi\ \frac{f_{RF}}{h}\ t \quad (6.1.3)$$

where ω_0 is related to the RF frequency f_{RF} as follows:

$$\omega_0 = 2\pi\ \frac{f_{RF}}{h} \quad (6.1.4)$$

Harmonic number h equal to 2 means that the frequency of the RF voltage is twice the revolution frequency of the particle.

When a particle starts its motion in a position along the vertical CS axis, the time spent to travel along the axis corresponds to a phase advance of the RF voltage and, consequently, the particle is injected onto the median plane with a RF phase shifted in time with respect to the initial one.

As usual for circular accelerators, the origin of time is taken at the zero crossing of the RF voltage with positive slope and the phase of a particle with respect to the RF voltage is defined as the phase of the RF voltage when the particle is in the middle of the accelerating gap.

The orbit properties are calculated at discrete values of the independent variable τ, with the first value coincident with the starting phase of each particle and the τ-step $\Delta\tau$ is obtained from the number of intervals per orbit period N_t (specified by the user at program input) as follows:

$$\Delta\tau = \frac{2\pi}{N_t} \tag{6.1.5}$$

The magnetic field used in the simulations is read both from a median plane field map, obtained from field measurements, and from the full 3D field map, obtained from the Opera-3d model of the CS magnetic structure. The main properties of the 3D model of the LNS cyclotron magnet has already been presented in Chapter 5.

Three-dimensional magnetic field data are needed in the cyclotron centre due to the presence of the spiral inflector, further out a median plane field map is good enough for ion tracking. A transition radius is set to 50 mm: for radii below this value, the full 3D field map is used and, for radii larger than 50 mm, the median plane field map is considered.

For radii smaller than the transition radius, the values of the three components of the magnetic field, extracted from the Opera-3d model of the LNS cyclotron magnet, are specified on a 3D polar mesh and the field at any point in the beam tracking volume is calculated by AOC by means

of 3D polynomial interpolation in this grid.

In the median plane field map, the magnetic field is specified on a 2D polar grid. Within the tracking volume, the field at any point on the median plane is calculated by AOC by means of 3D polynomial interpolation in this grid, outside the median plane it is obtained by expansion with respect to the z coordinate.

The electric field in AOC is calculated starting from the 3D electric potential maps, one for each electrode, extracted from the Opera-3d model of the CS accelerating structure. The main properties of the 3D model of the accelerating structure of the INFN-LNS Superconducting Cyclotron has already been presented in Chapter 5.

The electric potential map for each independent electrode of the Opera-3d model is obtained specifying the values on a 3D polar grid and later all the maps are combined in one file. The electric field components are obtained in any point of the beam tracking volume by interpolation and differentation of the electric potential in the 3D polar grid.

The polar grids for the magnetic field map and the potential field maps are customized in detail in order to have maximum flexibility for the mesh node location. Each mesh is subdivided in several sub-meshes. In this way, a high number of mesh points are concentrated only in the regions where a high accuracy of the calculated fields is required and not in the full beam tracking model. The use of multiple sub-meshes is mandatory due to the large sizes of the beam tracking model, indeed it extends radially up to the pole end (900 mm) and vertically up to very close the axial bore entrance (1440 mm from the median plane).

The AOC orbit code can detect particle hits with (or very close to) an accelerating structure electrode or a magnetic iron part, during the interpolation of the field maps at the current particle position for ion orbit integration. In order to detect ion losses on the accelerating structure electrodes, an indicator for the material properties is defined in the

Opera-3d model; in particular, a charge density (so small that it does not change the electric field) is assigned to all the electrodes, as already reported in Chapter 5. The values of the charge density are extracted by the Opera-3d Post-Processor in each point of the 3D polar grid, used for the potential field maps, and then the indicator-map are included in the 3D total potential map.

During ion orbit integration, the indicator is tested on the eight corners of the cubic sub-mesh that encloses the current field point.

If the charge density at one or more of these corners was non-zero, the particle is considered to hit an electrode. Consequently, the electric field components at the current particle position is put to zero and the orbit integration for the particle is stopped. The same occurs for detecting losses of particles on magnetic iron elements but, in this case, the indicator-map contains the values of the relative permeability μ_r. The use of this tool in AOC, in combination with the simulation of a differential radial probe in the beam tracking model, allows to study beam transmission and beam losses in the INFN-LNS Superconducting Cyclotron.

In addition to the differential radial probe, other kinds of post-processing option are used for the analysis of calculated ion and beam orbits, for example the intersection of particle orbits with multiple patches are simulated to calculate the beam properties in specific positions in the cyclotron. The patch in AOC is a plane with infinite vertical extension and specified by the coordinates of its end points in the median plane.

Moreover, as already reported in Chapter 5, for a better understanding of the simulation results, the calculated orbits can be visualized in the Opera-3d Post-Processor with the aid of a dedicated tool developed by IBA.

6.2 Study and optimization of the beam centroid

6.2.1 Motion through the spiral inflector

Although the spiral inflector is a small component of a cyclotron due its reduced sizes, it contribuites significantly in establishing the optical properties of the accelerated beams.

In the ideal case, the electric field between the electrodes of the spiral inflector is uniform and it extends only in the region between the electrodes. Actually, the fringing field is also present in the region before the entrance and after the exit gaps, as shown in Fig. 5.8 in the case of the CS spiral inflector. It is reasonable to expect that electric fringe fields at the inflector entrance and exit influence the motion of the beam particles with respect to the ideal case. The design of the spiral inflector requires the use of a reasonable model of the electric fringe fields at the inflector entrance and exit as well as the use of 3D magnetic field data in order to take into account the non-uniformity of the field in and around the inflector volume. Only if a reasonable model of the electric fringe fields is used, we can expect that the beam centroid orbit presents only small deviations from the ideal design orbit of the inflector. These could be corrected by small adjustments of the voltage on the inflector electrodes. If not, the re-design of the spiral inflector based on a more realistic electric fringe fields model is needed. Collimators before and after the spiral inflector could be also used to further reduce the electric fringe fields. In the LNS cyclotron, the collimator placed before the spiral inflector entrance is far enough away from the electrostatic device and then its only function is to protect the electrodes from the particle hits.

The motion of the beam centroid through the existing spiral inflector has been studied in order to test and optimize the injection properties of the existing device of the LNS cyclotron.

A position on the vertical axis of the LNS cyclotron was chosen as starting point for the beam centroid tracking. In particular, the starting position was set at the distance of 200 mm from the median plane, corresponding to a distance of 129 mm from the collimator, placed in the axial bore before the inflector, and 173 mm from the spiral inflector entrance (see Table 2.6).

In the case of the LNS existing spiral inflector, small adjustments of the inflector voltage with respect to the nominal value have been sufficient to adjust and optimize the beam centroid orbit, without the re-design of the spiral inflector. Figure 6.1 shows the vertical coordinate of the beam centroid close to the median plane, when the voltage applied on the inflector electrodes is the nominal value (± 6.3 kV) and the optimized value (± 6 kV) respectively. The dependent variable on the horizontal axis in the plot is the distance travelled by the particle, evaluated with respect
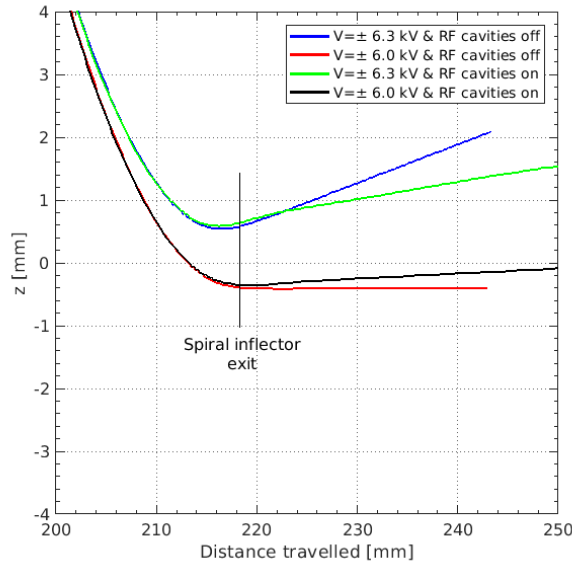

Figure 6.1: Vertical coordinate of the beam centroid close to the CS median plane when the applied inflector voltages are ± 6.3 kV and ± 6 kV. The distance travelled by the particle is evaluated with respect to the initial tracking position. In the interval [200-250] mm, $\tau/2\pi$ varies from 2.8 to 3.3.

to the initial position chosen for the ion tracking.

As one can see from a comparison between the blue and red curves in Fig. 6.1, the decrease of the electrode voltage allows to reduce the positive momentum vertical component of the beam central particle to a value very close to zero at the inflector exit. However, the beam centroid is injected into the CS with a slight vertical offset of about 0.4 mm with respect to the median plane.

When a vertical offset between the cyclotron median plane and the exit plane of the spiral inflector is present, even if it is small, a vertical oscillation of the particle around the median plane occurs during acceleration in the cyclotron. In general, a small vertical oscillation is always present because it is difficult to reduce it to zero. In Fig. 6.1 only the beginning of the vertical oscillation is visible (green and black curves).

For a better understanding of what occurs when the particle exits the inflector with a vertical offset with respect to CS median plane, Fig. 6.2 shows the vertical oscillation of the beam centroid during acceleration in the CS. The curves are referred to a different values of the inflector voltage lower than the nominal value. As in Fig. 6.1, the distance travelled by the particle is calculated with respect to the starting tracking position. The number of turns made by the particle in the CS is about nine. As one can see from a comparison between the curves, the inflector voltage that allows to minimize the vertical oscillation amplitude of the beam centroid, during particle acceleration in the CS, is ± 6 kV, the above-mentioned value.

A good centring of the beam central particle with respect to the spiral inflector electrodes is also essential for minimizing beam losses in the inflector. In the ideal case, the inflector design orbit moves in the spiral inflector along an equipotential surface with constant energy, equal to the injection energy of the reference ion, and it always maintains the same distance from the electrodes. Actually, a variation of the beam centroid
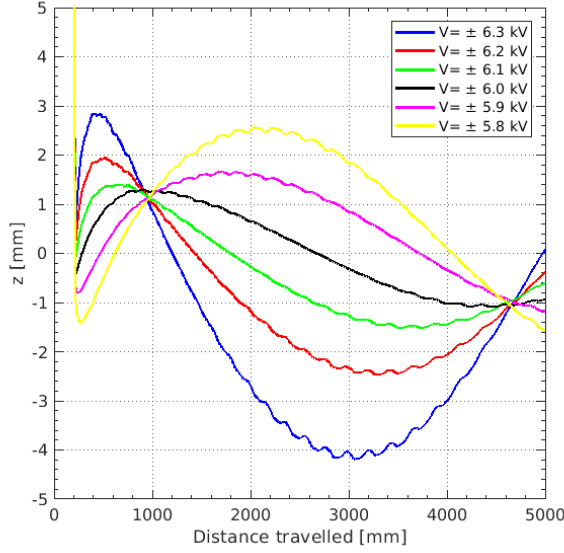
Figure 6.2: Vertical coordinate of the beam centroid in the CS when different voltages are applied on the inflector electrodes. The distance travelled by the particle is evaluated with respect to the initial tracking position. In the interval [0-5000] mm, τ/pi varies from 0 to 12.2. The beam centroid makes about nine turns in the CS.

energy is present during the motion of the particle in the electrostatic device, as shown in Fig. 6.3 on the left. This is associated with a offset in position of the beam centroid with respect to the ideal case, as one can see in Fig. 6.3 on the right. Figure 6.3 has been obtained supposing the optimized voltage applied on the inflector electrodes. These variations can be explained as effects of the electric fringe fields on the particle motion at the entrance and exit of the spiral inflector. Before the beam centroid enters the inflector, the electric fringe field first decelerates and later accelerates the particle and pushes it off the vertical CS axis. Therefore, the particle enters the spiral inflector with a slight offset with respect to the inflector design orbit and with a small different energy with respect to the ideal case. Consequently, the beam centroid orbit will be slightly different with respect to the inflector design orbit. Also the electric fringe field at the inflector exit influences the beam cen-
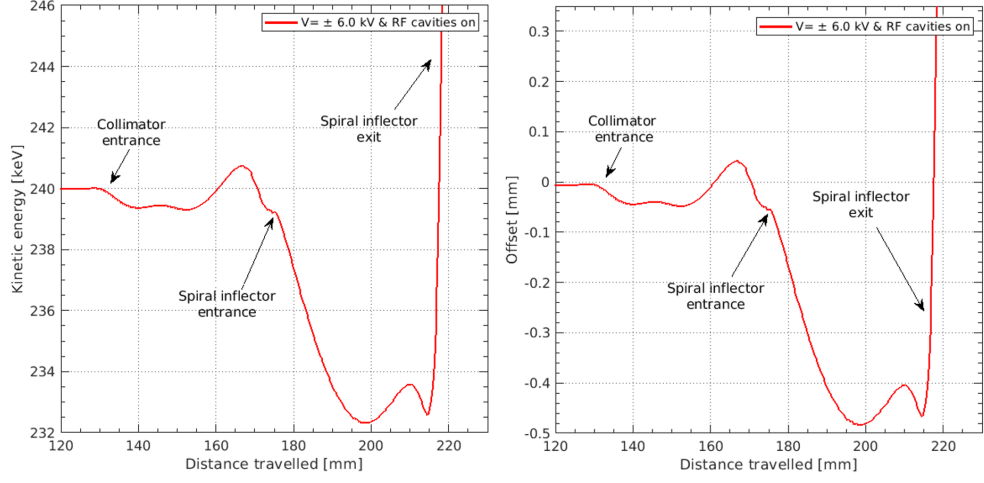
125

Figure 6.3: On the left, energy of the beam centroid through the spiral inflector. On the right, offset of the beam centroid orbit with respect to the inflector central orbit. The distance travelled by the beam centroid is calculated with respect to the initial tracking position. In the interval [120-230] mm, $\tau/2pi$ varies from 1.7 to 3.2

.

troid motion. The rapid increase of the beam centroid energy in the plot in Fig. 6.3 on the left is a consequence of the accelerating electric field acting on the particle before the beam centroid leaves the inflector.

The maximum variation of the beam centroid energy in the inflector with respect to the injection energy has been evaluated. It is 7.8 keV, corresponding to a maximum offset in position of the beam centroid with respect to the inflector central orbit of about 0.5 mm, an acceptable value considering that is less than the 10% of the distance between the inflector electrodes.

6.2.2   RF phase acceptance of the CS

Once optimized the motion of the beam centroid through the spiral inflector, the acceleration of a pencil beam in the INFN-LNS Superconducting Cyclotron has been studied. To simulate the motion in the cyclotron of a beam composed of some thousands of particles requires a lot

of time and data storage but, in any case, it do not allow to understand clearly the strong dependence of the orbit centre and vertical focusing in the CS centre on the phase of the RF dee voltage. The pencil beam, although it is a simplified representation of a beam, allows to understand these important properties.

As already reported in the introduction of this chapter, a cyclotron is not able to accept and accelerate the full DC beam coming out from the ion source. Therefore, calculations of RF phase acceptance become fundamental in order to evaluate the particle RF phase width the cyclotron is able to accelerate.

The simulations have been carried out assuming the starting position already considered for the study of the beam centroid motion through the spiral inflector. The RF phase width that can be accepted by the CS is constrained by the clearance for the beam in the first turns due to the presence of electrodes intercepting the median plane (the so-called pillars), and the vertical gap between the accelerating electrodes that stay above and below the median plane. Beam horizontal centring and vertical focusing requirements limit the acceptable phases to a range even smaller. As described in Chapter 2, vertical focusing in the cyclotron centre is mainly provided by the RF electric field, that is also responsible of the ion acceleration, and then it is particle RF phase dependent.

Also the orbit centring depends on the particle RF phase.

For a better understanding of these processes, Fig. 6.4 shows the smoothed orbit centre and the vertical coordinate of the pencil beam as a function of $\tau/2\pi$.

We assumed the pencil beam starting its motion at different RF phases at the starting tracking position. When the pencil beam moves in the cyclotron, the number of full periods of the RF voltage (divided by h) approximately coincides with the number of orbital turns carried out by the pencil beam. In Fig. 6.4, the pencil beam enters the central region
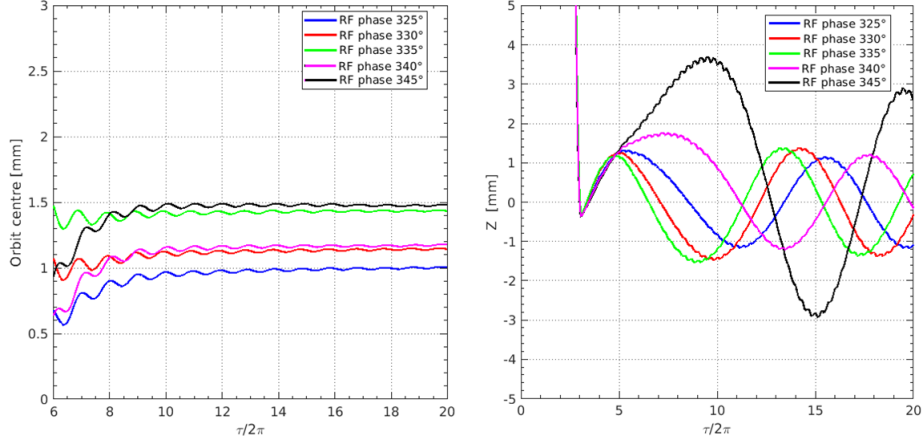
Figure 6.4: On the left, orbit centre after six periods of the RF voltage (divided by h) for different initial RF phases. On the right, vertical coordinate of the beam centroid in the first twenty periods of the RF voltage (divided by h) for different initial RF phases.

after about three full periods carried out by the RF voltage (divided by h). In the figure on the right, after the pencil beam enters the central region, the vertical oscillation amplitude is RF phase dependent. For all the phases excluded 345° the maximum shift of the pencil beam with respect to the median plane stays around 1 mm while a larger vertical oscillation amplitude is observed for the remaining RF phase. On the left, the smoothed orbit centre is plotted after six full periods of the RF voltage (divided by h) when the pencil beam is already on the median plane. For each integration point, the smoothed orbit centre is calculated as the average of the data points contained in a 360° complete azimuthal advance of the spiral orbit. As one can see in the figure, the smoothed orbit centre starts to be stable after $10 \cdot \tau/2\pi$ and it varies from about 1 mm to 1.5 mm for the chosen RF phase width.

The geometry of the central region, and especially the geometrical configuration spiral inflector-puller, plays an important role in determining the properties of the accelerated orbits in the cyclotron after ions leave the spiral inflector. In order to maximize the beam transmission after the central region, the entire existing inflector assembly of the CS is designed

to rotate and move vertically during the beam tuning for fine adjustment of the exit position of the ions from the spiral inflector. Clockwise and anticlockwise rotations are permitted and the maximum rotation angle in both directions depends on the minimum allowed distance between the housing and the non-grounded electrodes of the central region that avoids sparking problems.

The geometrical features of the spiral inflector and housing are well known; however, their present angular position within the CS is not and this complicates the study. It is not known if the position of the inflector in the CS coincides with the one reported in the 3D engineering drawing of the accelerating structure of the CS (CAD file), or if it was adjusted during the commissioning of the CS axial injection system.

Recent vacuum seal problems prevent the opening of the LNS cyclotron for site inspection, except in case of particular needs. We therefore evaluated the RF phase acceptance for different angular positions of the entire inflector assembly with respect to the vertical CS axis in order to estimate the optimum orientation of the spiral inflector. In particular, we considered three positions. The first one corresponds to the position reported in the 3D engineering drawing of all the electrodes of the LNS cyclotron, from which the Opera-3d model of the CS accelerating structure has been created. The other two positions have been obtained from the first one rotating the electrodes of $+5°$ and $-5°$ respectively, as shown in Fig. 6.5.

The study was also carried out supposing to apply different dee voltages, both lower and higher than the nominal one (V_{dee}= 86 kV).

Figure 6.6 shows the RF phase acceptance for the horizontal motion as a function of the dee voltage and the position of the spiral inflector. More details about the RF phase intervals can be found in Table 6.2.

Figure 6.7 shows the minimum and maximum value of the orbit centre and its amplitude for each RF phase range reported in the Table 6.2. These quantities have been estimated after 20 turns. The plot shows
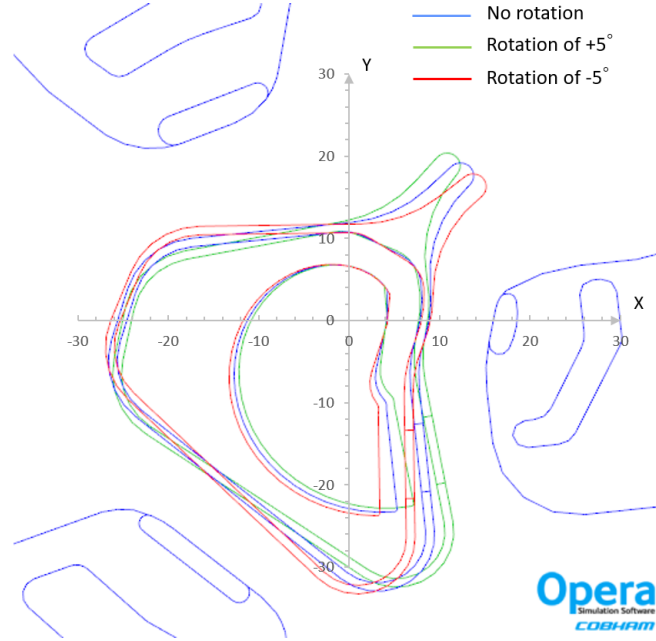
Figure 6.5: The three angular positions of the spiral inflector and its housing considered in the simulations. Each colour indicates a different position of the electrodes. The electrodes in blue are positioned as in the CAD file of the CS central region.

Dee voltage (kV)	Spiral inflector rotation		
	0°	+5°	−5°
80	/	/	/
86	35° [319°-354°]	47° [323°-370°]	/
90	50° [312°-362°]	54° [320°-374°]	36° [308°-344°]
95	64° [304°-368°]	64° [317°-381°]	46° [308°-354°]

Table 6.2: RF phase acceptance for the horizontal motion as function of the dee voltage and the rotation angle of the spiral inflector with respect to the z-axis. The rotation angles are defined with respect to the position of the spiral inflector in the CAD file. The values of the particle RF phase are referred to the position placed at 200 mm from the median plane along the z-axis.
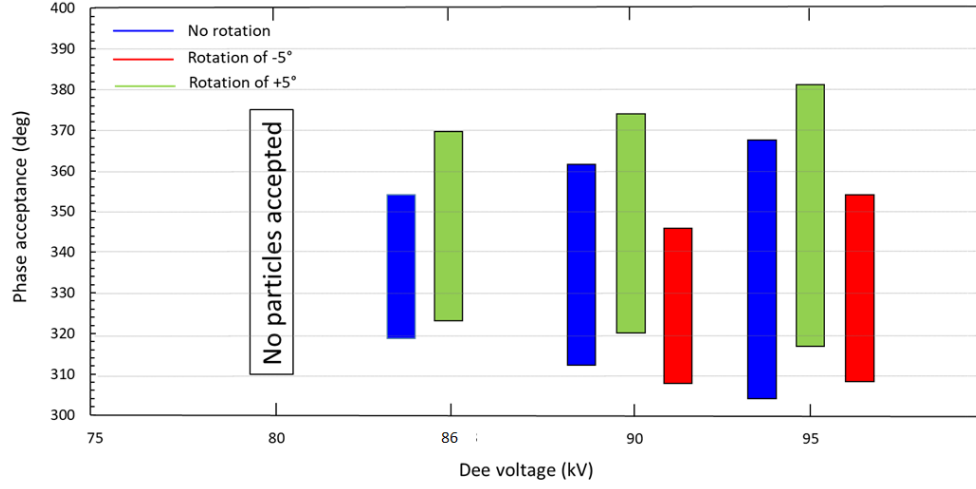
130

Figure 6.6: RF phase acceptance for the horizontal motion as function of the dee voltage and the rotation angle of the spiral inflector with respect to z-axis. The values of the particle RF phase are referred to the position placed at 200 mm from the median plane on the z-axis.

that the average orbit centre increases when the dee voltage rises for each inflector position. In addition, the plot shows that the rotation of the spiral inflector of $+5°$ around the z-axis has the positive effect to decrease the amplitude orbit centre for any considered dee voltage. The spread is larger because the RF phase acceptance is larger, as shown in Fig. 6.6.

The RF phase acceptance is limited by the amount of vertical focusing available in the first turns. Vertical losses on the electrodes decrease the RF phase width the CS is able to accelerate. A simple way to estimate the effect on the vertical focusing of the RF phase is by giving a vertical kick to the pencil beam at the spiral inflector exit. A vertical kick of 87 mrad, approximately equal to the value of the beam divergence, has been applied. We evaluated the CS vertical acceptance for all the cases reported in Table 6.2 by the aid of the application of a vertical kick to the beam centroid at the housing exit.

The RF phase acceptance of the CS for both the horizontal and vertical motion in the cyclotron, as function of the dee voltage and spiral inflec-
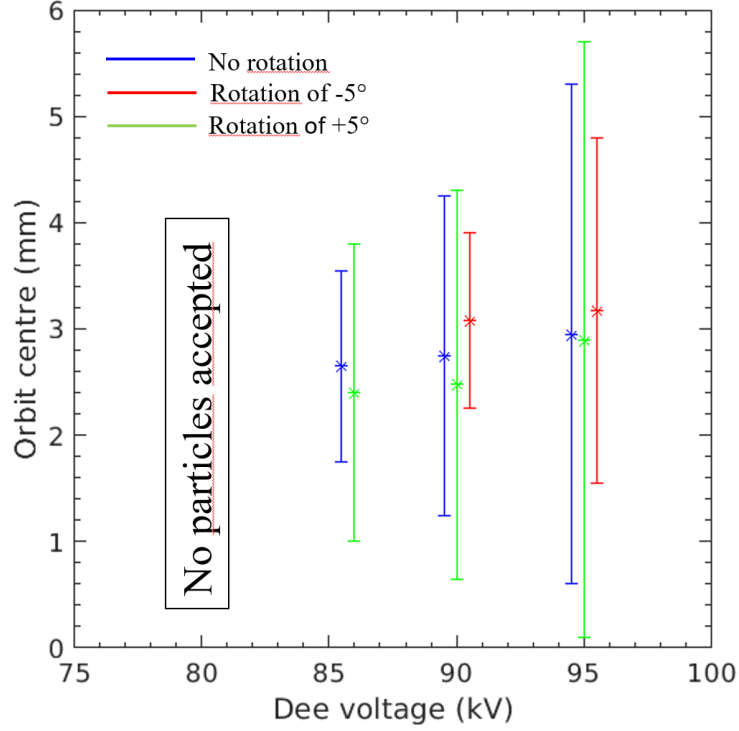
Figure 6.7: The minimum, the maximum and the average values of the orbit centre are plotted as a function of the dee voltage and the rotation angle of the spiral inflector with respect to z-axis.

tor position, is listed in Table 6.3. As one can see, for the nominal dee voltage, the rotation of $+5°$ of the spiral inflector with respect to the CAD position allows to obtain the higher RF phase acceptance, instead no particles are transmitted when the spiral inflector is rotated of the same angle in the opposite direction. In addition, the use of dee voltage higher than the nominal one allows to enlarge the interval of RF phases accepted by the CS for any rotation of the spiral inflector and its housing.

Looking at the results of the simulations, we decided to rotate in the tracking model the spiral inflector of $+5°$ with respect to the CAD position since it allows to obtain the higher RF phase acceptance and the smaller average orbit centre for all the considered dee voltage values.

Dee voltage (kV)	Spiral inflector rotation		
	0°	+5°	−5°
80	/	/	/
86	35° [319°-354°]	41° [328°-369°]	/
90	44° [317°-361°]	48° [326°-374°]	36° [308°-344°]
95	54° [314°-368°]	59° [322°-381°]	40° [314°-354°]

Table 6.3: RF phase acceptance for the horizontal and vertical motion as function of the rotation angle of the spiral inflector with respect to the z-axis and of the dee voltage. The rotation angles are defined with respect to the position of the spiral inflector in the CAD file. The values of the particle RF phases are referred to the position at 200 mm from the median plane on the z-axis.

6.3 Study of beam optics in the injection system

6.3.1 Beam matching in the yoke bore

As already reported in Chapter 3, the existing CS injection line is not equipped with beam diagnostic systems, such as emittance measurement devices and beam monitors. Consequently, it was not possible to use, in the simulation study reported in this chapter, measured quantities of the injected beam i.e. the exact beam phase space and beam emittance value. Therefore, reasonable assumptions were made on the injected beam to be simulated.

As reported in the introduction of this chapter, the first hypothesis is that the injected beam has rotational symmetry with respect to the beam axis. This implies that the beam emittance is the same in both transverse phase spaces.

For particle orbit simulations, where the phase space coordinates of all particles in the beam are determined, it is convenient to define the emittance in a statistical way, based on the particle distribution in the phase

space. The statistical emittance, the so-called geometrical r.m.s. emittance, is defined as:

$$\epsilon_{geom, \ r.m.s.} = \sqrt{<x^2><x'^2> - <xx'>^2} \qquad (6.3.1)$$

where $<>$ are the second-order moments of the particle distribution:

$$<x^2> = \frac{1}{N_{part}} \sum_{i=1}^{N_{part}} (x_i - \bar{x})^2 \qquad (6.3.2)$$

$$<x'^2> = \frac{1}{N_{part}} \sum_{i=1}^{N_{part}} (x'_i - \bar{x}')^2 \qquad (6.3.3)$$

$$<xx'> = \frac{1}{N_{part}} \sum_{i=1}^{N_{part}} (x_i - \bar{x})(x'_i - \bar{x}') \qquad (6.3.4)$$

Here, N_{part} is the number of the particles of the beam, $\bar{x} = \sum_{i=1}^{N_{part}} x_i$ is the average of all the coordinates x_i of the particles and $\sum_{i=1}^{N_{part}} x'_i$ is the average of all the divergences x'_i of the particles.

The normalized emittance ϵ_{norm} is defined as:

$$\epsilon_{norm} = \beta\gamma\epsilon_{geom} \qquad (6.3.5)$$

where $\beta = \frac{v}{c}$ and $\gamma^2 = \frac{1}{1-\beta^2}$, being v the light velocity. Ideally, the normalized emittance does not change during acceleration.

The meaning of the r.m.s. emittance is related to the amount of beam particle that is enclosed by the ellipse. This, of course, depends on the particle distribution shape. For example, for a Gaussian distribution, $4 \pi \epsilon_{norm, \ r.m.s.}$ corresponds to a contour containing 86% of beam particles while 100% of particles are contained in case of a uniform distribution [83]. In the simulation study reported in this chapter, we assumed a water-bag like distribution of particles.

Moreover, we supposed that the emittance at the CS axial bore entrance is equal to the value of the beam emittance at the ion source extraction. This is a good approximation if the beam optics between the ion source

and the cyclotron is linear and misalignment errors are not present along the beam injection line. r.m.s. emittance is conserved in linear system. The beam emittance at the extraction ion source is reasonably well known theoretically. In general, both the ion temperature and the magnetic field within ion sources determine the beam emittance. For ECR ion sources, the effect of the magnetic field dominates the emittance compared to the effect of the ion temperature, due to the high magnetic field in the extraction region. The normalized r.m.s. emittance, due to the magnetic field, depends on the charge-to-mass ratio Q/A of the ion, the magnetic field at the extraction region B_{extr} and the radius of the extraction hole r. Assuming a water-bag distribution, it is valid that [84]:

$$\epsilon_{norm,\ r.m.s.} \sim 0.032\ r^2 B_{extr} \frac{Q}{A} \qquad (6.3.6)$$

where $\epsilon_{norm,\ r.m.s.}$ is expressed in π mm-mrad, B_{extr} in T, r in mm and A/Q is dimensionless.

A normalized emittance equal to $1\pi \cdot$ mm-mrad has been set in the simulation study. This value corresponds to a geometrical emittance of $175\pi \cdot$ mm-mrad at the injection energy. The chosen emittance value is conservative, exceeding of about 10% the normalized emittance usually delivered by the ECR ion sources for the fully stripped ^{16}O ion beam.

As example, we report the calculated normalized r.m.s. emittance for the reference ion beam delivered by the SERSE ion source. According to Eq. 6.3.6, $\epsilon_{norm,\ r.m.s.}$ is about $0.9\pi \cdot$ mm-mrad, considering that the magnetic field at the extracton region B_{extr} is 1.6 T and the radius of extraction hole r is 6 mm in the SERSE ion source, as described in Chapter 2.

Finally, we supposed that the injected beam is well matched with respect to the optical properties of the CS axial bore. This is a reasonable assumption for the reasons already reported in the introduction of the chapter. A beam optics study through the axial bore of the LNS cyclotron was performed with the aid of the optical beam transport pro-

gram TRANSPORT in order to find the best match.

The CS magnetic field along the vertical axis (see Fig. 5.10) has been approximated as a succession of solenoids, each of length 20 mm. Simulations of beam back-integration from the median plane up to the axial bore entrance were carried out, assuming that the beam forms a waist on the median plane and considering the value of the geometrical emittance above-mentioned as constraint. The beam envelope has been calculated as a function of the beam half-size on the median plane. As an example, the envelopes of three beams with different initial half-size, equal to 1.5 mm, 2 mm and 2.5 mm respectively, are shown in Fig. 6.8.

The beam optics in the CS axial bore depends on the phase space of the injected beam. As described in Chapter 5, in all superconducting cyclotrons, the magnetic field along the vertical axis is very different from that of conventional AVF cyclotrons, achieving values relatively high close to the median plane. The CS magnetic field in the axial bore may highly correlate the beam transverse phase spaces in absence of a good match of the beam with the optical properties of the CS axial bore.
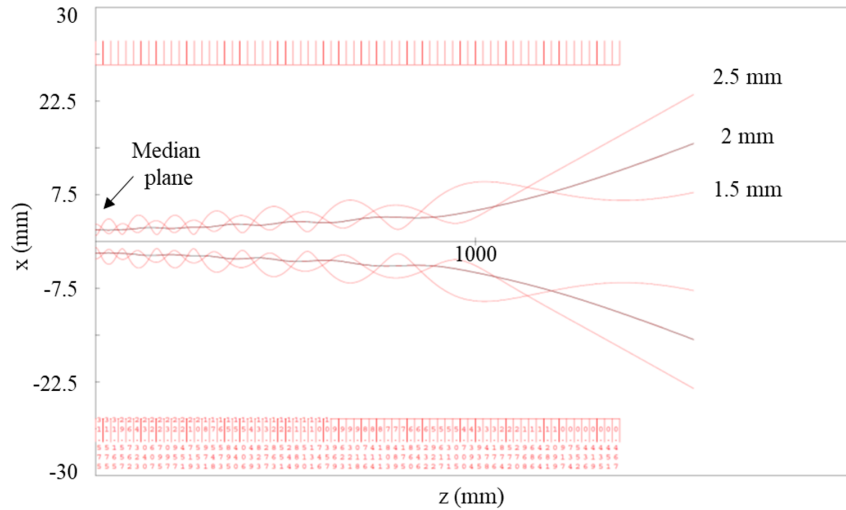

Figure 6.8: Envelopes of three beams with different initial half-size (x=1.5 mm, 2 mm, 2.5 mm) from the median plane up to the yoke bore entrance.

A mismatched beam is characterized by envelope width oscillations when the beam propagates through the axial bore, as in the case of the beams with half-size equal to 1.5 mm and 2.5 mm in Fig. 6.8.

In general, the matched beam provides the best condition in terms of beam losses and beam quality through the cyclotron axial bore.

The beam with half-size equal to 2 mm in Fig. 6.8 is matched with respect to the optical properties of the CS axial bore. Indeed, beam envelope oscillations are not visible along the beam path from the median plane up to the yoke entrance. Actually, very small envelope oscillations are present when 3D magnetic field data are considered in the calculations, as one can see in Fig. 6.9 (a) where the beam envelope along a small portion of the CS injection line close to the median plane is shown. However, the oscillations are so small that can be considered negligible, especially if compared to the other simulated beams. The envelopes of two mismatched beams are also shown in Fig. 6.9 for comparison. Consequently, this beam has been assumed in the beam dynamics study as the good beam matched with respect to the optical properties of the CS axial bore.

Its features, at 1370 mm from the median plane on the vertical CS axis, are listed in Table 6.4. This position, very close to the CS bore entrance, has been considered as the starting position in all the simulations present in this chapter, that include the beam motion through the axial bore of the INFN-LNS Superconducting Cyclotron. Figure 6.10 shows the spatial distribution and the $x - x'$ phase space of the matched beam at the chosen starting position.

6.3.2 Phase dispersion in the yoke bore and spiral inflector

Several processes occur during beam transit through the yoke bore of a cyclotron, before ions enter the accelerator, and axial magnetic field
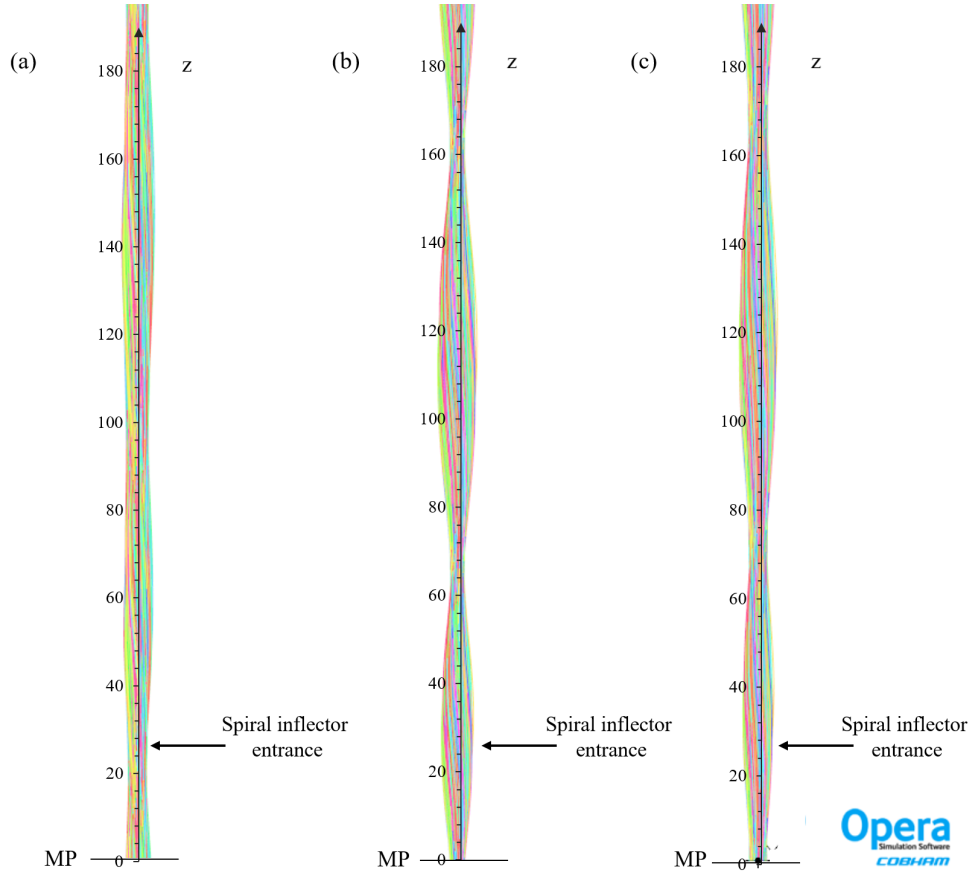
Figure 6.9: Three beam envelopes along a small portion of the CS injection line close to the median plane (MP): beam matched (a) and non-matched ((b) and (c)) with the optical properties of the CS axial bore.

and spiral inflector play a key role in determining the injected beam properties.

The greatest contribution to the coupling between the two transverse phase spaces is usually given by the spiral inflector. Indeed, an uncorrelated input beam will be correlated when it exits the electrostatic device. The result of this correlation is an increase of beam emittance.

Moreover, the coupling between the transversal and longitudinal phase spaces gives rise to a time dispersion and, consequently, to a particle RF phase width broadening. This process is due to particles at the edge of the beam that experience a transit time factor which is considerably

Beam half-size	13.4 mm
Beam divergence	26.3 mrad
Correlation	-0.87
Geometrical emittance	$175\pi \cdot$ mm-mrad
Normalized emittance	$1\pi \cdot$ mm-mrad
Starting beam tracking position	Position on the vertical axis at 1370 mm from the MP

Table 6.4: Transverse phase space 1370 mm above the median plane matched with the optical properties of LNS cyclotron axial bore. A water-bag distribution of particles has been assumed. The beam has rotational symmetry with respect to the beam axis.
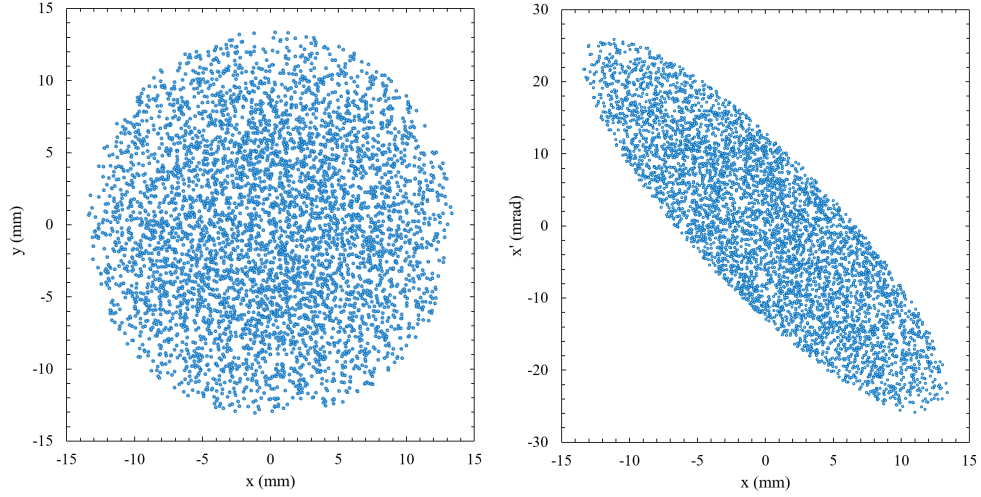

Figure 6.10: Beam matched with respect to the optical properties of the CS axial bore. On the left, spatial distribution $x - y$. On the right, the $x - x'$ phase space (it is the same for the $y - y'$ phase space).

different from the one of the reference orbit, due to the different orbit lengths. In general, it is dominant in the spiral inflector but it occurs also in the cyclotron yoke bore, due to the greater helical orbit length of the ions with respect to the reference particle moving on the vertical axis.

In this thesis work, the process of particle RF phase dispersion in the CS yoke bore has been studied simulating the beam particles motion from the axial bore entrance up to the spiral inflector exit.

The large emittance of the beam injected in the CS determines a large particle RF phase width broadening in the CS axial bore. Indeed, the greater the emittance the greater the RF phase dispersion in the injection line because the transit time factor that experience particles at the beam edge will be different from the reference one. The large beam size creates also different orbit lengths inside the spiral inflector.

The spiral inflector is electrostatic, bending the less energetic ions more than, and the more energetic ions less than the reference particle.

Therefore, this implies different ion orbit lengths inside the inflector and, consequently, a kinetic energy-time correlation is established.

In order to better understand the influence of beam emittance on the time dispersion process, two different simulations have been performed, assuming in each one to inject all the beam particles in the axial cyclotron bore at the same value of RF phase, equal to 321°. The mono energetic matched beam was compared with a beam with small emittance, one hundred times lower. In order to know the ϕ-distribution at the spiral inflector exit, the intersection of the beam particles with a patch placed at the exit of the device has been simulated.

A statistical analysis of the data have been carried out and the results are shown in Fig. 6.11.

The data has been fitted with a Gaussian function, defined as follows:

$$N_\phi = \alpha \cdot e^{-\frac{1}{2}(\frac{\phi-\bar{\phi}}{\sigma})^2} \tag{6.3.7}$$

where N_ϕ is the number of the particles, α is equal to $\frac{1}{\sigma\sqrt{2\pi}}$, σ is the standard deviation and $\bar{\phi}$ is the mean value of the ϕ-distribution at the inflector exit.

Also root-mean-square deviation calculations have been performed.

$\sigma_{r.m.s.}$ at the exit of the spiral inflector has been calculated by means of
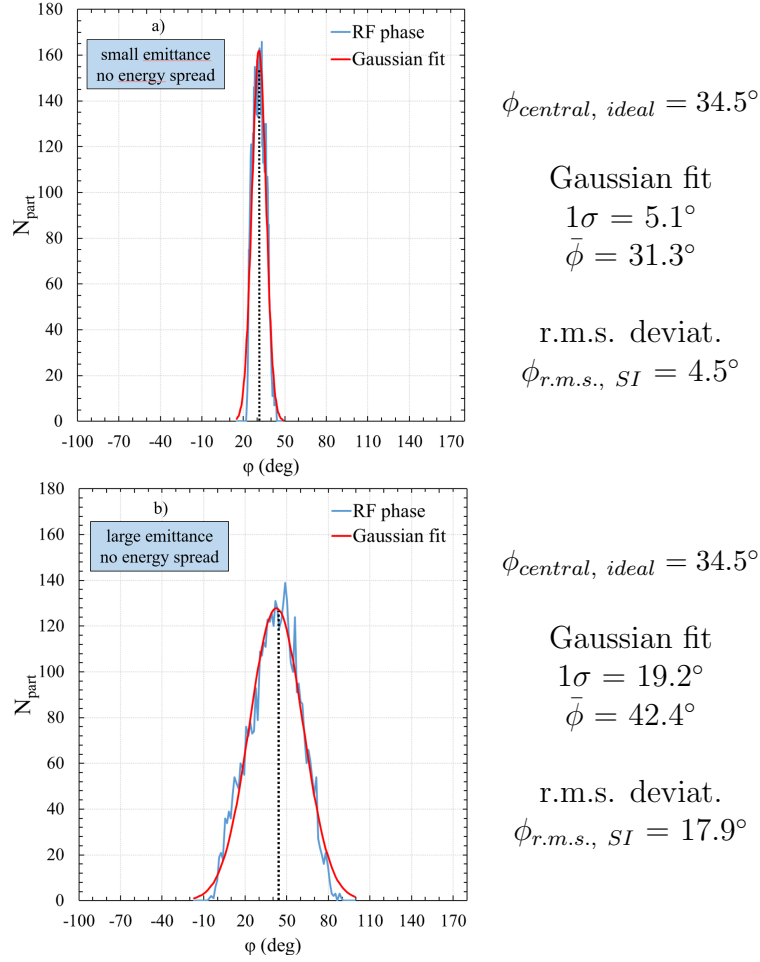
140

Figure 6.11: RF phase distribution at the SI exit in two different cases: (a) injection of a small emittance, (b) injection of a big emittance. The initial RF phase is equal for all the particles and in the two cases.

the following formula, according to its definition:

$$\sigma_{r.m.s., \, SI} = \sqrt{\frac{\sum_{N_{part}} (\phi - \bar{\phi})^2}{N_{part}}} \tag{6.3.8}$$

with $\bar{\phi}$ the mean value of the particle RF phase distribution at the spiral inflector exit and N_{part} the number of the beam particles.

The comparison between the two plots confirms that the beam emittance plays an important role in the RF phase dispersion process. The particle RF phase distribution at the inflector exit is greater when a large

141

emittance of the beam is injected in the CS axial bore.

The root-mean-square analysis shows that the r.m.s. deviation in the case of small injected emittance is only 4.5°, about a factor four less than the case of the injected large emittance. Also the comparison between the two Gaussian fits highlights the strong dependence of the beam longitudinal motion in the CS axial bore and spiral inflector on the emittance. An interesting result that emerges from the comparison of the two Gaussian fits is that the centroid of the RF phase distributions are not coincident to each other. In addition, their values are different from the value $\phi_{central,\ ideal}$. This value is the corresponding phase at the spiral inflector exit of the initial phase, having considered the RF phase advance during the ion motion from the cyclotron bore entrance up to spiral inflector exit. These results can be explained considering that, when a small beam emittance is injected in the CS axial bore, the orbit lengths of the ions at the beam edge differ only slightly from the each others and from the reference one moving along the vertical CS axis. The same occurs also in the spiral inflector. This implies that the particle RF phases are distributed in a narrow interval around a value very close to the value $\phi_{central,\ ideal}$. On the contrary, in the case of a large emittance, particles at the beam edge will take a different time to move in the CS axial bore and spiral inflector with respect to the reference beam particle.

Consequently, a broadening of the initial RF phase interval is observed. In conclusion, the injection in the CS of a great beam emittance implies a process of RF phase width broadening in the CS axial bore.

The width of particle RF phases injected in the CS central region will be higher than that injected in the CS axial bore. This aspect can not be negligible in the case of the CS, due its influence on the beam transmission in the central region.

6.4 Evaluation of the injection efficiency

Once the beam is injected onto the cyclotron median plane by means of the spiral inflector, the ions are accelerated in the central region, the complicated 3D accelerating structure occupying the inner part of the cyclotron. The design of the central region of the LNS cyclotron is complicated because the magnetic field is very high (compared to the normal cyclotrons), which makes the compact central region, leaving very little room for the spiral inflector and the accelerating electrodes.

A good design of the central region requires that: i) the beam moves on well-centred accelerated orbits, ii) the beam is vertical focused (it is important because the flutter goes quickly to zero in the central region) and iii) the losses in the central region are as small as possible in order to provide high transmission.

A study has been carried out in order to evaluate the injection efficiency supposing to inject the beam along the vertical CS axis. This is important in order to understand where the losses are localized in the cyclotron centre and how the ion transmission could be improved in view of the LNS cyclotron upgrade. Indeed, as already reported in Chapter 1, the injection efficiency has to be improved for obtaining the expected high beam power extracted by stripping from the CS.

The initial conditions assumed in the study are listed in Table 6.5.

We simulated the matched beam starting its motion at the entrance of the CS axial bore. An uniform distribution of particle RF phases on a interval of 30° was assumed at the starting tracking position. Furthermore, we considered a value of the beam energy spread equal to ±0.6%. Figure 6.12 shows the beam in the central region. We assumed to inject in the LNS cyclotron a sample of 10000 particles. For a better visualization of the particle losses, only the 10% of the injected particles are shown in the figure.

Details on the losses on each component of the central region, included

$[\phi_{min} - \phi_{max}]$	[306°-336°] (included $h = 2$)
$\phi_{central}$	321° (included $h = 2$)
ϕ-distribution	Uniform ($\phi_{r.m.s., \ init} = 8.7°$)
Beam	See Table 6.4
E_{inj}	240 keV
ΔE_{inj}	$\pm 0.6\% \ E_{inj}$
ΔE_{inj}-distribution	Uniform
N_{part}	10000

Table 6.5: Initial conditions assumed in the study of injection efficiency.

the spiral inflector, are listed in Table 6.6. The nomenclature used in the table is the same of the one reported in Fig. 6.13.

The total percentage of particles lost in the CS injection system is about 70.3%, corresponding to an injection efficiency of 29.7%.
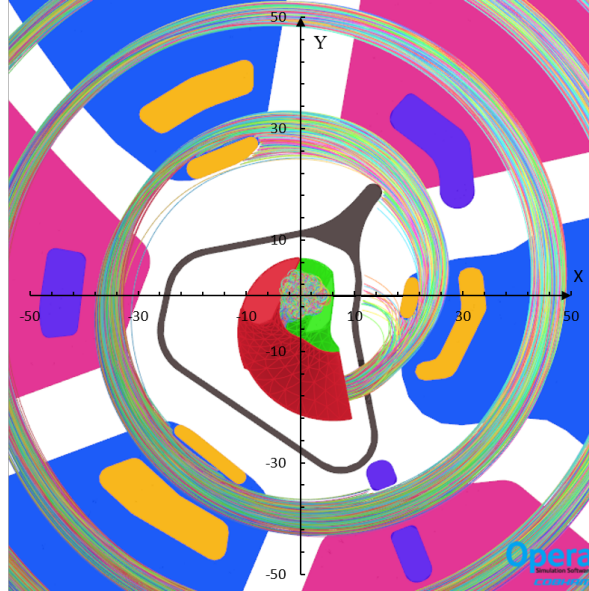

Figure 6.12: Beam in the CS central region. For a better visualization of the particle losses, only the 10% of the injected particles are shown.
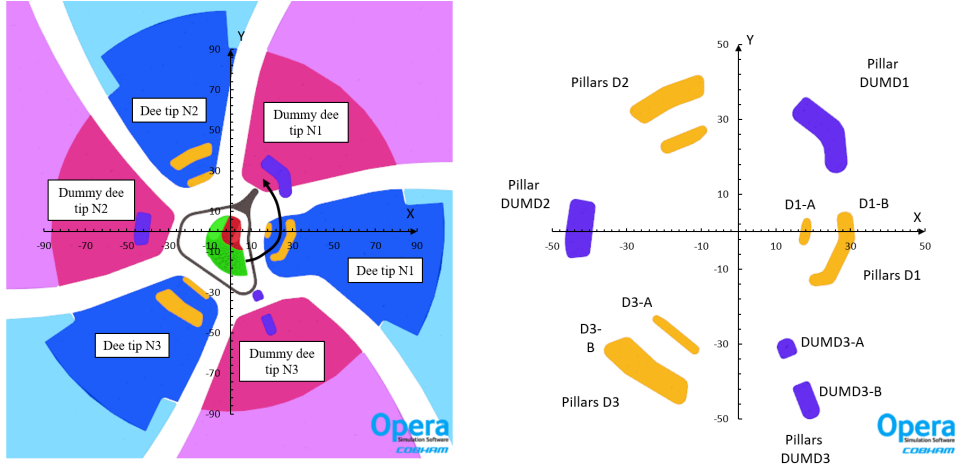
Figure 6.13: On the left, the Opera-3d model of the CS existing central region. All the components are visible except the collimator placed before the spiral inflector entrance. On the right, the pillars present in the central region are shown. The orange ones are at the same potential of the dee tips, the other ones are grounded electrodes.

The low injection efficiency is mainly due to the radial hits of the ions with the pillars in the central region, especially with the pillars D1 and D2. Indeed, the losses on these two elements represent about the 63% of the total losses in the CS injection system. Hits of particles with the spiral inflector and collimator are the 13% of the total losses. Losses on the dee and dummy dee tips are vertical due to the hits of particles with the accelerating electrodes that stay symmetrically above and below the median plane. However, their contribution to the total losses is only the 2.5%. Since this calculation has been done supposing to inject particles with initial RF phases within an interval of 30°, the injection efficiency in the case of an injected DC beam coming out from the ion source is:

$$\epsilon_{inj} = 29.7\% \cdot \frac{30°}{360°} \simeq 2.5\% \qquad (6.4.1)$$

In the event that the buncher in the injection line has a buncher efficiency of 50%, the injection efficiency stays around 15%.

It is interesting to observe that the injection efficiency shows only a slight

145

ϵ_{inj} (%)	29.7
Electrode	Losses (%)
Collimator	5.6
Spiral inflector	7.5
Housing	6.9
Dee tip N1	0.7
Pillars D1	21.6
Pillar DUMD1	/
Dee tip N2	1
Pillars D2	22.5
Pillar DUMD2	/
Dee tip N3	0.8
Pillars D3	2.3
Pillars DUMD3	1.3
Dummy dee tips	0.1

Table 6.6: Injection efficiency and percentage of lost particles on each components of the CS central region, included the spiral inflector. It refers to the simulation performed assuming the initial conditions reported in Table 6.5. The nomenclature used in the table is the same of the one reported in Fig. 6.13

.

dependence on the amplitude of the initial RF phase interval injected in the CS axial bore. The results on the injection efficiency shown in Table 6.6 are compared in Table 6.7 with the ones obtained assuming to inject in the CS axial bore, particles with RF phases inside an interval of 10° (centred at the same value $\phi_{central}$) and maintaining unchanged all the other initial conditions. This confirms what already reported in the previous section i.e. the injected beam emittance plays an important role

	Phase width 30°	Phase width 10°
ϵ_{inj} (%)	29.67	31.2
Electrode	Losses (%)	
Collimator	5.6	5.8
Spiral inflector	7.5	7.7
Housing	6.9	6
Dee tip N1	0.7	0.9
Pillars D1	21.6	20.5
Pillar DUMD1	/	/
Dee tip N2	1	1.1
Pillars D2	22.5	22.4
Pillar DUMD2	/	/
Dee tip N3	0.8	0.8
Pillars D3	2.3	2.2
Pillars DUMD3	1.3	1.2
Dummy dee tips	0.1	0.2

Table 6.7: Injection efficiency and percentage of lost particles on each elements of the CS central region, included the spiral inflector. The first column refers to the simulation performed assuming the initial conditions reported in Table 6.5. The other one refers to the same initial conditions but to a RF phase width of 10°. The nomenclature used in the table is the same of the one reported in Fig. 6.13

.

in determining the features of the accelerated beam after its injection in the cyclotron. The simulation results can be explained as a consequence of the large injected emittance that determines a RF phase distribution at the inflector exit, which is almost equal in the two cases. The results of the Gaussian fit and r.m.s. calculations performed on the RF phase

distribution at the exit of the spiral inflector in both cases are listed in Table 6.8.

Phase width	30°	10°
Gaussian fit		
σ (°)	33.6	32.8
$\bar{\phi}$ (°)	44	43
r.m.s. deviation		
$\phi_{r.m.s.}$(°)	31.1	29.8

Table 6.8: Gaussian fit parameters and r.m.s. deviations of the RF phase distribution at the exit of the spiral inflector when 30° and 10° particle RF phase widths are injected in the CS axial bore respectively.

6.5   Beam energy spread at the extraction

The extraction by stripping of high beam power with, at the same time, high energy resolution is the key-point of the CS upgrade project. Beam tracking simulations from the axial bore entrance, through the present spiral inflector up to the extraction system, have been carried out for the evaluation of the beam energy spread at the extraction.
The investigation of the factors that influence the energy spread of the extracted beam is essential for understanding what is the minimum value attainable by the CS and if and how it can be improved.
In all the simulations present in this section, the beam energy distribution has been evaluated at the beginning of the first electrostatic deflector of the CS, that is within the cyclotron area where the stripper foil system is expected to be placed.
For a beam extracted by stripping, the energy spread is determined by the horizontal emittance and energy gain per turn, as reported in Ref.
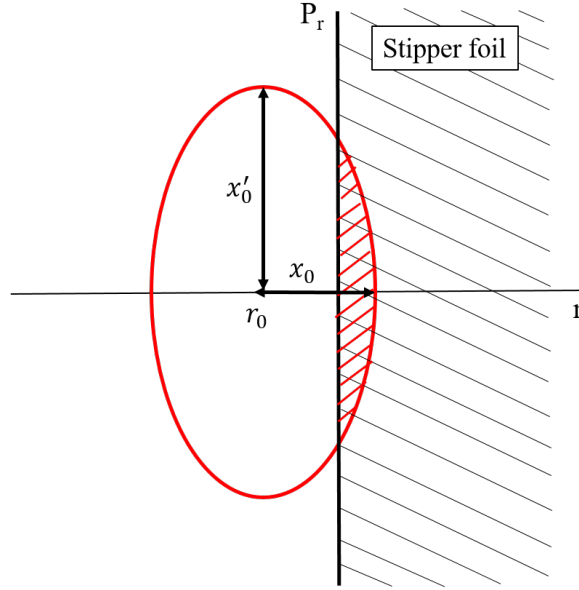
Figure 6.14: Radial phase space area reaching the stripper foil.

[85].

We consider a radial phase space area at position r_0 in the cyclotron, relative to the kinetic energy E_0 and we assume that the beam is well matched with respect to the eigen-ellipse and well centred. After many turns in the cyclotron, this is usually the case. We suppose that this area just touches the stripper foil, as shown in Fig. 6.14. Particles lying in the part of the phase space area that overlaps with the foil are stripped and extracted from the cyclotron. Other particles have to make more turns to reach the stripper and gain extra energy. During each extra turn, the eigen-ellipse is accelerated and shifted radially, according to Eq. 3.1.1. The beam energy spread is related to the horizontal beam width at the stripper foil. The beam width is individuated as the distance between two positions of the horizontal phase space ellipse with respect to the position of the stripper foil: the former is when the beam starts to be extracted and the upper radial extremity of the emittance touches the stripper foil from below; the latter is when all the beam has just been

149

extracted and the lower radial extremity of the emittance touches the stripper foil from below above. The following formula holds:

$$\pm \frac{\Delta E}{E_0} = \pm 2 \frac{x_0}{r_0} \qquad (6.5.1)$$

where ΔE is the beam energy spread at the stripper foil, E_0 is the extraction energy, r_0 is the extraction radius and x_0 is one half the radial width of the beam. Assuming that the beam is well matched with respect to the magnetic focusing structure, the beam emittance ϵ and the half the beam radial width x_0 relate as follows:

$$\epsilon = \pi \ x_0 \ x_0^{'} = \pi \ \frac{\nu_r x_0^2}{r_0} \qquad (6.5.2)$$

where ν_r is the radial betatron frequency and x_0' is one half the beam divergence at the extraction radius r_0.

Combining Eqs. 6.5.1 and 6.5.2, the contribution of the emittance to the energy spread is obtained:

$$\Delta E_{emit} = \pm \sqrt{\frac{4E_0^2 \epsilon}{r_0 \pi \nu_r}} \qquad (6.5.3)$$

However, there exists also a contribution due to the energy gain per turn. This can be seen by considering the case where the circulating emittance is very small (let's assume zero). In this case, the full energy spread in the extracted beam will be equal to $\Delta E_{acc} = \frac{\Delta E_t}{2}$, where ΔE_t is the energy gain per turn. Both contributions can be added in quadrature. Therefore, the final expression for the beam energy spread is the following:

$$\Delta E_{tot} = \sqrt{\Delta E_{emit}^2 + \Delta E_{acc}^2} = \sqrt{\frac{4E_0^2 \epsilon}{r_0 \pi \nu_r} + \frac{\Delta E_t^2}{4}} \qquad (6.5.4)$$

From this equation, it is possible to calculate the energy resolution:

$$\frac{\Delta E_{tot}}{E_0} = \sqrt{\left(\frac{\Delta E_{emit}}{E_0}\right)^2 + \left(\frac{\Delta E_{acc}}{E_0}\right)^2} = \sqrt{\frac{4\epsilon}{r_0 \pi \nu_r} + \frac{\Delta E_t^2}{4E_0^2}} \qquad (6.5.5)$$

We demonstrated that, when the circulating emittance in the cyclotron is large, the energy spread at the extraction, and consequently the energy resolution, is mainly determined by the horizontal beam emittance. According to Eq. 6.5.4, the contribution to the energy spread due to the horizontal beam emittance is given by:

$$\Delta E_{emit} = \sqrt{\Delta E_{tot}^2 - \Delta E_{acc}^2} \qquad (6.5.6)$$

In terms of energy resolution, we have:

$$\frac{\Delta E_{emit}}{E_0} = \sqrt{\left(\frac{\Delta E_{tot}}{E_0}\right)^2 - \left(\frac{\Delta E_{acc}}{E_0}\right)^2} \qquad (6.5.7)$$

ΔE_{emit} can be estimated only if the contribution to the energy spread due to the energy gain per turn is known. To perform such an evaluation, a pencil beam in the central region has been started at 120 mm from the CS centre in order to take into account only the acceleration process. A selection of 10° RF phase width has been done at the starting tracking position and the beam has been accelerated in the cyclotron up to the extraction system. In order to evaluate ΔE_{tot} in Eq. 6.5.6, the same particle RF range has been uniformly assigned also to the particles of a 1π mm-mrad normalized emittance beam, supposed well matched with respect to the magnetic focusing properties of the CS in the chosen tracking starting position. For sake of simplicity, the same value of 4 r.m.s. normalized emittance in both horizontal and vertical phase spaces has been assumed. A water-bag like distribution of particles in the beam has been simulated.

Figures 6.15 a) and b) show the energy distribution at the extraction obtained in the case of the acceleration of the pencil beam and the beam with big emittance respectively. In the same figure also the value of the relative energy spread, obtained from the Gaussian fit results, is reported for the two cases. According to Eq. 6.5.7, the relative energy spread due to the horizontal beam emittance only is 0.32%. Two interesting results
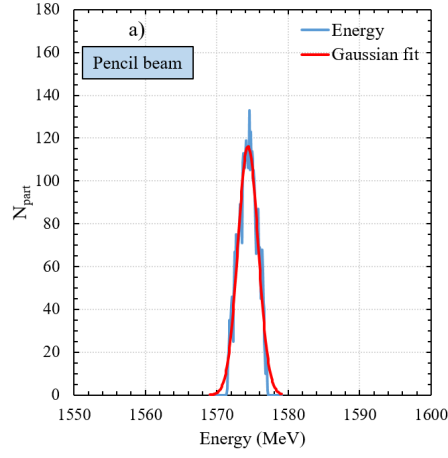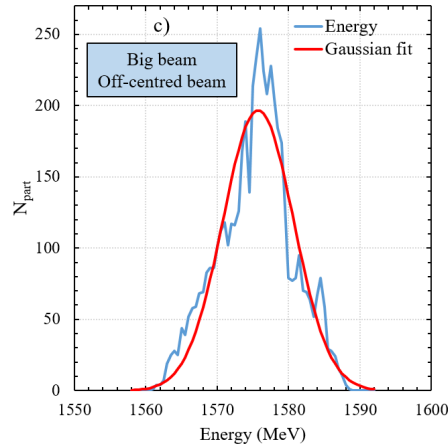
Gaussian fit
$1\sigma = 1.42$ MeV
$E_0 = 1574.38$ MeV
FWHM $= 3.34$ MeV

$\frac{E_{tot}}{E_0} = 0.21\%$
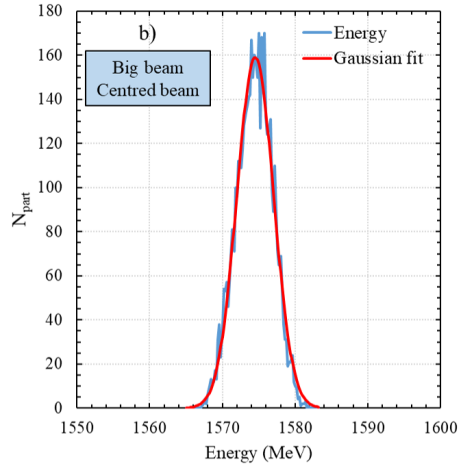
Gaussian fit
$1\sigma = 2.58$ MeV
$E_0 = 1574.3$ MeV
FWHM $= 6.08$ MeV

$\frac{E_{tot}}{E_0} = 0.39\%$

Gaussian fit
$1\sigma = 4.96$ MeV
$E_0 = 1575.75$ MeV
FWHM $= 11.68$ MeV

$\frac{E_{tot}}{E_0} = 0.74\%$

Figure 6.15: Beam energy distribution in three different cases: (a) acceleration of a pencil beam in the CS, (b) acceleration of a well centered big emittance. (c) acceleration of a big emittance with a initial offset of 2 mm. The initial RF phase interval is equal 10° in all the cases.

emerge from the comparison between the calculated energy spread values. The first one is that the beam energy spread at the extraction is mainly due to the horizontal beam emittance and the energy gain per turn contributes only partially, as above-mentioned. The second one is that the relative energy spread at the extraction obtained accelerating a pencil beam, and therefore related only to the acceleration process, is about twice the relative energy spread required by the NUMEN experiment. This value can be considered as an inferior limit of the energy spread obtainable from the CS.

Moreover, if the beam moves in the cyclotron on accelerated orbits not well centred with respect to the cyclotron centre, the horizontal emittance increase during acceleration and an additional contribution is expected to the energy spread at the extraction. In order to demonstrate this, we supposed to inject the big emittance in the same position in the CS central region with an initial offset of 2 mm. The energy distribution at the extraction obtained in this situation is shown in Fig. 6.15 c).

In this case the contribution of the emittance to the energy resolution is 0.71% , a value more than twice than that obtained in the well centred big emittance case. Therefore, for achieving a small energy spread of the extracted beam, it is important to accelerate a beam with horizontal emittance as small as possible exiting from the central region and well centred on an equilibrium orbit.

A more realistic beam tracking requires the beam energy distribution at the extraction to be evaluated supposing a matched beam (see Table 6.4) injected from the axial bore entrance. In the study reported hereinafter, also the process of RF phase selection in the central region has been investigated as a possible solution to decrease the energy spread at the extraction.

Usually, a phase selection system is used to improve the poor beam quality of the extracted beam, in particular to reduce the energy spread and

the pulse length. In cyclotrons, the traditional method of removing undesired RF phases from the beam consists in the use of one o more slits placed at certain radii and azimuthal angles in the accelerator.

The slits are placed in the centre of the cyclotron where the beam energy is low in order to reduce the possible activation of the cyclotron components.

In the simulation study, we used a trick in the AOC tracking model in order to take into account the effects of the RF phase selection without the needs to design the phase slits in Opera-3d. First, the beam particles were stopped in the central region at 120 mm from the CS centre and their phase space coordinates were taken. Later, the particles outside of the $10°$ RF phase width around the centroid were removed from the beam and were re-started at the same point in the cyclotron. Also the harmonics coils for providing horizontal beam centring have been not simulated in Opera-3d because another trick in AOC has been used. The position of beam stop in the CS central region, coincident with the new starting position for the beam tracking in the cyclotron, was re-set by adjusting the position and the momentum direction of the beam centroid on the median plane until a good centring of the accelerated particle orbit in the LNS cyclotron was found.

The beam energy distribution at the extraction obtained supposing to inject the matched beam at the bore entrance with $10°$ RF phase width is shown in Fig. 6.16. The first plot refer to the simulation performed without RF phase selection in the central region, the latter has been obtained including this process in the simulation. Also in these cases a Gaussian fit has been performed and the energy spread has been obtained starting from the FWHM of the energy distribution. The relative energy spread is 0.6% in the first case and this value becomes 0.5% when a RF selection process is performed in the central region. Both values are higher than the NUMEN requirement. The comparison between the plots shows that
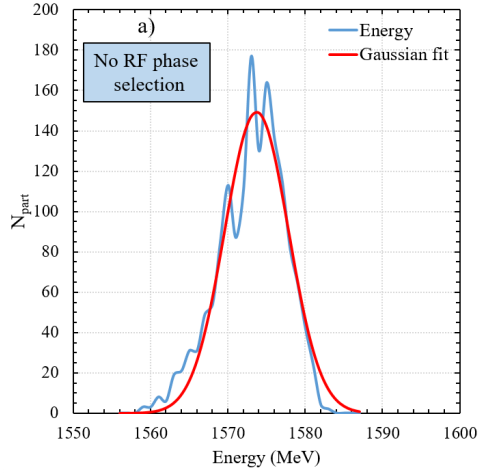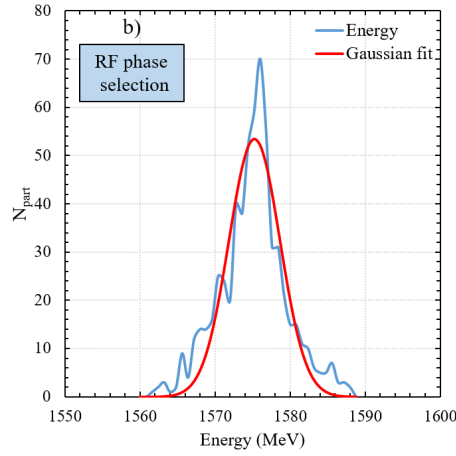
Figure 6.16: Beam energy distribution at the extraction supposing to inject the matched beam at the CS axial bore entrance and to accelerate it up to the extraction system. In the case b) a 10° RF phase selection is simulated in the central region. The initial RF phase interval is equal in all the cases.

the RF phase selection allows to reduce the energy spread at the extraction, and consequently the energy resolution, but not so significantly. Therefore, the simulated RF phase selection process increases the beam losses (almost 40% of the injected beam in the central region) without the possibility to allow to achieve the energy resolution value required by the NUMEN experiment.

This can be considered as a further confirmation that the beam emittance plays an important role in determining the beam energy spread at the extraction.

6.6   Evaluation of the total efficiency

The simulation results presented in the previous section shows that the CS is not able to deliver a beam with the energy resolution required by NUMEN. As a consequence, a beam energy selection is needed outside the LNS cyclotron in order to reduce the beam energy spread. Obviously, this process implies a power reduction of the extracted beam to be included in the evaluation of the overall efficiency as a further source of beam losses. However, the new fragment separator will be able to remove beam power up to 2 kW, then limiting the maximum beam power that can be delivered to the NUMEN experiment.

The total efficiency ϵ_{tot} is calculated as the product of the efficiency of all the processes that occur from the injection into the CS cyclotron up to the energy selection, according to the following formula:

$$\epsilon_{tot} = \epsilon_{inj} \cdot \epsilon_{RFS} \cdot \epsilon_{ext} \cdot \epsilon_{ES} \tag{6.6.1}$$

where ϵ_{inj} is the injection efficiency, ϵ_{RFS} is the RF phase selection (RFS) efficiency, ϵ_{ext} is the extraction efficiency and ϵ_{ES} is the energy selection (ES) efficiency. Therefore, ϵ_{tot} is determined by the losses in the spiral inflector and central region, the losses due to the RF phase selection

process occurring in the central region at 120 mm from the CS centre and the losses due the energy selection process, assuming an extraction efficiency of 100%.

Hereinafter, we report the calculation of the total efficiency carried out considering the same starting conditions already used for the study of the injection efficiency (see Table **??**).

According to the results obtained in Section 6.4, the transmission in the central region is equal to 29.7%. This means that about the 70% of the particles injected in the CS axial bore are lost in the spiral inflector or in the central region. Considering a DC beam coming out from the ion source, this value corresponds to an injection efficiency of 15%, in the event that the buncher in the injection line is able to guarantee a buncher efficiency of 50% inside a working RF range of about 30° [86]. The RF phase selection efficiency ϵ_{RFS} is 40.2%, in the event that only a 10° RF phase width around the centroid phase is accelerated from the central region up to the extraction. Since the study of the energy selection system is ongoing at LNS laboratories and beyond the scopes of this thesis work, the system has not been simulated and the value of the efficiency of the energy selection process has been extracted from the energy distribution of the beam at the extraction.

In order to estimate the energy selection process efficiency, we counted the number of ions contained in 0.1% with respect to the energy where the distribution is maximum. The ϵ_{ES} is 18.3%.

Considering the values of ϵ_{inj}, ϵ_{RFS} and ϵ_{ES}, the total efficiency stays around 1.1%. If the RF phase selection process does not occur in the central region, the total efficiency increases achieving a value close to 2.7%. This value is below the NUMEN requirements. However, it should be considered that it has been obtained under conservative hypothesis concerning the injected beam features and the energy spread. In any case, it can not be compared to the 15% assumed in Table 1.1 because in

the latter the RF phase and energy selection processes are not included. Even if pessimistic, the result obtained gives a clear indication that the improvement of the injection efficiency is needed in order to increase the total efficiency, even if it continues to be present a constraint on the minimum beam energy spread obtainable at the extraction, given mainly by the large beam injected emittance into the CS.

6.7 Improvement of the injection efficiency

As already described in Section 6.4, the spiral inflector and central region occupy a little room in the CS and, due to the presence of the pillars intercepting the median plane, a small clearance is reserved to the ions before their escape from the central region.

The radial losses on the pillars, especially on D1 and D2, are the principal causes of the low ion transmission in the central region, as reported in Table 6.6. In order to maximize the total transmission from the injection into the CS up to the extraction system, a high injection efficiency in the central region, where the acceleration process starts, is required.

In this section, the study of the improvement of the CS central region, resulting in better injection efficiency, is presented.

6.7.1 Increase of the dee voltage

As a first step, we investigated the effect on the injection efficiency of voltages higher than the nominal one applied on the present electrodes of the CS accelerating structure. Three different dee voltage values, equal to 90, 95 and 100 kV respectively, have been considered in the simulations and the results about the injection efficiency have been compared with the nominal dee voltage case (V_{dee}=86 kV).

The initial conditions assumed for the beam tracking are the same of the total efficiency calculations and are listed in Table **??**. Also in this

case, we considered a matched beam (see Section 6.3), with a normalized emittance equal to 1π mm-mrad, started the motion at the entrance of the cyclotron axial bore.

An uniform distribution of the particle RF phases on a interval of 30° was assumed at the starting position. For each dee voltage, the optimum RF phase range have been chosen in order to optimize both the horizontal orbit centring and the vertical motion of the beam reference particle. Table 6.9 contains the RF phase range chosen for each dee voltage. Furthermore, a sample of 10000 particles with an energy spread $\Delta E/E_{inj}$ equal to $\pm0.6\%$ has been included in the simulations.

The injection efficiency in percentage ϵ_{inj} as a function of the dee voltage

Dee-voltage (kV)	RF phases (deg)
86	[306-336]
90	[298-328]
95	[297-327]
100	[292-322]

Table 6.9: Dee voltage values and beam RF phase intervals considered in the study of the injection efficiency improvement. The total RF width is 30° in all four cases.

is listed in Table 6.10. The percentage of lost particles on each element of the central region are also reported. The nomenclature for the electrodes used in the table is the same of that reported in Fig. 6.13.

The injection efficiency increases from 29.69 % to 41.09 % when the dee voltage rises, as reported in Table 6.10.

The improvement of the transmission in the central region is mainly due to the decrease of the radial losses on the pillars D1 and D2. Indeed, the use of dee voltages higher than the nominal one has the effect to help a higher number of ions to move away from the above-mentioned electrodes reducing the hits. Only a fraction of these ions are lost on

159

	Dee-voltage 86 kV	Dee-voltage 90 kV	Dee-voltage 95 kV	Dee-voltage 100 kV
ϵ_{inj} (%)	29.7	39.2	43.5	41.1

Electrode	Losses (%)	Losses (%)	Losses (%)	Losses (%)
Collimator	5.6	5.6	5.6	5.6
Spiral inflector	7.5	7.5	7.5	7.6
Housing	6.9	4.2	3.2	2.2
Dee tip N1	0.7	1.3	1.6	1.5
Pillars D1	21.6	17.8	14	11.2
Pillar DUMD1	/	0.1	0.1	1.2
Dee tip N2	1	1.6	2.3	2.5
Pillars D2	22.5	16.7	11.2	8.8
Pillar DUMD2	/	/	0.1	4.6
Dee tip N3	0.8	1.4	1.8	1.8
Pillars D3	2.3	2.6	5.9	6.1
Pillars DUMD3	1.3	1.7	3	5.6
Dummy dee tips	0.1	0.3	0.2	0.4

Table 6.10: Injection efficiency ϵ_{inj} in percentage as function of the dee voltage. The initial number of particles is 10000 for all cases. The percentages of lost particles on each element of the central region are also listed. The nomenclature used in the table is the same of that reported in Fig. 6.13 .

the others pillars or vertically on the dee tips, the other ones are able to escape from the central region. This effect becomes greater and greater as the dee voltage is increased.

For a better understanding of the process of particle loss, Fig. 6.17 shows the beam in the central region when the voltage applied on the dees is 86 kV and 100 kV respectively. In Fig. 6.18 a zoom in the region close

to the pillars D2 and DUMD2 is present. As one can see, when the dee voltage applied is the nominal one, more particles hit the pillar D2 with respect to the 100 kV dee voltage case, whereas radial losses on the pillar DUMD2 are absent.

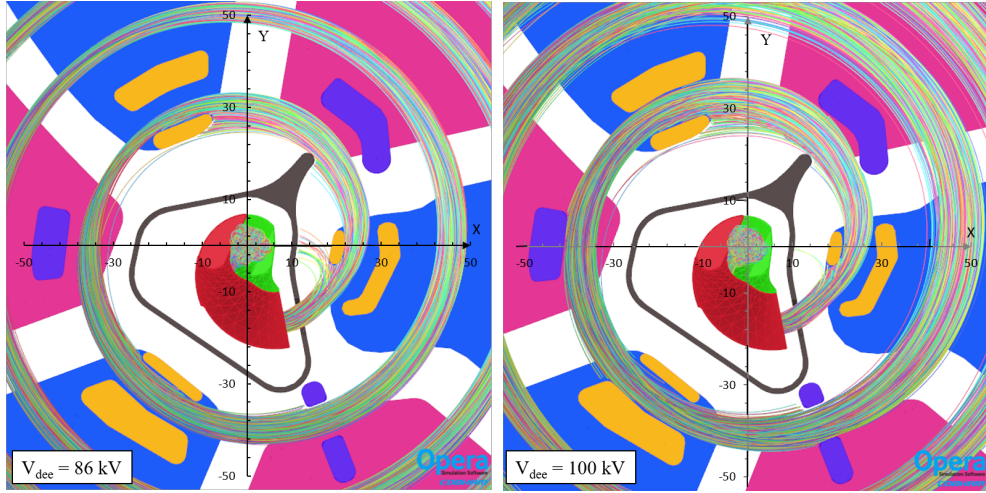Obviously, losses on the collimator and the spiral inflector electrodes

Figure 6.17: Beam particles in the central region, when the voltage applied to the dees is equal to 86 kV (on the left) and 100 kV (on the right). For a better visualization of the particle losses, only the 10% of the injected particles are shown.

are independent of the voltage applied on the dees and their contribution to the injection efficiency are the same in all the cases within statistical errors, as reported in Table 6.10.

6.7.2 Improvement of the central region design

The improvement of the injection efficiency by the use of dee voltages higher than nominal one was the base for some further simulations to investigate the increase of the ion transmission in the central region. Considering the two dee voltage values able to guarantee the higher injection efficiency, i.e 95 kV and 100 kV (see Table 6.10), the existing CS central region design has been slightly modified for further reduction of
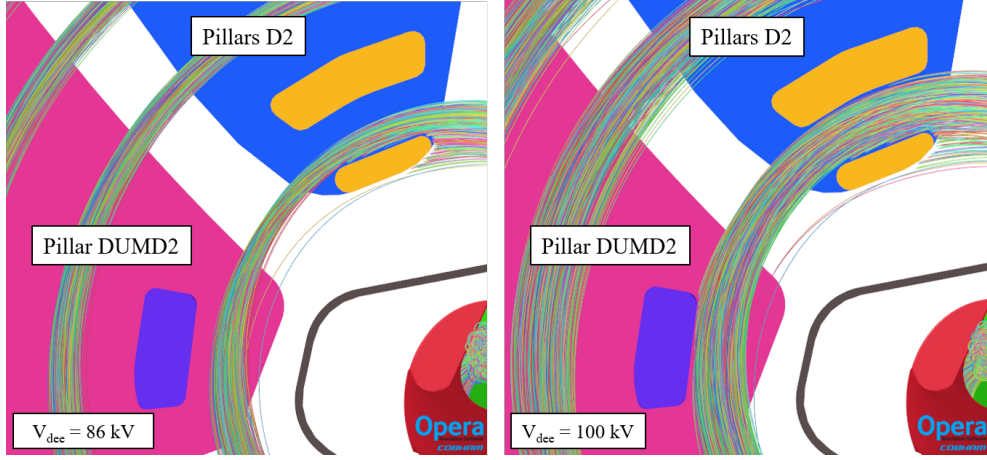
Figure 6.18: Beam particles crossing the dee tip N2 and the dummy dee tip N2, when the dee voltage is equal to 86 kV (on the left) and 100 kV (on the right). For a better visualization of the particle losses, only the 10 % of the injected particles are shown.

the radial hits of the ions with the electrodes intersecting the median plane.

In order to create a larger clearance reserved to the beam in the first turn in the CS centre, the pillars have been moved at higher or lower radius with respect to their present position (shift of 1 or 2 mm).

We compared the results about the injection efficiency for the existing design of the CS central region and for the two new modified geometry, obtained changing the pillar positions.

From now on, model I will be the name used to indicate the existing geometry of the CS central region, whereas the two modified geometries will be named model II and model III respectively.

Figure 6.19 shows the differences between the three models of the CS central region. For a better understanding of the changes, only the elements, which have been moved or cut, are shown. Each colour refers to a different model. On the left the differences between model I and II are shown and on the right the ones relative to model II and III. As one can see, model III differs from the second one only for the change in position

162

of the pillars D2-A and D3-A.

Due to the impossibility to move the pillar DUMD3-A at inner radius because of the small distance from the housing, the section of this pillar has been internally cut of 2 mm to increase the distance from the pillar DUMD3-B.

Furthermore, we decided to maintain the present position of the pillars D1, placed on the first dee tip after the spiral inflector exit, to avoid drastic changes of the beam dynamics in the cyclotron centre with respect to the present one. Indeed, the first accelerating gaps, crossed by the particles when their energy is very low, play an important role in the definition of the beam properties in the central region, especially in terms of vertical focusing and horizontal centring.

More details about the shift in position of the pillars in models II and III, with respect to the existing one, are present in Table 6.11.

Table 6.12 contains the results of the injection efficiency calculations for
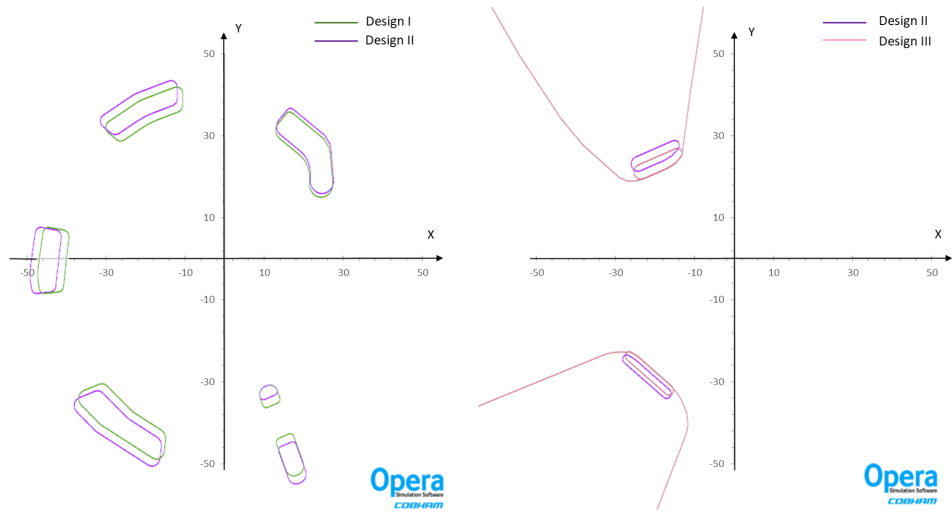

Figure 6.19: Differences between the three models of the CS central region. For a better understanding of the changes, only the electrodes, which have moved or cut, are shown. Each colour refers to a different model. On the left the differences between the models I and II and on the right the ones relative to the model II and III.

	Model II (shift in mm)	Model III (shift in mm)
Pillars D1	0	0
Pillar DUMD1	1 (outward)	1 (outward)
Pillar D2-A	0	2 (inward)
Pillar D2-B	2 (outward)	2 (outward)
Pillar DUMD2	2 (outward)	2 (outward)
Pillar D3-A	0	1 (inward)
Pillar D3-B	2 (outward)	2 (outward)
Pillar DUMD3-A	2 (cutting)	2 (cutting)
Pillar DUMD3-B	2 (outward)	2 (outward)

Table 6.11: Shift in position of the pillars in the two CS modified central region models, named model II and III respectively.

.

the three different geometries of the CS central region. We also studied the effect of the dee voltage extensively.

The percentage of lost particles on each element, depending on the dee voltage and three models, are reported in Table 6.13, together with the results already shown in Table 6.10. The nomenclature used in the table

	Dee-voltage 86 kV	Dee-voltage 90 kV	Dee-voltage 95 kV	Dee-voltage 100 kV
Model I	29.7 %	39.2 %	43.5 %	41.1 %
Model II	25.0 %	38.1 %	47.3 %	52.5 %
Model III	35.6 %	43.2 %	50.5 %	53.0 %

Table 6.12: Injection efficiency ϵ_{inj} in percentage as function of the different models of the CS central region and the dee voltage.

is the same of the one reported in Fig. 6.13.

As reported in Table 6.12, when the nominal voltage is applied on the dees, it is possible to reach transmissions higher than 35% only changing the position of the pillars in the central region. In addition, the use of high dee voltage allows to further increase the injection efficiency.

The maximum increments are obtained for the CS central region geometry corresponding to model III and for the dee voltages equal to 95 and 100 kV. The increase in the injection efficiency between the present situation and the 100 kV dee voltage and model III case is really relevant being more than 65%. Supposing to inject into the CS a DC beam and considering a buncher able to guarantee a buncher efficiency of 50% within 30° RF phase width, the injection efficiency becomes close to 25%. This implies that the total efficiency from the injection up to the energy selection process increases with a factor 1.7 with respect to the value reported in Section 6.6.

6.8   Concluding remarks

The requirements of the NUMEN research project are very challenging since it needs high intensity beams with, at the same time, high energy resolution. The requirements about the beam energy spread limit the maximum beam power that the CS could deliver to NUMEN.

The calculated total efficiency from the CS axial injection up to the extraction is far from the NUMEN requests if we take into account the requirement on the energy spread. Indeed, the beam energy spread at the extraction is higher than the NUMEN requirement. In order to reduce the beam energy spread, it is planned a process of energy selection outside the CS but this implies a reduction of the beam power extracted from the LNS cyclotron.

In this chapter we demonstrated that the energy spread at the extraction

depends on the horizontal emittance of the beam at the extraction and on the energy gain per turn. If a large horizontal emittance circulates in the cyclotron, its contribution to the beam energy spread at the extraction is more important than the energy gain per turn.

This is exactly our case. Indeed, the beam energy spread at the extraction is limited by the large emittance injected in the central region of the LNS cyclotron. The energy spread due to a pencil beam with $10°$ RF phase width injected immediately outside the central region and accelerated up to extraction is twice the NUMEN requirement of the beam energy spread and this value can be considered as a inferior limit obtainable. If a 4 r.m.s. normalized emittance equal to 1π mm-mrad with the same RF phase width is accelerated in the same starting condition, the energy spread is almost twice. Moreover, if the beam presents an initial horizontal offset of 2 mm at the same tracking starting position, the energy spread at the extraction doubles again.

We highlight that the beam emittance value assumed in the simulations is optimistic, since in the reality the emittance should be higher of a factor 2-3 than the ion source value, due to the coupling of the transverse phase spaces introduced by the spiral inflector, assuming a good transport of the beam from the ion source up to the cyclotron central region.

In this chapter, we also evaluated the effect on the energy spread at the extraction by the process of RF phase selection, occurring immediately outside the central region. The simulations showed that loss of about 40% of the injected beam into the cyclotron central region due to the RF phase selection process does not lead to a relevant improvement of the energy spread at the extraction. This can be considered as a further demonstration that the large horizontal emittance injected into the CS central region is the main cause of the low energy spread at the extraction.

Another aspect investigated in this chapter concerns the improvement of the injection efficiency.

The total efficiency from the CS axial bore injection up to the extraction system, supposing also a process of energy selection outside the CS (taking into account only the particles within the energy range of 0.1% around the energy where the distribution is maximum) stays around 2.7% (without phase selection process immediately outside the central region). It is substantial below the 15%, that has been assumed in Table 1.1. The energy selection outside the CS within the 0.1% around the energy where the distribution is maximum is the main cause of the decrease of the total efficiency. In order to increase the total efficiency, a possible solution could be the improvement of the injection efficiency, even if the constraint on the minimum beam energy spread at the extraction obtainable continues to be present.

We investigated how it is possible to increase the injection efficiency by increasing the dee voltage applied on the dees and also by slight modifying the existing central region. Simulations showed that the increase of dee voltages up to the values 95 kV and 100 kV, together with the change of the pillars' position according to the model III in Table 6.11, allows to increase the injection efficiency at around 70% with respect to the present case. Indeed, supposing to inject in the CS axial bore a beam with 4 r.m.s. normalized emittance equal to 1π mm-mrad and 30° RF phase width, the transmission increases from 29.7% to about 50%. This means that the injection efficiency increases from the present value 15% to 25% if we suppose to inject in the CS axial bore a DC beam coming out from the ion source and considering also a buncher in the injection line with bunching efficiency of 50%.

Looking at the total efficiency, it is enhanced of a about a factor 1.7 (in absence of RF phase selection immediately outside the central region) increasing from 2.7% to 4.6%. Otherwise, if the RF phase selection pro-

cess is considered, the total efficiency increases from 1.1% to 1.85%. However, to assume a initial beam energy spread of $\pm 0.6\%$ at the CS axial bore entrance as done is too pessimistic. In the event that a monoenergetic beam is injected in the CS axial bore, ϵ_{inj} increases from the value 29.7% to 46.3%.

Recent tests performed on the RF cavities of the CS have shown that the maximum allowed value of the dee voltage is 82 kV. Above this value, power and instability issues of the RF cavities of the LNS cyclotron occur.

Although the simulations on the injection efficiency have been carried out for dee voltage higher than the operating limit of the RF cavities, they have their physical importance and value for the following reason. The CS is a multi-particle variable energy cyclotron working in constant orbit mode. As already mentioned in Section 6.1, the ^{16}O fully stripped ion with final kinetic energy equal to 100 MeV/amu requires the maximum dee voltage for its acceleration, being that stay on the focusing line of the CS operating diagram. The acceleration of the other ions occurs scaling the dee voltage with the operating frequency, charge to mass ratio, and magnetic field, such that the Reiser parameter remains constant. Consequently, it will be possible to increase the injection efficiency up to a value close to 50%, as reported in Table 6.12, for all the ion species with low and medium energies requiring a dee voltage less than or equal to 82 kV for the acceleration in the CS.

Electrode	Dee voltage 86 kV			Dee voltage 90 kV			Dee voltage 95 kV			Dee voltage 100 kV		
	Model I	Model II	Model III	Model I	Model II	Model III	Model I	Model II	Model III	Model I	Model II	Model III
	Losses (%)	Losses (%)	Losses (%)	Losses (%)	Losses (%)	Losses (%)	Losses (%)	Losses (%)	Losses (%)	Losses (%)	Losses (%)	Losses (%)
ϵ_{inj} (%)	29.69	25.03	35.78	39.20	38.03	43.23	43.50	47.34	50.48	41.09	52.49	53.04
Collimator	5.6	5.4	5.6	5.6	5.4	5.6	5.6	5.4	5.6	5.6	5.4	5.60
Spiral inflector	7.5	7.4	7.4	7.5	7.5	7.5	7.50	7.50	7.5	7.6	7.5	7.5
Housing	6.9	7.4	7.3	4.2	4.63	4.6	3.2	3.5	3.5	2.2	2.4	2.4
Dee tip N1	0.70	0.7	2.00	1.3	1.4	2.7	1.6	1.9	2.8	1.5	2.2	2.60
Pillars D1	21.6	21.6	21.5	17.9	18	17.7	14	14	13.9	11	11.3	113
Pillar DUMD1	/	/	1.6	0.1	0.1	1.4	0.1	0.2	1.3	1.2	0.2	0.8
Dee tip N2	1	0.9	2.5	1.6	1.6	3.3	2.3	2.5	3.8	2.4	3.2	4.2
Pillars D2	22.5	26.4	7.5	16.7	18.7	6.3	11.2	12.7	4.1	8.8	9.1	3.5
Pillar DUMD2	/	/	/	/	/	/	0.1	/	/	4.6	/	/
Dee tip N3	0.8	1.1	2.3	1.4	1.5	3.3	1.8	2.3	3.5	1.9	2.8	3.9
Pillars D3	2.3	1	1	2.6	0.6	0.7	5.9	0.4	0.5	6.1	1.4	1.9
Pillars DUMD3	1.3	3.2	5.3	1.7	2.3	3.6	3	2	2.8	5.6	1.7	3.2
Dummy dee tips	0.1	/	/	0.3	0.3	0.1	0.3	0.3	0.1	0.4	0.3	0.2

Table 6.13: Injection efficiency ϵ_{inj} in percentage as function of the dee voltage and the different models of the CS central region. The features of the model II and III are reported in Table 6.11. The initial number of particles is 10000 for all cases. The percentage of lost particles on each element of the central region are also listed. The nomenclature used in the table is the same of the one reported in fig. 6.13

169

Conclusions and perspectives

The work presented in this thesis has been carried out in the framework of the upgrade of the INFN-LNS Superconducting Cyclotron, known as the CS. The project is devoted to increase the beam power for a set of light-medium ion beams with mass number A $\leq$ 40 and energy from 15 MeV/amu up to 70 MeV/amu by stripping extraction.

These ion beams are mainly requested by NUMEN, an innovative project recently born at INFN-LNS, for nuclear physics studies correlated to neutrino physics. The increment of the beam power for the above-mentioned ions will also allow to increase the beam power of the radioactive ion beams produced at INFN-LNS by means of the in-flight technique. Therefore, new perspectives of research in nuclear physics and astrophysics will open up at LNS laboratories.

This thesis has been mainly focused on two main subjects.

The first deals with the extraction by stripping from the CS.

The ion species that have been considered in the study of stripping extraction are ^{12}C, ^{18}O, ^{20}Ne partial stripped ions, i.e. ions with charge states equal to $Q = Z - 1$, $Z - 2$, $Z - 3$, accelerated up to the desired kinetic energy in the range 15-70 MeV/amu. We assumed an efficiency of the stripping extraction process equal to 100%, according to the expected values of the equilibrium charge fraction F(Q) reported in Table 3.1. Moreover, in the simulations, we assumed a beam energy spread equal to $\pm0.3\%$ FWHM for all the considered case studies.

The study of stripping extraction has been constrained by requirements

related to the full cyclotron design: i) the orbits have to pass at least 70 mm away from the CS centre to avoid any interference with the central region components, ii) the axial beam envelopes have to be lower than ± 15 mm inside the pole and ± 25 mm along the new extraction channel. This study has allowed to determine: i) the stripper foil position for each ion to be extracted by stripping, ii) the maximum transverse dimension and direction of the new extraction channel in the CS to be used for all the ions to be extracted by stripping and iii) the features of the magnetic channels to be installed inside the new extraction channel.

In order to facilitate the connection between the new extraction channel and the new dedicated extraction beam line, a common exit direction and a exit point from the CS to be crossed by all the extracted orbits, have been set.

For each considered ion, the best azimuthal position of the stripper foil has been found in order that the extraction orbit pass as close as possible to the common exit point. We were able to size down the region where to place the stripper foils in two main areas for all ions of interest, one is on the hill, $106° < \theta_{stripper} < 122°$, just where the electrostatic deflector ED1 is placed and the other one is on the valley, $60° < \theta_{stripper} < 88°$, just before the ED1. One of the most relevant results of this study was that only two passive magnetic channels, named MC1S and MC2S, placed in the new extraction channel, are sufficient to permit the extraction of the beams of all ions of interest with different charge states and energies. The gradient for both magnetic channels is 1.8 kG/cm. This result reduces considerably the complexity of the stripping extraction system since it will not necessary to open the CS when the ion to be extracted by stripping changes.

The passive magnetic channels will also be used as steering magnets for adjusting the direction of the extracted orbits inside the new extraction channel in order that each ion passes close as possible to the set exit point

from the CS. According to the simulation results, the steering action of each magnetic channel must be different for each ion. This means that the reference trajectory has to enter the magnetic channels in a different point. In order to do this, a handling system for each magnetic channel will be necessary to adjust their positions according to the ion to be extracted by stripping.

The second subject of this thesis is the beam injection and acceleration up to extraction in the LNS cyclotron. This study has been possible thanks to the development of the beam tracking model of the INFN-LNS Superconducting Cyclotron. AOC, the precise ion tracking code developed by the IBA company, has been used for this purpose.

The computation of particle orbits in the LNS cyclotron has required the development of the models of the magnetic and accelerating structures of the cyclotron to be used for accurate fields calculations.

Part of this thesis work has been dedicated to the creation of the 3D model of the LNS cyclotron acceleration structure by means of the Opera-3d software. It has been created using the modelling approach developed at IBA, consisting in the fully parametrization of the model and its generation by means of macro.

The evaluation of the total efficiency and energy spread at the extraction played an important role within this thesis work. The simulation results have shown that the total transmission efficiency from the CS bore injection up to the extraction system, simulating also a process of energy selection outside the CS, is substantial below the NUMEN requirement, staying only around the 2.7%. In the whole process, the energy selection has an important role in determining the low total efficiency since the beam energy spread at the extraction exceeds the NUMEN requirement and consequently it will be needed a beam removal outside the CS in order to reduce the energy spread.

When a beam is extracted by stripping, the beam energy spread presents two contributions; one is related to the horizontal beam emittance at the extraction and the other one is due to the energy gain per turn.

We demonstrated that the major contribution to the beam energy spread at the extraction in the LNS cyclotron is due to the large emittance circulating in the LNS cyclotron. The energy gain per turn contributes only partially to the energy spread at the extraction but, in any case, it sets an inferior limit on the minimum energy spread obtainable supposing a pencil beam circulating in the CS cyclotron. This value stays around 0.21%, about the twice of the NUMEN requirement.

This thesis allows also to establish a roadmap of the goals and milestones to be achieved in next months/years. According to the results of the simulations, in order to reduce as much as possible the energy spread at the extraction, it will be important in the future to pay attention on the ion beam production and transport of the beam from the ion source up to the CS, which determine the emittance in the horizontal and vertical phase spaces of the beam entering the CS central region. Also a good quality of the accelerated beam will be necessary since, as demonstrated in Chapter 6, an initial beam offset in the central region implies a further increase of the beam energy spread at the extraction.

Milestones to be achieved are: i) to produce ion beams with emittance as small as possible, ii) to have a good transport of the beam (in terms of beam losses, beam quality and beam alignment) along the injection line that links the ion source and the CS and iii) if it is possible, to minimize the coupling between the transverse phase spaces due to the spiral inflector, for example trying to design a new one.

About the increment of the total injection efficiency, we investigated the possibility to increase the injection efficiency applying higher dee voltages than the nominal one and doing slight modifications to the existing central region design, in particular the position of the pillars in the inner

part of the cyclotron have been slight changed. According to the results of the simulations reported in Table 6.12, we increased the injection efficiency up to a factor of about 1.7.

Further investigations will be needed in order to evaluate with more precision the injection efficiency, the total efficiency and the energy spread at the extraction, also in view of a better understanding of the beam features that can be obtained at the ion source extraction.

The transmission in the central region maybe could be also increased trying to improve the transit time factor in the first accelerating gap. Possible studies that could be performed are: i) reduction of the vertical gap in the first dee tip and of the radius of the housing exit hole, ii) redesign of the spiral inflector using a non zero tilt and iii) the changing of the position and orientation of the first dee tip with respect to the spiral inflector. We highlight that the magnetic field in the CS centre is so high that there is just a little room for the electrodes of the central region and spiral inflector and maybe substantial improvement using the first dee tip modification is not really possible.

Acknowlegements

Retracing the path covered during the last three years, I wish to acknowledge my debt to those who have helped me along the way towards this thesis work.

First I desire to thank the prof. Giacomo Cuttone, director of the INFN-Laboratori Nazionali del Sud during the last three years, for the opportunity of carrying out there the PhD course. The INFN also supported my participation to several international conferences, schools and to the internship at the IBA, which had an important role in my professional and human growth. I would like to express my gratitude to Prof. Francesco Cappuzzello for his scientific support during the PhD course. The support of the PhD course coordinator, Prof. Vincenzo Bellini, is especially acknowledged. Another person who deserves my sincere gratitude is Dr. Luciano Calabretta for giving me the opportunity to work in the accelerator and beam R&D group of the INFN-LNS and for his invaluable guidance and support in the course of this work. I would like to thank Dr. Danilo Rifuggiato and Dr. Mario Maggiore for their support and valuable suggestions.

I would like to give special thanks to Dr. Wiel Kleeven, whose patience and fruitful discussions helped me to grow up either form the scientific and human point of view. The nice promenades with him were much appreciated together with his humanity and helpfulness that made me feel like a part of the team. I would like to thank Dr. Eric Forton for giving me the opportunity to spend six months in Louvain La Neuve

Bibliography

[1] O. E. Lawrence et al., Science **72**, 376 (1930).

[2] F. Cappuzzello et al., Eur. Phys. J. A **54: 72**, (2018).

[3] P. Russotto et al., J. Phys.: Conf. Ser. **1014**, 012016 (2018).

[4] Q. R. Ahmad et al., Phys. Rev. Lett. **89**, 011301 (2002).

[5] Y. Ashie et al., Phys. Rev. D **71**, 112005 (2005).

[6] S. Abe et al., Phys. Rev. Lett. **100**, 221803 (2008).

[7] M. H. Ahn et al., Phys. Rev. D **74**, 072003 (2006).

[8] P. Adamson et al., Phys. Rev. Lett. **101**, 131802 (2008).

[9] S. M. Bilenky, Physics Letters B **94(4)**, 495 (1980).

[10] A. S. Barabash, Physics of Atomic Nuclei **74(4)**, 603 (2011).

[11] A. S. Barabash, Phys.Rev. C **81**, 035501 (2010).

[12] S. Pirro, Eur. Phys. J. A **27(S1)**, 25 (2006).

[13] F. T. Avignone III et al., Rev. Mod. Phys. **80**, 481 (2008).

[14] Z. Maki et al., Prog. Theor. Phys. **28(5)**, 870 (1962).

[15] B. M. Pontecorvo, J. Exp. Theor. Phys. Lett. **33**, 549 (1957).

[16] J. Kotila et al., Phys. Rev. C **85**, 034316 (2012).

[17] F. Cappuzzello et al., Eur. Phys. J. A **51: 145**, (2015).

[18] E. Caurier et al., Phys. Rev. Lett. **100**, 052503 (2008).

[19] J. Suhonen et al., Int. J. Mod. Phys. E **17**, 1 (2008).

[20] N. L. Vaquero et al., Phys. Rev. Lett. **111**, 142501 (2013).

[21] J. Barea et al., Phys. Rev. C **87**, 014315 (2013).

[22] A. A. Kwiatkowski et al., Phys. Rev. C **89**, 045502 (2014).

[23] J. Barea et al., Phys. Rev. Lett. **109(4)**, 042501 (2012).

[24] C. Agodi et al., https://web.infn.it/NUMEN/index.php/it/ .

[25] J. Blomgren et al., Phys. Lett. **B 362**, 34 (1995).

[26] F. Naulin et al., Phys. Rev. **C 25**, 1074 (1982).

[27] D.M. Drake et al., Phys. Rev. Lett. **45**, 1765 (1980).

[28] F. Cappuzzello et al., Eur. Phys. J. A **52:167**, (2016).

[29] M. Cavallaro et al., PoS BORMIO2017 **015**, (2017).

[30] P. Van Duppen, Lect. Notes Phys. **700**, 37 (2006).

[31] Y. Blumenfeld et al., Phys. Scr. **T152**, 014023 (2013).

[32] http://www.fair-center.eu/ .

[33] http://frib.msu.edu/about/index.html .

[34] G. Prete, Scholarpedia **5(5)**, 9751 (2010).

[35] G. Raciti et al., Nucl. Instr. and Meth. in Phys. Res. B **266**, 4632 (2008).

[36] A. Pagano, Nucl. Phys. News **22**, 28 (2012).

[37] E. V. Pagano, Eur. Phys. J. Web of Conf. **117**, 10008 (2016).

[38] F. Cappuzzello et al., Eur. Phys. J. A **52**, 167 (2016).

[39] K. Shima et al., Atom. Data and Nucl. Data Tables **51**, 173 (1992).

[40] E. Acerbi et al., Proceedings of the 9th International Conference on Cyclotrons and their Applications, Caen, France, 169 (1981).

[41] F. Alessandria et al., Proceedings of the 13th International Conference on Cyclotrons and their Applications, Vancouver, BC, Canada, 90 (1992).

[42] L. Calabretta et al., Proceedings of the 4th European Particle Accelerator Conference, London, England, 551 (1994).

[43] D. Rifuggiato et al., Proceedings of the 15th International Conference on Cyclotrons and their Applications, Caen, France, 599 (1998).

[44] L. Calabretta et al., Proceedings of the 14th International Conference on Cyclotrons and their Applications, Cape Town, South Africa, 12 (1995).

[45] G. Cuttone et al., Nuclear Instruments and Methods in Physics Research B **261**, 1040 (2007).

[46] G. Bellomo et al., INFN report, INFN/TC-84/5 (1984).

[47] L. H. Thomas, Phys. Rev. **54(8)**, 580 (1938).

[48] C. De Martinis et al., INFN report, INFN/TC-84/25 (1986).

[49] G. Bellomo et al., IEEE Transactions on Nuclear Science, **26**, 2095 (1979).

[50] E. Acerbi et al., Proceedings of the 9th International Conference on Cyclotrons and their Applications, Caen, France, 399 (1981).

[51] E. Fabrici et al., INFN report, INFN/TC-87/4 (1987).

[52] E. Fabrici et al., Nuclear Instruments and Methods in Physics Research **184**, 301 (1981).

[53] S. Gammino et al., Review of scientific instruments, **71**, 631 (2000).

[54] S. Gammino et al., Review of scientific instruments, **70**, 3577 (1999).

[55] A. Kitagawa et al., Proceedings of ECRIS 2012, Sidney, Australia, TUXO03 (2012).

[56] S. Gammino et al., Proc. of the 14th Workshop on ECR ion sources, Geneve, Switzerland 139 (1999).

[57] L. Calabretta et al., Proceedings of the 16th International Conference on Cyclotrons and their Applications, East Lansing, Michigan, USA, 79 (2001).

[58] D. Rifuggiato et al., INFN report, INFN/TC-00/01 (2000).

[59] L. Calabretta et al., Proceedings of the 16th International Conference on Cyclotrons and their Applications, East Lansing, Michigan, USA, 297 (2001).

[60] D. Rifuggiato et al., Proceedings of the 18th International Conference on Cyclotrons and their Applications, Giardini Naxos, Italy, 105 (2007).

[61] G. Bellomo, Proceedings of the 12th International Conference on Cyclotrons and their Applications, Berlin, Germany, 325 (1989).

[62] W. Kleeven, CAS-CERN Accelerator School and KVI: Specialised CAS Course on Small Accelerators, Zeegse, The Netherlands, 271 (2005).

[63] S. L. Snyder, PhD thesis, MSU, (1995).

[64] J. L. Belmont et al., IEEE Transactions on Nuclear Sciences **NS-13**, 191 (1966).

[65] D. Rifuggiato et al., Proceedings of the 20th International Conference on Cyclotrons and their Applications, Vancouver, BC, Canada, 52 (2013).

[66] G. P. A. Cirrone et al., IEEE Transaction on Nuclear Science **51(3)**, 860 (2004).

[67] S. Passarello et al., Proceedings of 2005 Particle Accelerator Conference, Knoxville, Tennessee, 1245 (2005).

[68] G. G. Gulbekyan et al., Proceedings of 18th International Conference on Cyclotrons and their Applications, Giardini Naxos, Italy, 308 (2007).

[69] G. D'Agostino, Simulazioni di dinamica dei fasci per l'upgrading del Ciclotrone Superconduttore dei LNS, Master thesis on physics, University of Catania, 2015 .

[70] A. Calanna et al., Proceedings of the 13th International Conference on Heavy Ion Accelerator Technology, Yokohama, Japan, 23 (2015).

[71] A. Radovinsky et al., IEEE Transactions on applied superconductivity **26 No. 4**, (2016).

[72] G. Gallo et al., Proceedings of 18th International Conference on Cyclotrons and their Applications, Zürich, Switzerland, 322 (2016).

[73] A. D. Russo et al., J. Phys.: Conf. Ser. **1056**, 012051 (2018).

[74] S. Russo, LNS internal report (2017).

[75] L. Celona et al., 21st International Particle Accelerator Conference, Copenhagen, Denmark, 570 (2017).

[76] S. S. Tomic et al., IPhys. Rev. E **65**, (2002).

[77] H. Houtman et al., Busse W., Zelazny R. (eds) Computing in Accelerator Design and Operation. Lecture Notes in Physics, Springer, Berlin, Heidelberg, **215**, 98 (1984).

[78] http://operafea.com .

[79] W. Kleeven et al., CERN Yellow Report CERN-2017-004-SP, presented at the CAS-CERN Accelerator School on Accelerators for Medical Application, Vösendorf, Austria, 177 (2015).

[80] W. Kleeven et al., Proceedings of the 7th International Particle Accelerator Conference, Bexco, Busan Korea, 1902 (2016).

[81] G. Bellomo et al., Nuclear Instruments and Methods, **206**, 19 (1983).

[82] K. Brown et al., CERN-80-04, NAL-91, FERMILAB-NAL-091, UC-28 (1980).

[83] R. Baartman, TRIUMF Beam Physics Note, TRI-BN-15-07 (2015).

[84] M. A. Leitner, Proceedings of the 2001 Particle Accelerator Conference, Chicago, Chicago, Illinois USA, 67 (2001).

[85] W. Kleeven et al., Internal report, IBA (2009).

[86] A. Caruso et al., Proceedings of the 20h International Conference on Cyclotrons and their Applications, Vancouver, Canada, 147 (2013).

[87] H. Matsubara et al., Few Boby Systems **54 1433**, (2013).

[88] W. Kleeven et al., Nuclear Instruments and Methods in Physics Research **B64**, 367 (1992).

182